

Magnetosensitive e-skins for interactive electronics

DISSERTATION

zur Erlangung des akademischen Grades

Doktoringenieur (Dr.-Ing.)

vorgelegt

der Fakultät Maschinenwesen

der Technischen Universität Dresden

von

Msc. Gilbert Santiago Cañón Bermúdez

geboren am 26. August 1989 in Bogotá, Kolumbien

Tag der Einreichung: 28. Juni 2019

Gutachter: Prof. Dr. Gianaurelio Cuniberti

Prof. Dr. Jürgen Fassbender

Prof. Dr. Kornelius Nielsch

"The scientists of today think deeply instead of clearly. One must be sane to think clearly, but one can think deeply and be quite insane"

Nikola Tesla

Abstract

The rapid progress of electronics and computer science in the last years has brought humans and machines closer than ever before. Current trends like the Internet of Things and artificial intelligence are closing the gap even further, by providing ubiquitous data processing and sensing. As this ongoing revolution advances, novel forms of human-machine interactions are required in an ever more connected world. A crucial component to enable these interactions is the field of flexible electronics, which aims to establish a seamless link between living and artificial entities using electronic skins (e-skins). E-skins combine the functionality of commercial electronics with the soft, stretchable and biocompatible characteristics of human skin or tissue. Until lately, the focus had been to replicate the standard functions associated with human skin, such as, temperature, pressure and chemical detection. Yet, recent developments have also introduced non-standard sensing capabilities like magnetic field detection to create the field of magnetosensitive e-skins. The addition of a supplementary information channel—an electronic sixth sense—has sparked a wide range of applications in the fields of cognitive psychology and human-machine interactions.

In this thesis, we expand the concept of magnetosensitive e-skins to include the notion of directionality, which utilizes the full interaction potential of the magnetic field vector. Also, we introduce the use of flexible magnetoelectronics in virtual/augmented reality and human-computer interfaces. Three main results are attained in the course of this work: (i) we first demonstrate how magnetosensitive e-skins can be used as human-machine interfaces driven by permanent magnet sources in the range of 5 mT. (ii) Building upon this milestone, we realize the first magnetosensitive e-skins which are driven by the earth’s magnetic field of 50 μ T. (iii) We fabricate magnetosensitive e-skins which push the detection limit below 1 μ T. The magnetosensitive e-skins in this work open exciting possibilities for sensory substitution experiments and sensory processing disorder therapies. Furthermore, for human-machine interactions, they provide a new interactive platform for touchless and gestural control in virtual and augmented reality scenarios beyond the limitations of optics-based systems.

Zusammenfassung

Der rasante Fortschritt der Elektronik und der Informatik in den letzten Jahren hat Mensch und Maschine nähergebracht als je zuvor. Aktuelle Trends wie das Internet der Dinge und künstliche Intelligenz schließen die Lücke noch weiter, indem sie eine allgegenwärtige Datenverarbeitung und -erfassung ermöglichen. Mit fortschreitender Revolution sind neue Formen der Mensch-Maschine-Interaktion in einer immer vernetzter werdenden Welt erforderlich. Eine entscheidende Komponente, um diese Interaktionen zu ermöglichen, ist das Gebiet der flexiblen Elektronik, das darauf abzielt, mithilfe elektronischer Häute (e-skins) eine nahtlose Verbindung zwischen lebenden und künstlichen Entitäten herzustellen. E-skins verbinden die Funktionalität kommerzieller Elektronik mit den weichen, dehnbaren und biokompatiblen Eigenschaften menschlicher Haut oder menschlichen Gewebes. Bis vor kurzem lag der Schwerpunkt auf der Nachbildung der mit der menschlichen Haut verbundenen Standardfunktionen wie Temperatur-, Druck- und Chemikalienerkennung. Jüngste Entwicklungen haben jedoch auch nicht standardmäßige Erfassungsfähigkeiten wie die Magnetfeldererkennung eingeführt, um das Feld magnetoempfindlicher e-skins zu erzeugen. Die Hinzufügung eines zusätzlichen Informationskanals - eines elektronischen sechsten Sinns - hat eine breite Palette von Anwendungen auf den Gebieten der kognitiven Psychologie und der Mensch-Maschine-Interaktionen ausgelöst.

In dieser Arbeit erweitern wir das Konzept der magnetoempfindlichen e-skins um den Begriff der Richtwirkung, bei dem das volle Wechselwirkungspotential des Magnetfeldvektors genutzt wird. Außerdem führen wir die Verwendung flexibler Magneto Elektronik in der virtuellen Realität / erweiterten Realität und in Mensch-Computer-Schnittstellen ein. Im Verlauf dieser Arbeit werden drei Hauptergebnisse erzielt: (i) Wir demonstrieren erstmals, wie magnetoempfindliche e-skins als Mensch-Maschine-Schnittstellen verwendet werden können, die von Permanentmagnetquellen im Bereich von 5 mT angetrieben werden. (ii) Aufbauend auf diesem Meilenstein realisieren wir die ersten magnetoempfindlichen e-skins, die vom Erdmagnetfeld von 50 μT angetrieben werden. (iii) Wir fertigen magnetoempfindliche e-skins, bei denen die Nachweisgrenze unter 1 μT liegt. Die magnetoempfindlichen e-skins in dieser Arbeit eröffnen aufregende Möglichkeiten für sensorische Substitutionsexperimente und Therapien bei sensorischen Verarbeitungsstörungen. Darüber hinaus bieten sie für die Mensch-Maschine-Interaktion eine neue interaktive Plattform für die berührungslose und gestische Steuerung in virtuellen und Augmented Reality-Szenarien, die über die Grenzen optikbasierter Systeme hinausgehen.

Confirmation

I confirm that I independently prepared the thesis and that I used only the references and auxiliary means indicated.

Acknowledgments

As I summarize these last years of research, it is inevitable to appreciate the contributions of so many who have helped me walk this road. First, I would like to thank Prof. Dr. Jürgen Fassbender and Prof. Dr. Gianaurelio Cuniberti who granted me a fantastic place to do my research and continuously supported all projects I took part in. Also, I wish to express my gratitude to Dr. Denys Makarov for showing me the importance of effectively communicating scientific results to the public. His drive to find new collaboration partners and promote the work of our group, never ceases to amaze me. Furthermore, his continuous support with all administrative matters has given me the freedom to seamlessly conduct my research. I would like also to thank Prof. Dr. Martin Kaltenbrunner for his helpful advice during the conception of the papers which constitute this work and his continuous support in many international conferences. Along the same lines, I'm deeply grateful to Dr. Jürgen Lindner who was very understanding and helpful every time we met.

At my former institute, the IFW Dresden, I'd like to thank Prof. Dr. Oliver G. Schmidt for the support during the first stages of this work. Also I'd like to acknowledge all the insightful dialogues, feedback and lessons learnt from Dr. Daniil Karnaushenko, Dr. Dmitriy Karanushenko, Dr. Michael Melzer and all the other members of the former MAGNA group.

I am very grateful to Dr. Tobias Kosub and Dr. Martin Kopte, who always kept me sane in moments of difficulty, through meaningful conversations and hilarious impersonations. Besides this, they also broadened my knowledge by giving me insights into the working principles of many setups and magnetic effects. Thanks also to Dr. Jin Ge for teaching me a lot about chemical processes in the last two years and for all the fruitful conversations we shared. Thanks a bunch to Tetiana Voitsekhivska who helped me immensely to complete circuits and lithography processes, and promptly supported me whenever a deadline was approaching. Huge thanks to Hagen Fuchs for all the programming magic, wonderful conversations and book recommendations. Thanks a lot to Xu Wang, Dr. Oleksii Volkov, Dr. Rico Illing and the rest of the group for all the help in the lab, lunch break exchanges and memorable bus rides. Many thanks also to Pablo Granell and Gouliang Wang for all their experimental input to assemble and debug many measurement setups, which were essential for the last part of this thesis. I would like also to acknowledge the constant support of Dr. Lothar Bischoff, Bernd Scheumann, Tommy Schönherr, Claudia Neisser and all the other members of the characterization and fabrication facilities at HZDR.

Many thanks to Dr. Kai Wagner, Dr. Ana Semisalova, Alexandra "Sasha" Titova, Xiaomo Xu and all the members of magnetobiernonics for welcoming me in HZDR. It has been quite a ride. Special thanks also to Dr. Leonardo "Carlito" Medrano, Dr. Anniruddha Mitra, Dr. Alejandro "Tiger" Santana, Andrés Ramos, Dr. Marisinha

and all the members of What is love, you guys made this road much more fun. My deepest appreciation to Dr. Eduardo "Lalo" Rojo and Marta Urbanska; with whom I respectively lost a legendary backpack and shared many evenings on a tennis court. Sincere thanks to Camilo "Chapita" Téllez, Cindy Montenegro and Daniel Moreno for their jokes, unconditional warmth and philosophical discussions, as part of the Colombian legion in Germany.

Not least of all, I want to thank my beloved family and girlfriend who have been an unconditional source of love, patience and understanding throughout the course of this work. My parents have made me everything I am today; allowing me to grow as an independent person but also teaching me valuable lessons about kindness, resilience and honesty. My sister has been the light of my life, my companion and friend through all the good and bad moments I have been through. Every time I see her I remember that it is worth fighting for what we love. Georgi, words are not enough to describe how much you have helped me to reach new heights in every aspect of my life. You have been with me through thick and thin, shown me how to be more loving, and led me to many insights which have made me a better person.

Contents

1	Introduction	13
1.1	Motivation and scope	13
1.2	Accomplishments	15
1.3	Thesis structure	16
2	Background	17
2.1	Flexible electronics	17
2.1.1	A brief history	17
2.1.2	Electronic skins (e-skins)	19
2.1.3	Enhanced mechanical properties	21
2.2	Thin film magnetic field sensors	22
2.2.1	Magnetoresistive sensors	22
2.2.2	AMR sensors	22
2.2.3	Giant magnetoresistive (GMR) sensors	26
2.2.4	Spin-valves	28
2.3	Interactive devices and human-computer interfaces (HCI)	31
2.3.1	Early stages	31
2.3.2	Beyond standard interactions	32
2.3.3	Interactive devices based on magnetic fields	33
3	Fabrication and characterization techniques	37
3.1	Device design	37
3.2	Photolithography	37
3.2.1	General process	38
3.2.2	Considerations for ultra-thin substrates	40
3.3	Thin film deposition	43
3.3.1	Magnetron sputter deposition	43
3.3.2	E-beam evaporation	44
3.4	Characterization of device properties	44
3.4.1	Magnetoresistive characterization	44
3.4.2	Mechanical characterization	46
3.4.3	Morphological characterization	47
4	Magneto-sensitive e-skins with directional perception	49
4.1	Introduction	49
4.2	Fabrication process	50
4.3	Mechanical characterization and performance	53
4.4	Magnetoresistive performance	57
4.5	Application examples	59

4.5.1	Virtual keypad	59
4.5.2	Interactive light dimming by touchless manipulation	60
4.6	Reliability tests	61
4.6.1	Encapsulation performance	61
4.6.2	Angular resolution	61
4.6.3	Temperature stability	63
5	Geomagnetosensitive e-skins	67
5.1	Introduction	67
5.2	Barber-pole-based geomagnetosensitive e-skins	68
5.2.1	Fabrication and mechanical performance	68
5.3	Conditioning and magnetoresistive characterization	72
5.4	Geomagnetic field measurements	76
5.5	Application examples	78
5.5.1	E-skin geomagnetic orientation in the outdoors	78
5.5.2	Geomagnetic virtual reality control	80
6	Sub-μT magnetosensitive e-skins	82
6.1	Introduction	82
6.2	Fabrication process	82
6.3	Magnetoresistive characterization	83
6.4	Compliant PHE sensors for detecting magnetic stray fields	84
7	Summary and outlook	86
7.1	Summary	86
7.2	Outlook	88

List of Figures

2.1	The early years of flexible electronics.	18
2.2	E-skins: from science fiction to reality.	20
2.3	Scattering cross-section change in an AMR film.	23
2.4	Relationship between the magnetization and current vectors in an AMR film.	23
2.5	Barber pole modification and Wheatstone bridge arrangement.	24
2.6	Planar Hall effect measurement scheme and magnetoresistive response.	26
2.7	GMR effect and exchange coupling in multilayered systems.	27
2.8	RKKY coupling and Mott model.	28
2.9	Spin-valve working principles.	29
2.10	Spin-valve-based Wheatstone bridge.	31
2.11	The early years of interactive devices and VR.	32
2.12	The new era of VR devices and haptics.	34
2.13	Interactive devices based on magnetic fields.	36
3.1	From conceptual design to device fabrication.	38
3.2	Photolithographic process.	39
3.3	Laser writing process.	39
3.4	Processing of ultrathin polymer films by adhesion layers.	41
3.5	Sacrificial layer processing of ultrathin polymer films.	41
3.6	Expansion correction of photolithographic masks.	42
3.7	Thin film deposition methods.	44
3.8	Setups for magnetoresistive characterization.	45
3.9	Mechanical characterization tools.	47
4.1	Touchless manipulation of objects based on the interaction with magnetic fields.	50
4.2	Fabrication of spin-valve sensor chips.	51
4.3	Assembly of a 2D magnetosensitive e-skin.	52
4.4	Compliance characterization of the 2D magnetosensitive e-skin.	54
4.5	Functional tests of a single spin-valve sensor under mechanical strain.	55
4.6	Mechanical stability of the sensor layer stack upon bending.	56
4.7	Magnetoresistive characterization of spin-valves and angle reconstruction.	58
4.8	Virtual keypad addressed in a touchless manner.	60
4.9	Light dimming of a virtual bulb.	61
4.10	Encapsulation experiments for a spin-valve sensor.	62
4.11	Morphology and thermal performance of the polyimide foils.	65
4.12	Temperature compensation of the sensor bridge.	66

5.1	Fabrication of the barber pole geomagnetic e-skin.	69
5.2	Mechanical performance of the barber pole geomagnetic e-skin.	70
5.3	Morphological characterization of the barber pole geomagnetic e-skin upon bending.	71
5.4	Tuning effects of the geometric conditioning and aspect ratio of the sensors.	73
5.5	Magnetoresistive characterization and flipping effects in the geomagnetic e-skin.	75
5.6	Detection of the earth's magnetic field upon rotational offset.	77
5.7	Thermal noise of the e-skin compass.	78
5.8	On-skin geomagnetic orientation setup.	79
5.9	Outdoor geomagnetic detection.	80
5.10	Geomagnetic interaction with a virtual reality environment.	81
6.1	Fabrication, imaging and measurement of PHE e-skins.	83
6.2	Magnetic stray field detection with PHE sensors.	85

List of abbreviations

AC Alternating current

AI Artificial intelligence

AMR Anisotropic magnetoresistance

AR Augmented reality

CAD Computer-aided design

DC Direct current

DMAc Dimethylacetamide

DTPA Diethylenetriaminepentaacetic acid

EB Exchange bias

FFT Fast Fourier Transform

FIB Focused ion beam

GMR Giant magnetoresistance

HCI Human-computer interactions

HMD Head-mounted display

IoT Internet of Things

PAA Polyacrylic acid

PCB Printed circuit board

PDMS Polydimethylsiloxane

PET Polyethylene terephthalate

PHE Planar Hall effect

PI Polyimide

SEM Scanning electron microscopy

SPD Sensory processing disorder

SQUID Superconducting quantum interference device

TFT Thin film transistor

TMR Tunnel magnetoresistance

VHB Very high bonding

VR Virtual reality

Chapter 1

Introduction

1.1 Motivation and scope

In the last decades, the evolution of electronics and computer science has given birth to ever more intelligent machines and systems, which are rivaling human intelligence. Concepts like the Internet of Things (IoT) ¹ and artificial intelligence (AI) ² are increasingly pervading our world and demand for new kinds of human-computer interactions (HCI). ^{3,4} State-of-the-art robots and computational systems are behaving more “human-like” thanks to the massive amounts of data collected by sensor networks and analyzed by AI platforms. ⁵ At the same time, humans are more connected than ever due to the numerous portable and wearable gadgets continuously monitoring and influencing our day-to-day life. ^{6,7} As these technologies progress further, the boundaries between humans and machines are becoming fuzzier, and new aspects of human perception and device interactivity are being discovered. A key part of this development is the field of flexible electronics, which promises to harmoniously bridge the living and digital worlds by means of electronic skins (e-skins). ^{8–11} These e-skins aim to preserve the functionality of standard electronics while allowing skin or tissue-like properties such as flexibility, stretchability and biocompatibility. ^{8,12–14} Accomplishing this vision could provide humans with more natural prosthetics, skin substitutes or even a second skin with additional functionalities. Mostly, the efforts in this field have focused on the development of temperature, pressure and chemical sensors, ^{6,7,15} which address the natural aspects of human skin. However, recent works ^{16,17} on shapeable magnetoelectronics ¹⁸ have introduced a new sensorial dimension to e-skins, namely, the ability to detect and interact with magnetic fields. These magnetosensitive e-skins have opened up exciting possibilities for human perception as they could become a supplementary information channel beyond the standard five senses. Exploiting this additional information channel could significantly influence both sides of the human-machine spectrum.

On the human side, they could provide a way to systematically study the effects of magnetic fields in sensory perception. This task has been the subject of controversy especially when investigating the influence of the earth’s magnetic field. ¹⁹ Many animal species certainly possess an in-built sensitivity to magnetic fields termed magnetoreception, ^{20–22} however it still remains unclear whether humans also do. ^{23,24} Exploring this phenomenon is of crucial importance for biology as it has been suggested that it might be “the primal sense”, ²³ and thus an evolutionary link to other

species. Also, in the field of cognitive psychology, magnetoreception, whether natural or artificially provided, is of paramount relevance for the understanding of navigation and sensory substitution.^{25–30} Elucidating the underlying mechanisms of these two topics could help to explain how and if new senses can be acquired. Furthermore, this knowledge can be used to treat individuals with sensory processing disorder (SPD),^{31–34} which “exists when sensory signals are either not detected or don’t get organized into appropriate responses”.³³ In this case, magnetosensitive e-skins together with active feedback could increase the spatial awareness of patients and complement the proprioceptive or vestibular therapies commonly used. Apart from these approaches, some people would like to use additional senses to enhance their natural perception beyond the usual five senses. Technology enthusiasts have tried to artificially replicate magnetoreception using wearable devices³⁵ or implants;³⁶ yet, these approaches remain unpopular due to their bulkiness or cumbersome implementation. Here, magnetosensitive e-skins could provide a seamless way of integrating this desired functionality with the human body.

On the side of machines, magnetosensitive e-skins exploit an often overlooked stimulus like magnetic fields, to enable new kinds of flexible and soft human-machine interfaces. Conventional approaches in the field of flexible electronics utilize capacitive or strain sensing,^{37–39} and therefore are limited to touch-based interactions. Magnetic sensing, on the other hand, can be used as an inherently touchless detection platform, which unlocks a wide array of interaction scenarios.¹⁸ Due to the three-dimensional pervasiveness of magnetic fields, they allow for ubiquitous and unobstructed interactivity, which can be used to reconstruct motion or position in space. This aspect can be utilized for example, to fabricate gestural control interfaces which behave as the touchless analog of pressing and turning interactions. Moreover, as magnetosensitive e-skins do not require line-of-sight to operate, they do away with complex setups or cameras which optical systems typically use. In addition, magnetic sensors can operate using compact and “self-powered” sources like permanent magnets, or even go source-less by exploiting the omnipresent geomagnetic field. All these characteristics are desirable to create portable, lightweight and mechanically compliant human-machine interfaces, which provide a new platform for virtual (VR) and augmented reality (AR) systems. This novel platform could become a natural evolution beyond the typically rigid VR gadgets; by enabling fine motion tracking in a compact, soft and flexible manner.

1.2 Accomplishments

This thesis has advanced the field of shapeable magnetoelectronics¹⁸ by adding directional perception as a new sensing mode and showing how this novel approach can be employed in numerous application fields. Previous shapeable magnetoelectronic devices were limited to proximity detection and therefore did not use the full interaction potential of the magnetic field vector. The results of this thesis demonstrate a new kind of interactive devices in the form of magnetosensitive e-skins which can be employed in AR or VR scenarios. Various configurations allow these magnetosensitive e-skins to operate with standard permanent magnet sources,⁴⁰ using geomagnetic⁴¹ or sub-geomagnetic fields.⁴² During this thesis I accomplished the following tasks:

- Set up a group of labs suitable for polymer synthesis, microfabrication and characterization of flexible electronics.
- Developed sample preparation methods which allow handling and patterning on flexible and ultrathin polymeric substrates using standard photolithography conditions.
- Established microfabrication procedures and photolithography strategies to overcome the alignment difficulties arising from the thermal expansion or physical displacement of ultrathin polymer substrates.
- Wrote computer scripts and instrument control programs to automatize measurement setups, collect data and calculate relevant experimental parameters.
- Created an uncomplicated transfer printing methodology to fabricate angular magnetic field sensors on ultrathin substrates employing a single deposition run and without the need for laser annealing.
- Introduced the idea of using magnetosensitive e-skins for multi-directional interactivity, which ultimately merged the field of flexible magnetoelectronics with VR, AR and HCI.
- Devised a fabrication route for geomagnetic field sensors on ultrathin substrates, thus extending the capabilities of shapeable and imperceptible magnetoelectronics to the μT detection range.
- Designed and built characterization setups to measure the magnetoresistive properties of magnetosensitive e-skins under static or dynamic bending conditions.
- Supervised and collaborated on the conception and realization of magnetosensitive e-skins with sub- μT detection capabilities.
- Attended conferences and workshops where I presented and disseminated the results of this work.
- Supervised master students towards the successful completion of their master theses and project works/lab rotations.

1.3 Thesis structure

Chapter 2 presents a survey of the most prominent concepts and prior art required for the understanding of this thesis. The chapter first addresses the history of flexible electronics, the evolution of electronic skins and their resurgence with enhanced mechanical properties. Next, the most relevant types of magnetoresistive sensors for this work are discussed and their working principles explained. Lastly, some of the most important milestones in the history of interactive devices, virtual reality and magnetic interfaces are highlighted.

Chapter 3 introduces the fabrication and characterization methods utilized during this thesis. First, general concepts of photolithography and thin film patterning are explained. Then, sample preparation techniques for flexible substrates and thin film deposition methodologies are examined. Finally, various magnetoresistive and mechanical characterization approaches are described.

Chapter 4 is dedicated to a new class of magnetosensitive e-skins with directional perception, which advance beyond the proximity sensing concept. The chapter explains the working principle of these novel e-skins, which is based on specifically arranged spin-valve sensors. Subsequently, fabrication details, material properties and characterization methods needed to gauge the performance of these e-skins are provided. Application examples in the fields of touchless interactive devices and virtual reality are presented at the end.

Chapter 5 builds upon the ideas of the previous chapter to create geomagnetosensitive e-skins, i.e, magnetosensitive e-skins driven only by the earth's magnetic field. The technology at the core of this achievement; barber pole modified AMR sensors, is correspondingly introduced. The chapter then describes the fabrication process, magnetoresistive characterization and vectorial experiments performed to ensure the proper reconstruction of the geomagnetic field. Two potential uses in the fields of portable on-skin orientation devices and geomagnetic virtual reality are presented in the last part.

Chapter 6 explores how to achieve magnetosensitive e-skins with sub- μT detection, to potentially access the tiny biomagnetic fields of the human body towards point-of-care devices. For this purpose, a different measurement configuration based on the planar Hall effect is proposed. The chapter summarizes the fabrication, magnetoresistive characterization and mechanical tests carried out to validate the functionality of these e-skins. Lastly, two demonstrators for detecting small stray magnetic fields in stationary and rotating conditions are presented.

Chapter 7 summarizes this work and discusses outlook scenarios to enhance the functionality of magnetosensitive e-skins or extend the concept of functional e-skins to include sensory feedback in biological entities. Potential improvements for magnetosensitive e-skins like nerve stimulation, wireless communication and integration with active electronics, multiaxial sensing, and encapsulation are presented.

Chapter 2

Background

2.1 Flexible electronics

Electronics is one of the most important pillars of the modern world and probably the most subversive technology of the last fifty years. Its constant evolution keeps on driving our society forward in ways which were unthinkable when the first transistor was fabricated and described by Shockley and collaborators.⁴³ As this technology continues to reach for new frontiers, the modern trends of our civilization require novel kinds of functional electronics which are flexible,^{6,9,44} stretchable^{12,13,45} and wearable.⁴⁶⁻⁴⁸ This innovative electronics aim to integrate with and mimic biological entities or structures, while preserving its functionality and becoming a seamless link between machines and the living world.¹⁰ Conventional electronics manufacturing is not suitable to address these societal needs, mainly due to the restrictions imposed by its usually rigid substrates and fabrication techniques. Therefore, to bring mechanical flexibility to electronics, researchers shifted their attention towards thin film fabrication methods, which are at the core of what is now called flexible electronics.

2.1.1 A brief history

It would be tempting to consider flexible electronics a new research field; however, its origins can be traced as far back as 1903, when Hanson proposed a flat foil conductor in British patent 4681. Unfortunately, the interest back then was not in flexible devices but rather in cables and interconnects, so this idea found no application in flexible electronics. Nevertheless, the concept of interconnecting components motivated other inventors like Charles Ducas, who in 1925 patented a method to print conductive inks onto non-conducting substrates.⁴⁹ This invention would ultimately pave the way for modern printed circuit boards (PCBs) and additive manufacturing, both of key relevance in flexible electronics. Some decades later, Lilienfeld⁵⁰ and Heil⁵¹ would first conceive the thin film transistor (TFT), but due to the limited technology at the time, they could not fabricate it. This invention remained dormant until RCA labs finally materialized it in 1962⁵² and then were forced to stop when MOS transistors took industry over. This move left Westinghouse labs as the only TFT player and the one who would first demonstrate in 1967^{53,54} a plethora of digital and power circuits on paper and plastic. All these newly devised circuits attracted the attention of the aerospace industry, which aimed to increase

the generated power per unit weight for their solar cell modules.⁵⁵ However, with the decay of space exploration activities and further industrial developments, thin film circuits were temporarily forgotten.

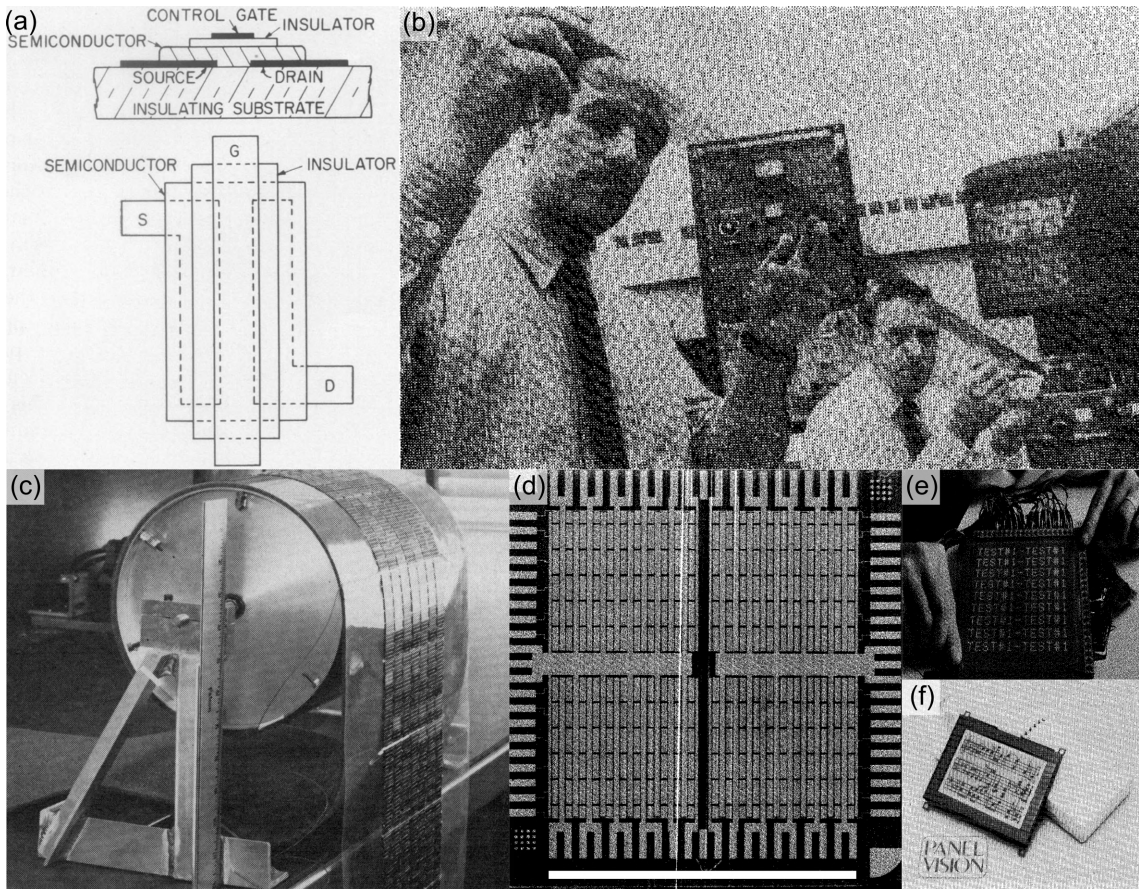


Figure 2.1: **The early years of flexible electronics.** (a) Cross-sectional and top view of the first fabricated TFT at RCA labs.⁵² (b) Large-area production of TFTs on Mylar at Westinghouse labs.⁵⁴ (c) Twelve inch solar cell array produced for the US Air force using thin film technology.⁵⁵ (d) TFT power device by Westinghouse labs (1973). Scale bar indicates one inch. (e) Demonstration screen with 120 x 120 TFT elements (Westinghouse 1974). (f) TFT addressed liquid crystal (LC) panel manufactured by Panelvision in 1983. Images (d) to (f) are taken from.⁵⁴

Yet, during the 70s and 80s, science fiction books and films popularized the early notions of bionic body parts and inadvertently set the ground for future electronic skins. Series like *The Six million Dollar Man*⁵⁶ and movies like *Star Wars*⁵⁷ and *Terminator*⁵⁸ already depicted bionic replacements, electronic hands and self-healing materials. All these fictional stories started to come to reality in 1974 when Clippinger et al. demonstrated an implantable feedback system for prosthetics.⁵⁹ Then, in 1985, General Electric created the first prototype of a sensitive skin for a robotic arm,⁶⁰ integrating 500 infrared sensors on Kapton foil (inter-sensor distance 5 cm). During the 90s, a series of large-area, low-cost flexible sensors and actuators were developed for detecting signals in (until then) unconventional environments^{61–63} or for motion planning.^{64,65} One of the most prominent examples was the work of Lee et al., which combined shear stress sensors and Microelectromechanical systems

(MEMS) actuators on a single skin.⁶⁶ Just at the turn of the century, a seminal paper on the mechanics of film-on-foil electronics⁶⁷ would spark the current era of flexible electronics.

2.1.2 Electronic skins (e-skins)

At the dawn of the new millennium, flexible circuits were a reality and researchers were moving more and more towards plastic-based electronics, as seen in the classical review “putting it on plastic”.⁶⁸ However, it was not clear yet where to employ the mechanical advantages of this emerging technology. The tipping point was the 1999 “Sensitive Skin Workshop” in Arlington where it was first recognized that “sensitive skins” could find their niche in human sensing, textiles and robotics.⁶⁹ In the following years, researchers began integrating different kinds of sensors onto these artificial skins, propelled by the ideas of this workshop. Amidst this exploration, the first use of the expression electronic skins in the context of flexible electronics came in an article by Wagner and coworkers.⁷⁰ In this work, they describe the use of stretchable metallization on elastomeric substrates to interconnect rigid islands hosting functional cells of electronic circuitry and sensors. This rigid-island approach became one of the most used topologies, as it preserves the integrity of the functional elements while the rest of the skin stretches. At the same time, the possibility of having multiple islands with different functionalities opened the door for multisensory electronic skins. From there, a subsequent paper by Someya et al.⁷¹ introduced the term e-skins and combined temperature and pressure mapping for the first time in flexible electronics. Further efforts from Prof. Rogers and coworkers consolidated the field by establishing a wide range of fabrication methods for flexible, high-performance semiconductors and epidermal circuits.^{11,72 –77} Contributions from Prof. Bauer and coworkers have explored the use of soft dielectrics,^{78,79} ferroelectrets⁸⁰ and solar cells.⁸¹ In a breakthrough paper, Kaltenbrunner et al. introduced the concept of imperceptible electronics, where reducing substrate thickness renders the fabricated devices virtually unbreakable.⁸² Based on this concept, the groups of Profs. Someya and Bauer have explored numerous applications in photonics,^{83,84} biosensing^{85,86} and photovoltaics.⁸⁷ In parallel, the groups of Profs. Rogers and Bao have initiated the field of transient and bioresorbable electronics,^{88 –90} in line with modern environmentally-friendly policies. Recently at MIT media lab, Kao and coworkers have created various kinds of electronic tattoos which act as interactive devices and “Hybrid body craft”.^{91 –93} In the last years, our group and formerly at the IFW Dresden, we have developed the concept of shapeable magnetoelectronics,¹⁸ which bridges the world of e-skins with that of thin film magnetic field sensors to add an additional “sixth sense”.¹⁷



Figure 2.2: **E-skins: from science fiction to reality.** (a) Artificial limb portraying early visions of e-skins in the film *Star Wars V: The Empire Strikes Back*.⁵⁷ (b) Image from the film *The terminator* depicting how e-skins could replicate the properties of human skin in robotic entities.⁵⁸ (c) Sensitive skin module with 8 x 8 infrared sensor pairs developed by Lumelsky at the Robotics Laboratory in the University of Wisconsin-Madison.⁶⁹ (d) Electronic artificial skin based on organic transistors developed by Someya et al.⁹⁴ (e) Epidermal electronic tattoo with wireless transmission and sensing modules. The tattoo remains functional under compression (left) and stretching (right).⁷⁶ (f) Imperceptible electronic skin hosting a 12 x 12 active matrix of organic field effect transistors.⁸² (g) Bending-insensitive pressure sensors acting as a second skin on a human hand to detect slight normal forces.⁹⁵ (h) Nanomeshed on-skin electronic circuit with high compliance and breathability.⁹⁶ (i) Colorimetric UV dosimeter based on epidermal electronics developed by Rogers group at Northwestern University.⁹⁷ (j) Gold leaf skin user interfaces for interactive electronics and functional body craft.⁹² (k) Interactive pointing device based on imperceptible magneto-electronics mounted on a finger.¹⁷ (l) E-skin based control of a virtual reality environment using the earth's magnetic field.⁴¹

2.1.3 Enhanced mechanical properties

While the fabrication of flexible circuits was already available since the early 90s, the breakthrough in understanding came with Suo's work in 1999.⁶⁷ Only then it became clear what mechanical advantages would it bring to manufacture circuits on compliant and thin substrates. The main realization by Suo and coworkers was to treat the thin film on foil problem as a classical composite beam problem of continuum mechanics. In doing so, they found out that reducing the substrate thickness is also effectively reducing the strain experienced by the thin films on top. This result comes as a natural consequence of the equation describing the strain along the bending direction x in a structure:⁹⁸

$$\epsilon_x = \frac{z}{R} \quad (2.1)$$

As seen in equation 2.1, the strain in x ϵ_x scales linearly in the z direction or thickness of the substrate and it's inversely proportional to the curvature radius R . Three implications stem from this statement: (i) At $z = 0$, the neutral mechanical plane, there's no strain, (ii) large curvature radii decrease strain and (iii) the larger the z position is, the more strain in that plane. All these facts are usually seen in nature and it is why thick objects have a large bending stiffness.⁹⁹ Another key point of this research was noticing that by having softer substrates, with lower Young's moduli, like plastic, the strain could also be reduced. This follows from the calculation of the centroid for a composite structure. In the case of a single-material structure or one where the Young's moduli are similar, for example metals on silicon, the centroid \bar{z} lies in the middle of the structure:

$$\bar{z} = \frac{(d_f + d_s)}{2} \quad \text{and the strain is:} \quad \epsilon_x = \frac{(d_f + d_s)}{2R} \quad (2.2)$$

Where d_f and d_s are respectively the thickness of the film and the substrate. However, if the substrate material has a considerably smaller Young's modulus than the thin film on top, the structure behaves like a composite^{99,100} and the centroid changes:^{67,98}

$$\bar{z} = \frac{(d_f + d_s)(1 + 2\eta + \chi\eta^2)}{2(1 + \eta)(1 + \chi\eta)} \quad \text{with a strain:} \quad \epsilon_x = \frac{(d_f + d_s)(1 + 2\eta + \chi\eta^2)}{2R(1 + \eta)(1 + \chi\eta)} \quad (2.3)$$

Where $\eta = d_f/d_s$, $\chi = Y_f/Y_s$ and Y_f , Y_s are the Young's moduli of the film and substrate respectively. If χ is about 100 as is the case between steel and plastic, the strain can be reduced approximately 5 times compared to the rigid case. Furthermore, if a proper encapsulation layer is selected, the film can be placed at the neutral plane and no strain will be exerted on it upon bending. Selecting an appropriate encapsulation implies fulfilling the relation:⁶⁷

$$Y_s d_s^2 = Y_e d_e^2 \quad (2.4)$$

Where Y_e and d_e are respectively the Young's modulus and thickness of the encapsulation. As it can be seen, there is an interplay between the Young's moduli and the thicknesses of the layers above and below the film. Correspondingly, all the equations above can also be used to estimate the minimum bending radius for a desired critical strain threshold, a common practice in flexible electronics.

2.2 Thin film magnetic field sensors

The fabrication requirements of flexible electronics have opened a new application space for thin film technologies, which were also at the core of the magnetic storage revolution. Magnetic field sensing can be performed with search-coils, flux-gates, superconducting quantum interference devices (SQUIDs) and magnetoresistive devices among others.^{101–103} However, magnetoresistive and Hall effect technologies are the most suitable for thin film fabrication as they do not require bulky parts like coils or cooling systems. Therefore, in this work we have explored the possibilities of these technologies in combination with the electronic skins described above.

2.2.1 Magnetoresistive sensors

In simple terms, magnetoresistance is the change of electrical resistance of a material upon the application of a magnetic field. This pervasive effect was first noticed by William Thomson (Lord Kelvin) while experimenting with iron pieces in 1856.¹⁰⁴ During his tests, he discovered that the electrical resistance of iron decreased when a magnetic field was applied perpendicular to the current and increased when applied along. While this observation would nowadays be classified as anisotropic magnetoresistance (AMR), it marked the beginning of an era of exploration with magnetoresistance. There are many kinds of magnetoresistive sensors depending on the physical nature of their effect; the simplest variety relies on the Lorentz force in conducting or semiconducting materials. This force deflects electrons perpendicularly to the applied current and magnetic field, thereby decreasing the carrier mobility in the material.¹⁰⁵ Magnetoresistive sensors can be considered a large set of devices which have many different physical origins.

2.2.2 AMR sensors

The physical origin of AMR is related with the shift in the energy levels of spin-up and spin-down electrons upon the application of a magnetic field.¹⁰⁶ However, consistent agreement between experiments and theory has not yet been achieved.¹⁰⁷ The main characteristics of this effect in contrast with ordinary magnetoresistance are that it arises in ferromagnetic materials and it is not solely explained by the Lorentz force. One of the clearest pictures of the effect uses spin-orbit coupling to explain the resistance increase for the case of a ferromagnetic sensor film (Fig. 2.3). In this case, applying a magnetic field perpendicular to the current direction deforms the lattice in this orientation and, due to the coupling, aligns the electronic orbitals with the current. The effect of this modification is that the scattering cross-section in the material as well as its resistivity are reduced. Conversely, if the field is parallel to the current, the scattering cross-section and the resistivity are increased.¹⁰⁸ For sensing purposes, it is important to define the anisotropy field H_0 in a sensor stripe, which describes the minimum energy magnetization state. Usually, this state also determines the so called easy axis or the preferential orientation of the magnetization without an external magnetic field applied. The magnetization vector M in the stripe is therefore defined by the interplay of the anisotropy field and any externally applied magnetic field (Fig. 2.4). In a stripe with easy axis along the x axis and an external magnetic field H_y acting only along the y axis, the following relation can be established:

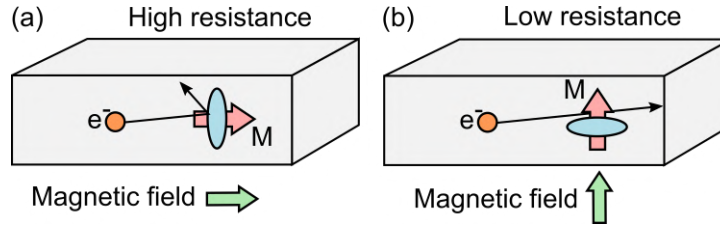


Figure 2.3: **Scattering cross-section change in an AMR film.** Parallel and perpendicular arrangements between the magnetic field and current vectors yield high (a) and low (b) resistive states respectively.

$$\sin(\theta) = \frac{H_y}{H_0} \quad (2.5)$$

Where θ is the angle between magnetization vector M and the easy axis. Typically, the electric current in the sensor is aligned with the easy axis so the angle θ can also be linked to the resistance $R(\theta)$ using:¹⁰⁶

$$R(\theta) = R_{0\perp} + \Delta R \cos^2(\theta) \quad (2.6)$$

Where $R_{0\perp}$ is the minimum resistance (perpendicular to the magnetization) and ΔR is the maximum change in resistance which is usually about 2% for AMR. The angle θ is explicitly defined in this case as that between the magnetization and electric current vectors (Fig. 2.4). Due to their defined angular dependence, AMR devices are readily used as versatile angle and proximity sensors with applications in hard disk read heads, automotive and current sensing.¹⁰¹ The most common materials used for AMR sensing are Ni and Fe alloys, especially permalloy ($\text{Ni}_{81}\text{Fe}_{19}$), as it displays high AMR effect and very low magnetostriction. Key advantages of these sensors are their low cost, noise immunity, fast response (1-5 MHz bandwidth) and ease of integration with silicon-based electronics. Usually, they are thin film deposited and arranged as a Wheatstone bridge,^{109,110} which cancels out unwanted disturbances and maximizes the signal output.^{111,112} Furthermore, if this bridge topology is combined with layout conditioning techniques, AMR sensors can be applied to detect magnetic fields as low as the magnetic field of the earth (25 - 60 μT ¹¹³).

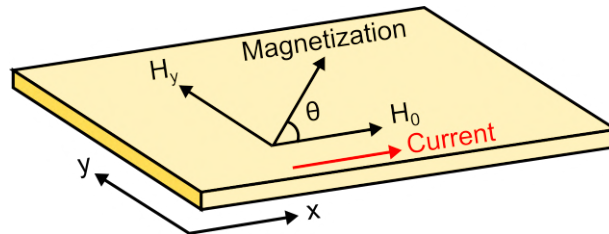


Figure 2.4: Relationship between the magnetization and current vectors in an AMR film.

Geomagnetic field sensing

Detecting the earth's magnetic field or geomagnetic field requires achieving high sensitivity at low magnetic fields ($< 1\text{mT}$), a task out of reach for most magnetoresistive

sensors. However, AMR sensors can be designed to operate at this sensing range with the barber pole biasing method, first proposed by Kuijk and coworkers.¹¹⁴ In this method, a standard AMR stripe is tailored to operate around an angle θ of 45° , where the sensor response is highly linear.¹⁰¹ To do so, skewed slabs of highly conducting material are added on the stripe at a 45° angle with respect to the easy axis. This modification assures that the current will flow at 45° with respect to the magnetization in the stripe. Such a behavior is valid as long as the external field is smaller than the anisotropy field H_0 , otherwise non-linear or flipping effects might arise.

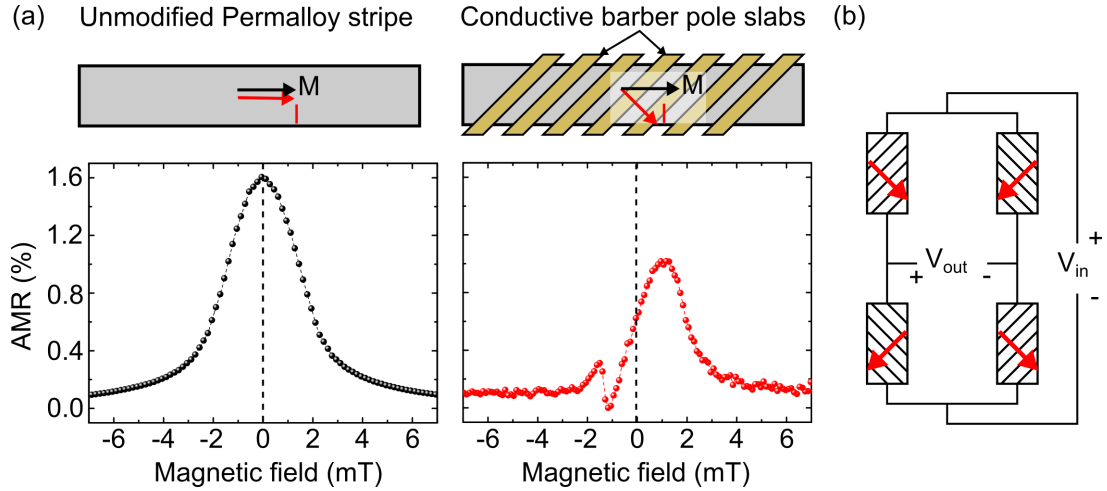


Figure 2.5: **Barber pole modification and Wheatstone bridge arrangement.**

(a) Arrangement of the current and magnetization vectors in an unmodified permalloy stripe. The AMR response displays a symmetric bell-like response (left panel). Upon modifying the permalloy stripes with 45° skewed conductive stripes, the AMR response becomes antisymmetric about zero magnetic field (right panel). (b) Wheatstone bridge configuration used to maximize the output voltage. The electric current orientations on each of the barber pole modified sensors are indicated by red arrows.

To illustrate the effect of the barber pole, equation AMR can be reorganized as a function of the maximum resistance $R_{0\parallel}$ (parallel to the magnetization) to yield:

$$R(\theta) = R_{0\parallel} + \Delta R \sin^2(\theta) \quad (2.7)$$

Next, by combining equation 2.5 with equation 2.7 the resistance as a function of the external magnetic field H_y can be defined:

$$R(H_y) = R_{0\parallel} + \Delta R \left(\frac{H_y}{H_0}\right)^2 \quad (2.8)$$

This equation describes the standard response of an AMR stripe without barber pole modification. Upon applying the barber pole method a 45° shift is introduced so that $R(\theta)$ and $R(H_y)$ become:

$$R(\theta)_{45^\circ} = R_{0\parallel} + \Delta R \sin(\theta) \cos(\theta) \quad , \quad R(H_y)_{45^\circ} = R_{0\parallel} + \Delta R \frac{H_y}{H_0} \sqrt{1 - \left(\frac{H_y}{H_0}\right)^2} \quad (2.9)$$

From equation 2.9 it is clear that for $H_y < H_0$ $R(H_y)$ is a fairly linear function, which can detect sign changes in the magnetic field H_y (Fig. 2.5(a)). These two properties are ideal to detect the geomagnetic field, typically below the anisotropy field of 200 μT to 1 mT in permalloy.^{115–117} Another advantage of the barber pole method is that changing the orientation of the conducting slabs from 45° to 135° flips the sign of the ΔR term in equation 2.9. Using this property in a Wheatstone bridge configuration yields maximum output voltage if adjacent elements in the bridge have opposite slab orientations (Fig. 2.5(b)). Under such condition the output voltage of the Wheatstone bridge is given by:

$$V(H_y) = V_{in} \frac{R(H_y)_{45^\circ} - R(H_y)_{135^\circ}}{R(H_y)_{45^\circ} + R(H_y)_{135^\circ}} = V_{in} \frac{\Delta R}{R_{0\parallel}} \frac{H_y}{H_0} \sqrt{1 - \left(\frac{H_y}{H_0}\right)^2} \quad (2.10)$$

This equation shows that the output voltage of the bridge is linear with the external magnetic field H_y and readily allows detecting the geomagnetic field.

Planar Hall effect

Another aspect of AMR sensing which is often overlooked is the planar Hall effect (PHE)¹¹⁸ which appears as a transversal voltage during AMR measurements. To illustrate this, we can consider a uniform current I_x circulating through a bar-shaped ferromagnetic thin film of thickness t , which produces a transverse voltage V_y given by:¹¹⁹

$$V_y = \frac{I_x \Delta \rho \sin(2\theta)}{2t} \quad (2.11)$$

Where $\Delta \rho = \rho_{\parallel} - \rho_{\perp}$, with ρ_{\parallel} and ρ_{\perp} are the resistivities parallel and perpendicular to the magnetization direction. Furthermore, the magnetic thin film is assumed to be in a single domain state with an in-plane magnetization along the unit vector $\hat{M} = (\cos\theta, \sin\theta)$. This expression is only valid for a Hall bar with infinitesimal voltage probes, however it reflects the expected angular dependence in PHE sensors. Considering a ferromagnetic film with a magnetic anisotropy forcing the magnetization to be in the film plane; when an electrical current circulates through the film along the x axis, the longitudinal (E_x) and transverse (E_y) electric fields can be derived using the resistivity tensor:¹²⁰

$$\begin{bmatrix} E_x \\ E_y \end{bmatrix} = \begin{bmatrix} \rho_{xx} & \rho_{xy} \\ \rho_{yx} & \rho_{yy} \end{bmatrix} \begin{bmatrix} J_x \\ 0 \end{bmatrix} \quad (2.12)$$

$$\text{with: } \rho_{xx} = \rho_{\perp} + (\rho_{\parallel} - \rho_{\perp}) \cos^2(\theta) \quad (2.13)$$

$$\text{and } \rho_{xy} = \frac{1}{2}(\rho_{\parallel} - \rho_{\perp}) \sin(2\theta) \quad (2.14)$$

Even though the magnetoresistance effect is of the same magnitude for both AMR and PHE, the resistance variation for the AMR case evaluates to a non-zero value at zero field. This fact makes AMR devices more susceptible to thermal noise and thermal drifts,¹²¹ while yielding an effective sensitivity of zero at small magnetic fields. On the other hand, when measuring the transverse voltage (PHE voltage), the response of the PHE sensor devices is intrinsically linear and lies on a zero

baseline. These properties are ideal for detecting small magnetic fields without the need of additional conditioning as for barber-pole-based sensors.

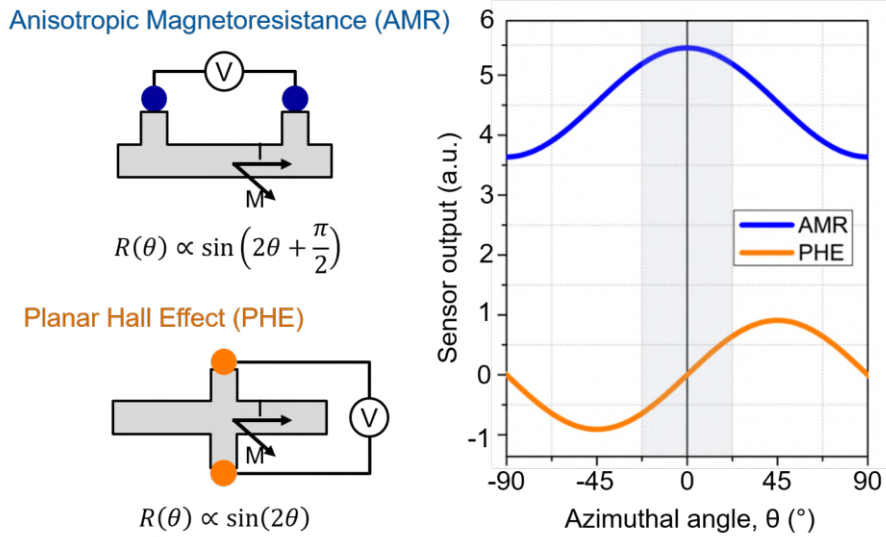


Figure 2.6: **Planar Hall effect measurement scheme and magnetoresistive response.** Figure adapted from. ⁴²

2.2.3 Giant magnetoresistive (GMR) sensors

The discovery of giant magnetoresistance by the groups of Fert ¹²² and Grünberg ¹²³ marked the beginning of the magnetic storage revolution, leading to the wide-spread use of GMR sensors. The main advantage of GMR sensors is that they display a larger effect (up to 150% ¹²⁴) compared to AMR sensors (2%). This improvement allowed smaller magnetic regions and weaker signals to be detected, thus improving the capacity and performance of modern hard disks. The GMR effect arises in magnetic multilayered systems with intercalated ferromagnetic and non-magnetic conductors. In such systems, a parallel or antiparallel alignment between the magnetization vectors of the ferromagnetic layers leads to large magnetic field-dependent changes in electrical resistance (Fig. 2.7(a)). This alignment is mainly due to two prominent effects; exchange interlayer coupling and spin-dependent scattering.

Exchange coupling

Exchange coupling is based on the energetically favorable alignment of ferromagnetic layers depending on the thickness of the spacer (non-magnetic) layer (Fig. 2.7(b)). For certain thicknesses, the magnetization of the ferromagnetic layers will be parallel (ferromagnetic coupling) and for other thicknesses it will be antiparallel (antiferromagnetic coupling). This phenomenon was first reported in by Grünberg et al. in 1986 ¹²⁵ for a Fe/Cr/Fe system, where they noticed the vital importance of the Cr spacer layer thickness. Some years later, Parkin et al. ¹²⁶ first realized that the dependence of the coupling had an oscillatory nature as a function of the spacer thickness. These works were followed by the report of a 65% GMR effect in a Co/Cu system at room temperature, ¹²⁷ which propelled the industrial applications of GMR sensors. The most successful model for understanding this effect is based

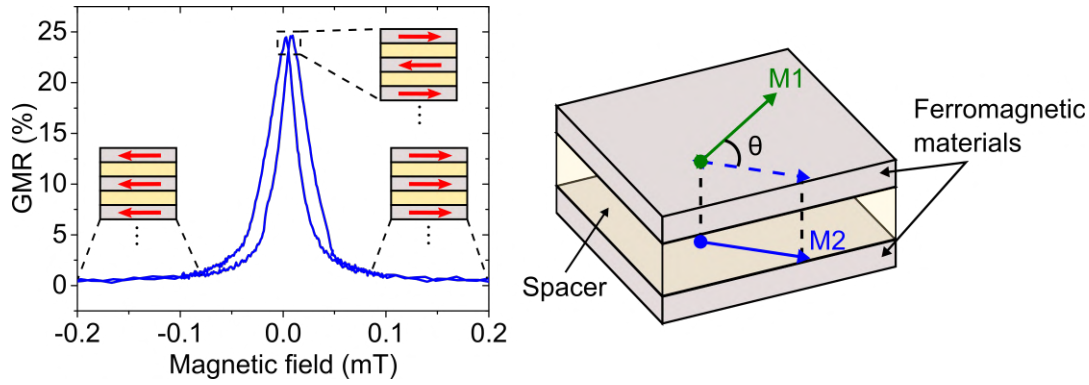


Figure 2.7: **GMR effect and exchange coupling in multilayered systems.** (a) Typical GMR response of a Co/Cu multilayer. Parallel and antiparallel magnetization alignments respectively lead to low resistance and high resistance states. (b) Schematic showing the most important parameters of the exchange coupling mechanism. The coupling energy depends on the angle between magnetizations of the intercalating ferromagnetic layers and the spacer thickness.

on the Ruderman-Kittel-Kasuya-Yosida (RKKY) theory,^{128,129} which attributes the oscillations to spin-dependent quantum interference in the spacer layer. Using the predictions of the model, it can be conveniently estimated for which spacer thickness there will be a ferromagnetic or antiferromagnetic coupling (Fig. 2.8(a)).

Spin-dependent scattering

Originally, the GMR effect was thought to be tightly linked with exchange coupling; however, several studies in the early 90s^{130,131} reported GMR effects even in its absence. Therefore, the observed results had to be related to another phenomenon. So far, the most commonly accepted explanation is spin-dependent scattering due to the exchange-split band structures in ferromagnetic materials. This scattering can be qualitatively understood through the Mott model, originally proposed for explaining resistance increase in ferromagnetic materials when heated above Curie temperature.¹³² The model introduces 2 basic postulates: (i) Electrical conductivity in metals can be thought to have two independent conducting channels, respectively formed by the spin-up and spin-down electrons. These two channels do not mix as spin-flip scattering processes are far less probable than those which conserve spin. (ii) For ferromagnets, the scattering rates for spin-up and spin-down electrons differ and are highly affected (exchange-split) by the magnetic moment of the material. Therefore, ferromagnets with a particular magnetic orientation will weakly scatter electrons with certain spin and strongly scatter those with the opposite spin. Using Mott's formalism, the resistance of a GMR multilayer can be modeled as parallel resistances which have a preferential (spin-up or spin-down) scattering orientation (Fig. 2.8(b) and (c)). In the simplest case of two ferromagnetic layers and a spacer layer, two possible scattering scenarios can arise. First, if both ferromagnetic layers are assumed to preferentially scatter spin-down electrons (parallel magnetizations); spin-up electrons experience very little resistance and spin-down electrons very high resistance (Fig. 2.8(b)). On the other hand, if the magnetizations are antiparallel, spin-up and spin-down electrons are both eventually scattered in one of the layers, resulting in a higher resistance overall (Fig. 2.8(c)).

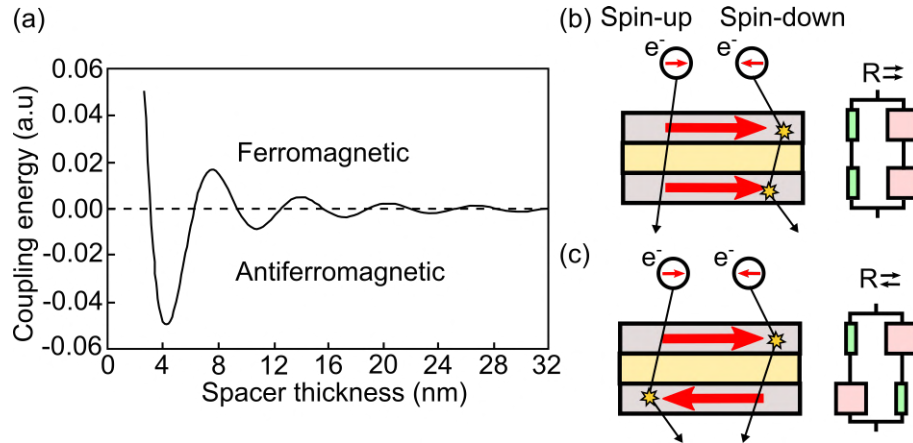


Figure 2.8: **RKKY coupling and Mott model.** (a) Schematic showing the oscillatory dependence of the RKKY coupling as a function of the spacer thickness for a Co/Cu multilayer. (b) Parallel magnetization alignment and equivalent Mott model circuit. The two resistance branches respectively correspond to the spin-up and spin-down channels. In this parallel alignment the spin-up electrons experience low resistance (green squares) and spin-down electrons high resistance (red squares) in both ferromagnetic layers. (c) An antiparallel alignment eventually creates a high resistance state (red squares) in either of the layers for both spin-up and spin-down electrons. The overall resistance in this case is higher compared to the case described in (b).

2.2.4 Spin-valves

First proposed in 1991 by Dieny et al.,¹³³ spin-valves are a special GMR configuration which introduces an additional antiferromagnetic (AFM) layer to define a preferential magnetization axis. The typical structure of a spin-valve consists of a GMR ferromagnetic/non-magnetic/ferromagnetic trilayer (Fig. 2.9(a)), where one of the ferromagnetic layers is in contact with an AFM layer. Because of this arrangement, the magnetization of the ferromagnetic layer close to the AFM layer gets pinned by means of the exchange bias effect.¹³⁴ To complete the process, the growth of the whole device is performed under a magnetic field, which fixes a preferential orientation, i.e., biases the system. As the ferromagnetic layer farthest away from the AFM layer is not affected by the exchange bias, it is referred to as the free layer (its magnetization is easier to switch). The free and pinned layers are essential to understand the magnetoresistive behavior of spin-valves.

Magnetoresistive behavior

The magnetoresistive response of spin-valves differs from common multilayered GMR systems due to the unidirectional anisotropy resulting from the exchange bias effect. This anisotropy is responsible for an asymmetric MR response (Fig. 2.9(b)), in contrast to the normally symmetric one of GMR multilayers (Fig. 2.7). The typical MR plot of a spin-valve is shown in figures 2.9 (b) and (c), where the most important parts of its response are highlighted. The first critical point is the interlayer coupling H_e between ferromagnetic layers, at this field, the spin-valve switches from a low resistive to a high resistive state. The second checkpoint is the exchange bias field

H_{eb} or the magnetic field required to switch the pinned layer and decrease the resistance again. The linearity of the switching is mainly determined by the coercivity of the free layer H_{cf} , also called the minor loop of the spin-valve (Fig. 2.9(c)). This coercivity is very important if the spin-valve is to be employed as a linear sensor. Finally, the parameter H_{cp} refers to the coercivity of the pinned layer, represented by the so called major loop of the spin-valve.

Crossed anisotropy

To use spin-valves for sensing it is desirable to reduce the hysteresis during switching, this means reducing the coercivity of the free layer H_{cf} . To accomplish this, a cross anisotropy configuration is commonly used, a concept originally proposed by Rijks and coworkers in 1994.¹³⁵ In this configuration, the exchange bias axis is defined perpendicular to the easy axis of the free layer. By including this modification, the free layer magnetization coherently rotates 90° and the hysteretic behavior is substantially reduced, as no domain wall motion is involved^{135,136} (Fig. 2.9(d)).

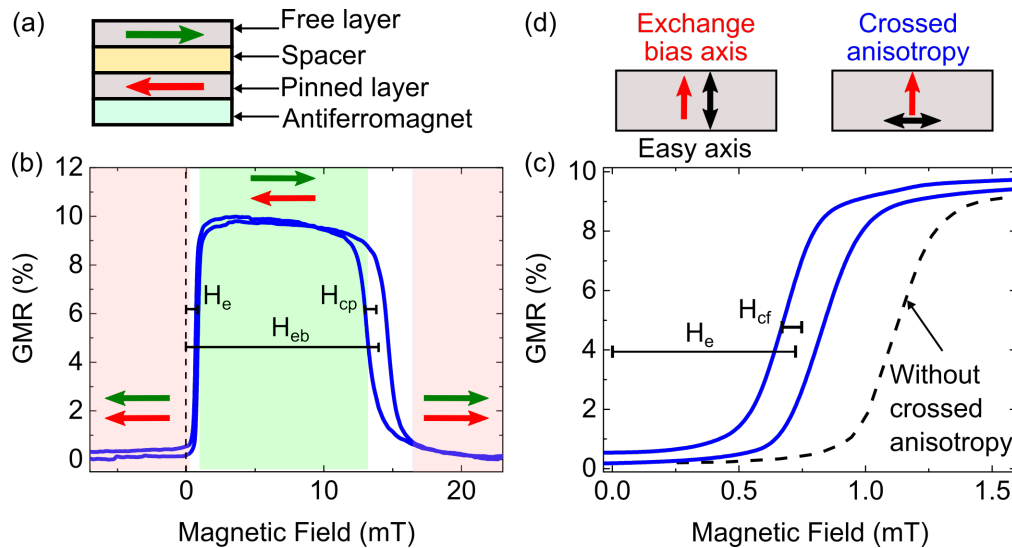


Figure 2.9: **Spin-valve working principles.** (a) Standard spin-valve layer stack. (b) Typical GMR response of the spin-valve in (a). The operating region of the spin-valve is highlighted in green. Red and green arrows show the alignment of the free and pinned layers at each magnetic field region. (c) Zoomed image of the minor loop in (b) highlighting the interlayer coupling H_e , the coercivity of the free layer H_{cf} and the effect of a crossed anisotropy configuration. (d) Schematic describing the orientation of the exchange bias and easy axis in an unmodified spin-valve (left) and a spin-valve with crossed anisotropy (right).

Spin-valve based angular sensors

Similarly to AMR sensors, GMR based sensors can be employed to detect the angle (orientation) of an external magnetic field. However, spin-valves have been particularly studied as angle sensors due to their constant resistance operation range at magnetic fields between H_e and H_{eb} . Within this range, the variation of the resistance is only influenced by the angle of the magnetic field, unlike GMR multilayers,

which are influenced by angle and intensity. Several works have explored the angular dependence of resistance in spin-valve systems,^{112,137,138} which is given by the following expression:¹³⁸

$$R(\theta) = R_p + \frac{R_{ap} - R_p}{2}(1 - \cos(\theta)) \quad (2.15)$$

Where R_p and R_{ap} are respectively the resistance when the magnetizations of the free and pinned layers are parallel and antiparallel to each other. The angle θ is defined between the magnetization of the free layer and the exchange bias direction. Equation 2.15 shows that the unlike in AMR sensors, the resistance in spin-valves is proportional to $\cos(\theta)$, which allows them to detect angles in the full 360° range. Another advantage of spin-valves is their inherent anisotropy due to the exchange bias, which gives them a sense of directionality. This property is usually exploited by combining several spin-valves in a Wheatstone bridge configuration^{109,110} to achieve maximum signal output and cancel intrinsic thermal effects. This can be illustrated by looking at the typical output of a Wheatstone bridge consisting of resistances R_1 to R_4 (Fig. 2.10):

$$V_{out} = V_{bias} \frac{R_1 R_3 - R_2 R_4}{(R_1 + R_2)(R_3 + R_4)} \quad (2.16)$$

Usually, if the nominal value of all resistances is the same, the output voltage is 0 under no external stimuli, which is desirable for sensor conditioning. However, in the case of spin-valves, their anisotropy brings another benefit if they are arranged so that adjacent elements in the bridge have opposing orientations (Fig. 2.10). Under this condition, the output of the bridge can be rewritten in terms of $R(\theta)$ and $R(\theta + 180^\circ)$, assigning the same nominal resistance of R_1 to all elements:¹¹²

$$V_{out} = V_{bias} \frac{R_1^2(\theta) - R_1^2(\theta + 180^\circ)}{(R_1(\theta) + R_1(\theta + 180^\circ))^2} = V_{bias} \frac{R_1(\theta) - R_1(\theta + 180^\circ)}{R_1(\theta) + R_1(\theta + 180^\circ)} \quad (2.17)$$

In Equation 2.17, if $R_1(\theta)$ is at its maximum, $R_1(\theta + 180)$ is at its minimum and the output variation is twice the total change of a single element (Fig. 2.10). Thus, this configuration maximizes the signal output of the bridge. Finally, to complete a full-fledged angle sensor, an identical Wheatstone bridge is fabricated perpendicular to the first one to provide an output proportional to $\sin(\theta)$. The angle of the external magnetic field or measured angle α can then be calculated using the trigonometrical relationship:

$$\alpha = \tan^{-1}(\theta) = \frac{V_{sin}}{V_{cos}} \quad (2.18)$$

Where V_{sin} and V_{cos} are the output voltages of the two perpendicularly placed Wheatstone bridges. Using this relationship, spin-valve angle sensors can reconstruct absolute angles over 360° , an improvement over AMR based angle sensors which are intrinsically limited to 180° .

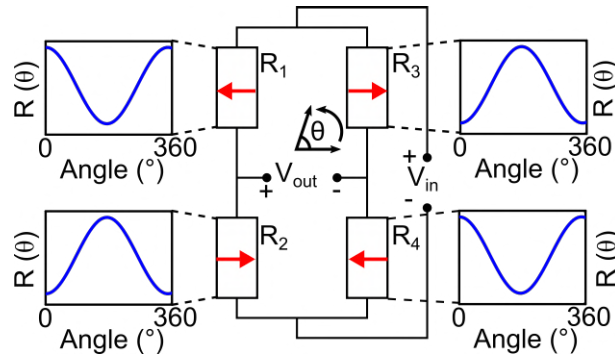


Figure 2.10: **Spin-valve-based Wheatstone bridge.** Required exchange bias orientations to maximize the signal output. Small inset plots indicate the angular dependence of each of the single spin-valves. As adjacent components have opposite exchange bias orientations, their respective maxima and minima overlap and enhance the differential output.

2.3 Interactive devices and human-computer interfaces (HCI)

2.3.1 Early stages

One of the main aspects which this thesis explores is the interaction between humans and computers using magnetic fields from the surroundings. However, interactivity and the need to communicate with computers started far back with very different mechanisms and devices, giving birth to what is now HCI. The term HCI is sometimes also defined as human-computer interaction,^{4,139,140} which is essentially equivalent to human-computer interfaces, in the context of this work. The history of HCI started in 1963 with the breakthrough PhD thesis of Ivan Sutherland,¹⁴¹ where he first demonstrated direct manipulation of objects on a screen. His system, called the Sketchpad was a multifunctional “light pen” capable of writing, moving and scaling objects, among other functions. During the years to follow, many input devices and user interfaces were conceived to enable basic human-computer interactions. Concepts like the modern mouse and multiple tiled windows were developed as part of the NLS (“oN-Line System“) project, and demonstrated in 1968 by Engelbart and coworkers.^{142,143} Projects like Newman’s 1967 Reaction Handler¹⁴⁴ introduced one of the earliest versions of a “widget”, a graphical potentiometer for dial-like control dubbed “Light Handles”.¹⁴⁰

Later on during the 1970’s, Xerox PARC (Palo Alto Research Center) established most of today’s interfaces for object manipulation in a computer and formulated the “WYSIWYG” (what you see is what you get) approach. This concept set the base for ubiquitous direct manipulation interfaces with text and drawing capabilities, as envisioned by Alan Kay in his 1977 article about the Dynabook.¹⁴⁵ The capabilities of the Dynabook as described by Kay, strongly resemble the interactivity and functions of today’s laptops and tablets. Building upon this knowledge, Xerox released the Xerox Star in 1981 and was followed by Apple’s Lisa (1982) and Macintosh (1984), the first commercial systems with “Direct Manipulation”. This term was coined by Ben Shneiderman in 1983¹⁴⁶ and it means the “replacement of complex command language syntax by direct manipulation of the object of interest”. This concept is at

the core of most computer programs nowadays and it is partly responsible for the wide-spread use and increased accessibility of personal computers.

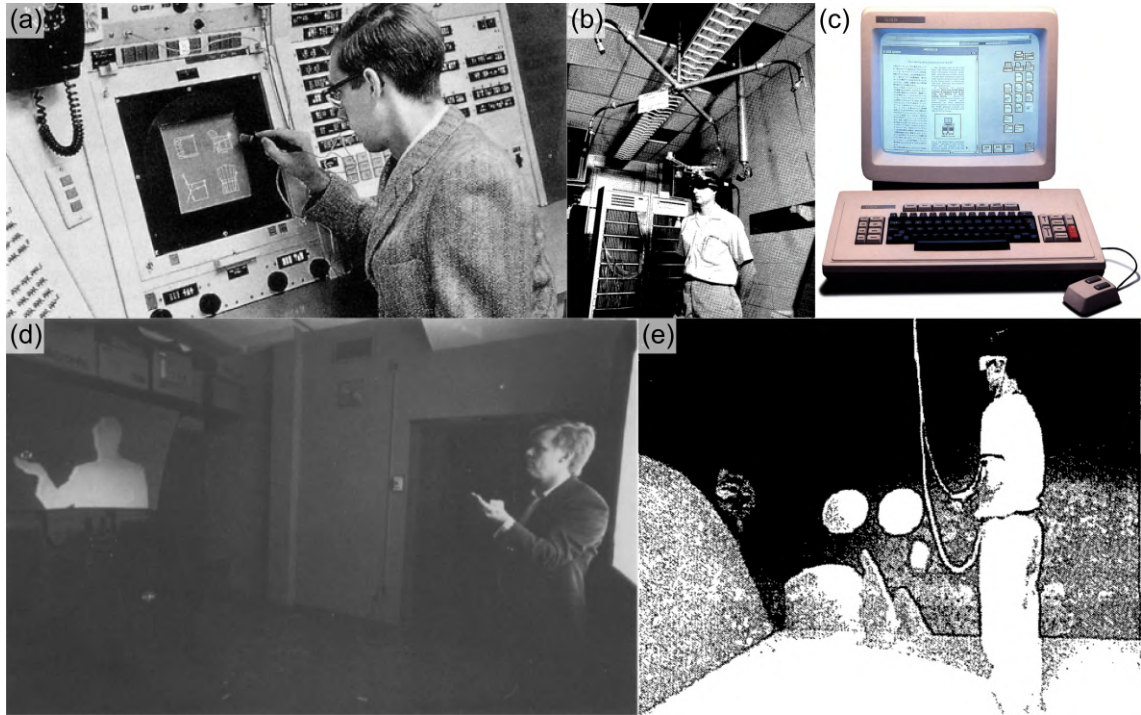


Figure 2.11: **The early years of interactive devices and VR.** (a) Sketchpad, the first interactive device created by Ivan Sutherland in 1963.¹⁴¹ Image taken from[BIM blog]. (b) The sword of Damocles, the first head mounted virtual reality system.¹⁴⁷ (c) The iconic Xerox Star computer, the first commercial product introducing human machine interactivity.¹⁴⁸ (d) VIDEOPLACE, the first VR system utilizing interactive silhouettes as “characters”.¹⁴⁹ (e) CAVE, the first VR system using stereoscopic projection for a full room-scale experience.¹⁵⁰

2.3.2 Beyond standard interactions

During the 60s and 70s, designers realized that there were many interaction modes which were still unexplored and could potentiate the user experience. Suddenly, futuristic concepts such as gesture control,¹⁵¹ multi-media, 3D animation,¹⁵² VR,¹⁵³ cooperative computing¹⁴³ and even speech recognition¹⁵⁴ started to become true.¹⁵⁵ Very important milestones like the RAND tablet,¹⁵¹ a precursor of gesture-controlled devices, and the Lincoln wand,¹⁵⁶ a 3D location sensing system, set the table for novel interactions. However, the most visionary work was Ivan Sutherland’s paper *The ultimate Display*¹⁵³ in 1965, which already proposes an artificial world with multisensorial stimuli and force feedback. This work is considered the conceptual origin of VR, and would be materialized three years later when Sutherland himself built *The Sword of Damocles*, the first VR head-mounted display (HMD) system.¹⁴⁷

In the next years, several VR systems were invented to improve the artificial world that Sutherland had originally envisioned. Works like Myron Krueger’s VIDEO-PLACE in 1975, which allowed users to interact with virtual silhouettes, expanded on the development of virtual worlds. Further devices like the popular DataGlove

(1985) and BOOM (1989) established themselves as VR dedicated consumer products. Also in 1989, Jaron Lanier of VPL Research proposed the term virtual reality, which would later cement itself as a technology field. In 1992, a new kind of VR based on stereoscopic projection was presented; the CAVE,¹⁵⁰ allowed users to experience a high resolution room-scale experience without an HMD. Then, in 1993 Feiner and coworkers introduced the term augmented reality¹⁵⁷ as “presenting a virtual world that enriches, rather than replaces the real world”. In this paper, AR was presented as a way to ease printer maintenance by providing visual cues to guide the user. However, the bulkiness, high cost and complexity of VR and AR technologies prevented them from spreading and reaching the public. By the early 2000s, almost all interest in these technologies had faded. It took about a decade for a new generation of much cheaper and accessible hardware to appear and spur the current revival of AR and VR. The first device of this new era was the Oculus Rift (DK) 1 released in 2012, an HDM device which has set the tone for many other competitors and iterations. In the last years, a plethora of VR and AR devices like the HTC Vive, Google Cardboard, Samsung Gear VR, Microsoft HoloLens, among others; have been released.¹⁵⁸ The relative success of this last wave of VR products is enabled by the low cost and availability of consumer electronics nowadays. These advantages have allowed manufacturers to deliver affordable VR sets and use the already pervasive smartphones as VR/AR projecting systems.¹⁵⁹

On the side of gestural interfaces, from the mid-2000s we have seen an explosion of devices based on touch and motion tracking. Some of the most prominent examples are Nintendo’s Wii console (2006), Apple’s iPhone and iPod touch (2007) and numerous touchscreen mobile devices which have been released since 2008.¹⁶⁰ All these products initiated a technological revolution which has led to the current smartphone and tablet era. Furthermore, motion capture systems have emerged as a standard tool for gaming environments, sports training, animation and even art.¹⁵⁸ In these systems, sets of infrared (IR) cameras digitize movement and transfer it to computers or gaming consoles for manipulating or interacting with objects. In the last years, systems like the Leap Motion controller, Microsoft Kinect and Intel’s Real Sense Camera; have enabled more real and smoother interactions. Current efforts are focused on the integration of haptic systems with VR to deliver a more complete experience to the users.^{161–163}

2.3.3 Interactive devices based on magnetic fields

While IR motion capture systems are very popular nowadays, there are many other sensing technologies available to build interactive devices based on human motion. Mechanical, inertial, acoustic, magnetic and optical sensors have all intrinsic advantages and disadvantages, which implies that the best tracking solutions should use a combination of them.^{158,164,165} Building upon the expertise of our group with magnetic field sensors,¹⁸ we have focused our research on achieving interactivity through magnetic field detection. Also, magnetic field sensors have desirable characteristics for interactive devices; compactness, no requirements for line-of-sight, and single-source or even source-less (using the geomagnetic field) detection.¹⁶⁴ Magnetic or electromagnetic tracking systems have been in use at least since 1969 when Polhemus Navigation Systems developed head tracking systems for the military [PolhemusHist]. In the 80s and 90s, they were mainly employed in kinesiological



Figure 2.12: **The new era of VR devices and haptics.** (a) Modern head-mounted displays. Top row from left to right: Oculus Rift, Steam VR/HTC Vive, and Avegant Glyph, bottom row: Google Cardboard, Samsung Gear VR and OSVR HDK. Image taken from. ¹⁵⁸ (b) Reactive Grip Motion Controller by Tactical haptics. This device includes tangential motion and skin stretching capabilities to recreate the grip sensation in VR environments. (c) The Tactai Touch™ system by Tactai. This system acts on the fingertips of the user to mimic the sensations of pressure or texture during VR interactions (d) The VR touch system by GoTouchVR. It operates similarly to the Tactai Touch, using vibrating actuators to stimulate the skin. Pictures (b) to (d) are taken from. ¹⁶³

studies,^{166–168} rehabilitation¹⁶⁹ and human motion.¹⁷⁰ In the last 20 years, the development low-cost wireless systems and compact inertial sensors, has boosted the performance and convenience of the experiments done in previous decades. This has been enabled by the appearance of magnetic and inertial measurement units (MIMUs) which allow for unconstrained motion monitoring.^{171,172} Numerous applications have emerged as possible alternatives to optical systems in gait analysis,¹⁷³ medicine¹⁷⁴ and all kinds of human motion.^{175,176} However, most of these technologies utilize AC magnetic fields rather than the “pure” DC magnetic fields of permanent magnets. Therefore, their complexity, footprint, weight and power consumption increase dramatically compared to DC devices. As we move forward, wearable and interactive devices are becoming lightweight, seamless and compliant to the human body.^{47,163} Under these conditions, magnetic sensing schemes must adapt to be also flexible, soft, lightweight and portable. The first steps towards this vision had been given by Parkin et al. who first grew GMR multilayers on Kapton¹⁷⁷ and Mylar,¹⁷⁸ yet, with a reduced performance. The next step was given by Chen et al. in 2008,¹⁷⁹ who significantly enhanced the response of GMR sensors on flexible substrates. Some years later, Melzer and coworkers created the first stretchable magnetoelectronic sensors based on GMR multilayers on PDMS.¹⁸⁰ Ensuing works on stretchable spin-valves,¹⁸¹ printable magnetoelectronics,^{182,183} flexible magnetoelectronic analytical platforms,¹⁸⁴ transfer printable magnetic field sensors;¹⁸⁵ consolidated the field of flexible and stretchable magnetoelectronics. The next milestone for interactive devices came in 2015 when Melzer et al. demonstrated wearable interactive devices based on Hall effect sensors.¹⁶ This work first hinted towards interactive pointing devices which could be worn as an electronic skin and even map the surrounding magnetic field. Further developments led to the breakthrough paper in 2015¹⁷ by Melzer and coworkers again, where they introduced the concept of imperceptible magnetoelectronics. This concept enables magnetoresistive sensors to withstand massive deformations while attaching conformably to the human skin and remaining fully functional. Additional efforts have facilitated the on-site conditioning of these flexible magneto electronic circuits, opening the door for higher circuit complexity and integration.¹⁸⁶

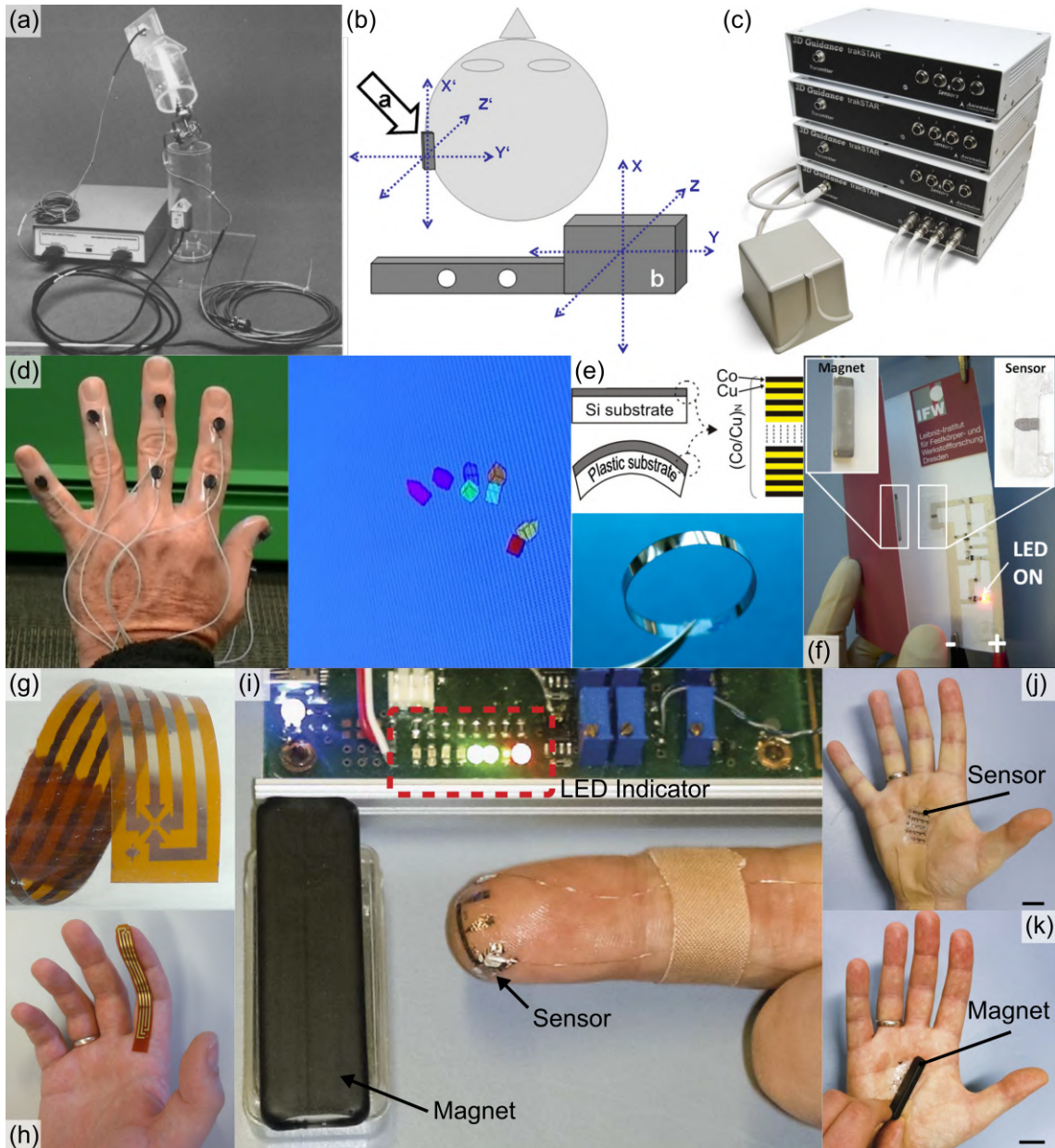


Figure 2.13: **Interactive devices based on magnetic fields.** (a) The 3space Isotrak, an electromagnetic tracker used as a three-dimensional joint simulator for kinesiology.¹⁶⁶ (b) Magnetic tracking using pulsed DC magnetic field and a dynamic reference frame (DRF) sensor for head-tracking during operation. The DRF sensor is shown on the head of the subject and the magnetic source is depicted as a separate unit labeled b.¹⁸⁷ (c) The trakSTAR system by Ascension Technology Corporation. This device tracks motion using a combination of sensors and an electromagnetic source.¹⁸⁸ (d) Polhemus finger tracking demonstration. The general operating principle is the same as for trakSTAR device in (c). (e) First high performance GMR sensors on flexible substrates by Chen et al.¹⁷⁹ (f) An interactive postcard using printable GMR sensors developed by Karhausenko et al.¹⁸³ (g) Freestanding flexible Hall sensor for applications in wearable (h) interactive devices.¹⁶ (i)-(j) Interactive devices based on imperceptible magneto-electronic sensors which seamlessly attach to a finger or a hand palm to enable magnetic cognition.¹⁷

Chapter 3

Fabrication and characterization techniques

This chapter discusses the main tools and processes required to manufacture and characterize magnetosensitive e-skins. The following sections are organized in a sequential manner to describe the typical fabrication workflow: device design, photolithography, thin film deposition and characterization of device properties.

3.1 Device design

The fabrication process always starts in the mind of the designer, who must find a way to satisfy the functional requirements of the device to be created. Designing a working prototype is part of a constant refinement process which can involve several iterations. Therefore, before committing to any computational drawing tools, it is important to start by sketching the design on a piece of paper. This approach greatly simplifies the search for fundamental mistakes and enhances the creative process. It is here that parameters like materials, dimensions and interconnections must be carefully thought through to avoid redesign issues later. Once a consistent design is selected, it can be transferred to a computational drawing. The most common tools for advanced computational drawing are grouped under the umbrella of computer-aided design (CAD) software. This kind of software allows the user to create and debug complex 2D and 3D patterns with relative ease. In this work we have used CAD tools like QCAD and AutoCAD to design the 2D structures required for my designs. The typical procedure involves creating polygon-based shapes within the software (Fig 3.1, left)), which represent the regions where a specific material will be deposited or not during the ensuing photolithography (Fig 3.1, center). An output file containing this information is then exported to a laser writing system which creates a photolithographic mask or directly writes the pattern. At the end of the photolithographic process, the vision which started in the mind of the designer is translated into a patterned material on a substrate (Fig 3.1, right).

3.2 Photolithography

One of the most important techniques utilized in this work is photolithography, the workhorse of the microfabrication industry. As its name indicates, this technique

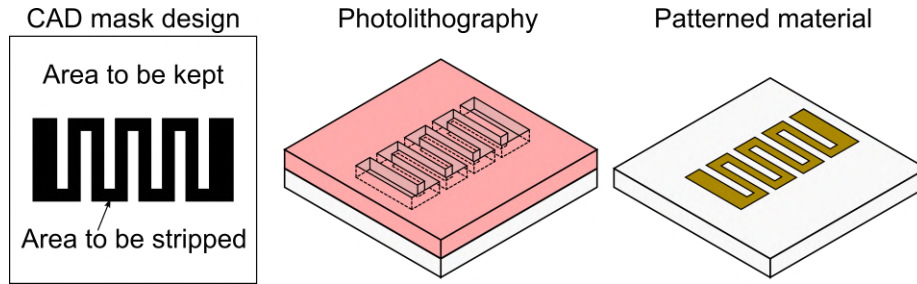


Figure 3.1: **From conceptual design to device fabrication.** A polygon-based CAD design is converted into a physical pattern by means of photolithography.

uses light (photo) to transfer patterns from a master design onto a substrate, just like conventional lithography does. However, because it uses light, its resolution is substantially improved with respect to non-optical lithography, as the resolving limit is mainly determined by the wavelength λ of the light used. Due of this fact, most photolithographic systems use light sources with the smallest possible λ , usually in the UV region of the spectrum.

3.2.1 General process

To start the photolithographic process, a photosensitive polymer resin, called photoresist, must be evenly spread or coated on the substrate. One of the most common and well established methods to achieve this is spin-coating, which we used all throughout this work. This method is carried out in a spin-coater, where the sample is vacuum fixed to a holder. Then, after applying the photoresist on the sample, the coater rotates the sample and the photoresist is spread by action of the inertia opposing the centripetal force (fig 3.2 (a)). The main characteristic of the photoresist is that it becomes soluble or insoluble (in a specific solvent called developer) upon illumination. If the photoresist becomes soluble with light, it is said to be positive tone, on the contrary, if it becomes insoluble it is negative tone (fig 3.2 (b)). This property turns the photoresist into an excellent tool for selectively covering portions of the substrate and allowing for the formation of patterns. Positive photoresists are usually more intuitive to use however, where very precise lift-off process are required, the negative ones excel due to th In this work, we have mainly used positive photoresists like the AR-P 3510 (Allresist GmbH, Germany) and the S1813 (Dow Electronic Materials, USA), due to their availability and ease of use. Also, when higher lift-off precision was required, an image reversal photoresist (AZ5214E, Microchemicals) was used. Due to its inversion capabilities, it ultimately behaves like a negative photoresist, resulting in sharp undercuts which ease lift-off. Once the coating is completed, a pre-exposure bake ensues to dry the still wet content of the photoresist and leave the sample ready for light exposure.

The illumination process is usually performed with mercury lamps, as their spectral lines coincide around the UV region of the spectrum where more photoresists operate (365-436 nm). These lamps are usually integrated in mask alignment systems which allow the user to very precisely align a reflective mask over the target substrate. The mask contains the master design created by the CAD software and is manufactured by etching patterns on a chromium coated glass. Alternatively, the substrate can be directly illuminated without the need for a mask, an approach

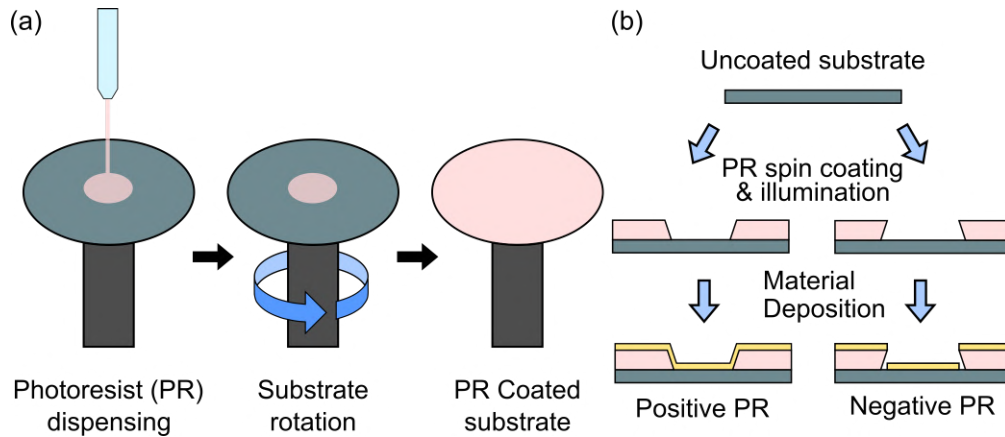


Figure 3.2: **Photolithographic process.** (a) Spin coating working principle (b) Workflow of the photolithographic process. The schematic shows the two possible structure outcomes when using a positive or negative photoresist and how it affects the pattern of the deposited material on the substrate.

known as direct laser writing (Fig. 3.3(a)). Both these approaches have been used throughout this thesis, but direct laser writing has been mostly preferred due to its prototyping versatility. The main advantage of using a maskless technique is that several different designs can be tried without having to manufacture a mask for each trial, thus saving in costs and time. The direct laser patterning in this document has been carried out in a DWL 66FS laser lithography system (Heidelberg Instruments, Germany). This device uses a 405 nm laser which is spatially oriented along its main axes of motion by an acousto-optic modulator (AOM) and deflector (AOD) set. Complementary parts like a micro, micro cameras and an interferometrically positioned stage allow extremely precise alignment and positioning of the sample during writing (Fig. 3.3(b)).

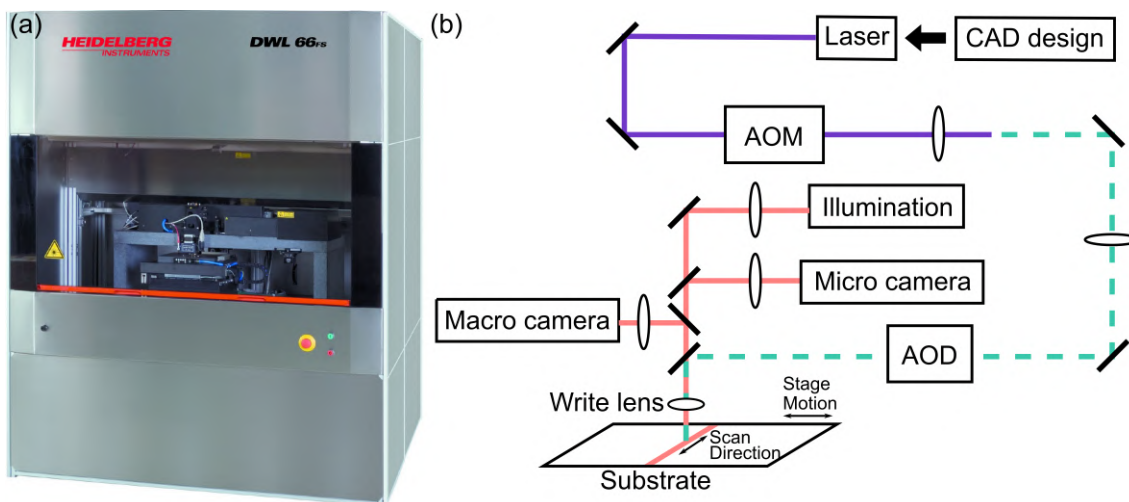


Figure 3.3: **Laser writing process.** (a) Photograph of the DWL 66 direct laser writer using during this thesis. Image taken from the DWL66FS User Guide Part 1. (b) Schematic describing the internal workings of the DWL 66.

After the illumination is completed, the samples are submerged in a developer solution, which washes away the still soluble parts of the photoresist to reveal the

pattern. The developer usually consists of a hydroxide (OH⁻) containing solution which removes the unwanted parts but doesn't attack the patterns on the photoresist. Following the development process, the samples are thoroughly rinsed with deionized water until the photoresist remnants are removed. Finally, the samples are blow dried and they are taken for thin film deposition (see next section). After the thin film deposition is completed, the photoresist underneath the deposited material is removed in a process called lift-off. During this process, the samples are submerged in a strong organic solvent, like acetone or dimethylacetamide (DMAc), which removes the photoresist together with the unwanted parts of the thin film. The remaining parts of the thin film constitute the desired pattern according to the initial design. Next, the samples are rinsed with isopropanol and dried to complete the photolithographic process and get ready for additional photolithographic steps or characterization.

3.2.2 Considerations for ultra-thin substrates

A key aspect of the photolithography performed in this thesis is that all the processes mentioned above must be completed on extremely thin foils (1-10 μm in thickness). The main difficulty with these substrates is their tendency to wrinkle, stick to surfaces and fly away due to their malleable and lightweight nature. This unwanted behavior makes it hard to process them on a flat state, something which is crucial for photolithography. Therefore, during this thesis we have employed the following strategies to try to circumvent these limitations: adhesion-based processing, sacrificial layer-based processing and expansion compensated mask design.

Adhesion-based processing

This approach starts with a rigid substrate like glass or a silicon wafer and uses an intermediary adhesion layer to stick the foil on top (Fig. 3.4(a)). The most straightforward way is to use the capillary force of water as adhesion promoter. In this case, some drops of water are dispensed on the substrate and the foil is placed on top of them. Subsequently, the foil is pushed against the substrate using pressurized air to eliminate all excess of water underneath. As soon as the water dries, the foil on the substrate can be processed as described in the previous section. The main drawback of this approach is that it is only stable if the substrate is larger than the foil, otherwise the corners of the foil will be prone to delamination. The reason for this is that if the substrate is larger, the photoresist goes over the corners of the foil and enhances adhesion and edge protection during photolithography. Also, this method does not produce a very flat surface, especially if the sample size is larger than $2 \times 2 \text{ cm}^2$.

Another adhesion-based strategy is to use an elastomeric adhesive like PDMS to fix the foil on the substrate (fig 3.4(b)). In this case, the PDMS layer is spin-coated and cured on the substrate, which allows the corresponding foil to stick by means of Van der Waals forces. An important part of this process is to pre-stretch the foil before adhering it, so that the final surface is as flat as possible for photolithography. This can be accomplished by using a bi-axial stretching setup or frame where the flatness and tension on the foil can be tuned at will. Once the foil is pre-stretched, it can be brought into contact with the PDMS covered substrate, ensuring a mostly flat substrate.

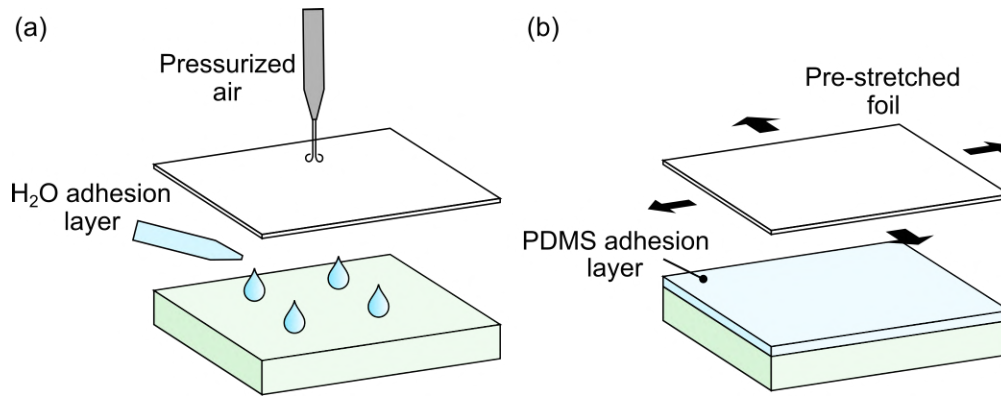


Figure 3.4: **Processing of ultrathin polymer films by adhesion layers.** (a) Schematic of the water mediated adhesion approach. (b) Schematic of the PDMS mediated adhesion approach.

Sacrificial layer-based processing

An alternative to adhesion-based strategies is to use a sacrificial layer for releasing the processed foil at the end of the photolithography. This approach is more robust fabrication-wise, but it is substantially more complex than the ones mentioned above as it involves additional spin-coating and removal steps. A summary of the typical workflow is depicted on Fig. 3.5. The most important elements required are: a sacrificial layer which is resistant to all the chemicals used during photolithography, and a polymer resin which can be spin-coated and cured to form a chemically stable foil.

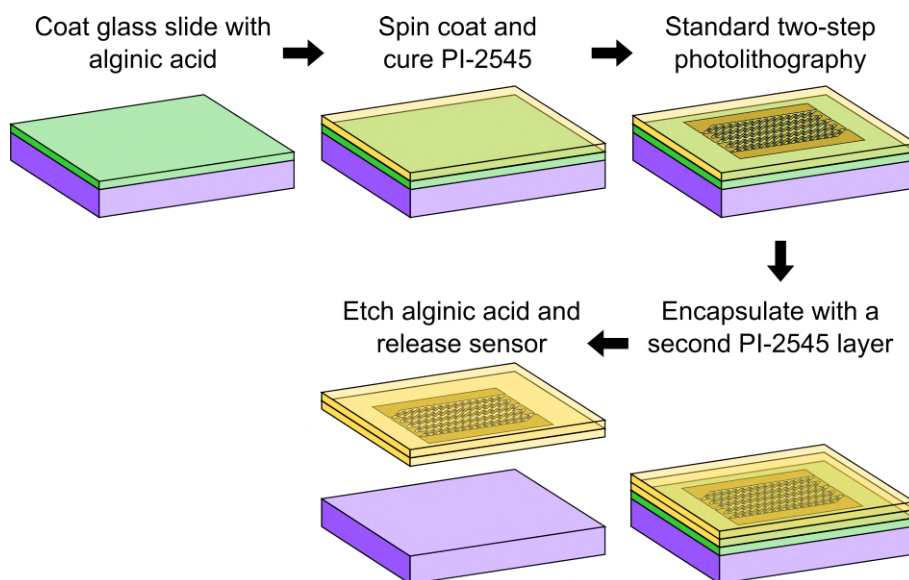


Figure 3.5: **Sacrificial layer processing of ultrathin polymer films.** Processing steps required to obtain a freestanding PI-2545 based sensor.

In this thesis, a method presented by Linder et al.¹⁸⁹ has been adapted in collaboration with Dr. Jin Ge to achieve better functionality. The original method used polyacrylic acid (PAA) crosslinked with calcium Chloride (CaCl_2) as a sacrificial layer. The working principle here is that when PAA binds with the Ca- ions, it be-

comes water insoluble and not easily attacked by the photolithographical chemicals. However, upon contact with a sodium chloride (NaCl) solution, the higher affinity of the Na⁻ ions renders the PAA water soluble again. This property is used to establish a steady and reversibly soluble sacrificial layer. For this work, we have used alginic acid instead of PAA, as we have observed that PAA tends to harden very fast and doesn't yield a flat surface. Alginic acid in contrast gives an excellent surface finish while keeping the desired properties mentioned above. As a polymer resin to form a chemically stable foil we have used PI-2545 (Dupont, USA), a versatile polyimide (PI) which is thermally and chemically stable after curing at 200°C. Once cured, the PI coated substrates were processed as in conventional photolithography. Finally, to ensure the integrity of the thin film layers after photolithography, the resulting devices were coated with an additional layer of PI to prevent the NaCl removal solution from etching the metallic thin films.

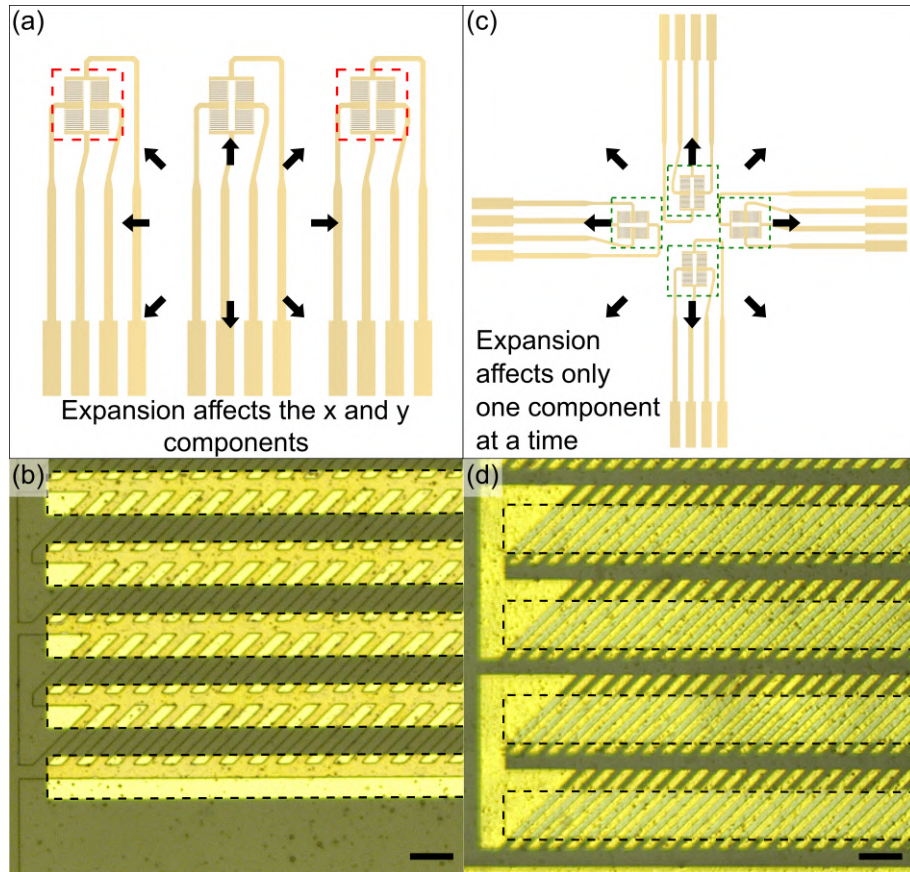


Figure 3.6: **Expansion correction of photolithographic masks.** (a) Initial arrangement of the sensor elements on the mask. (b) Optical micrograph of the observed result after using the mask in (a). The pattern is misaligned with respect to the underlying layer (dotted lines). (c) Schematic of the corrected mask. The sensor elements are now placed close to the center and expansion aligned to minimize distortion. (d) Optical micrograph after using the corrected mask. The skewed structures on top are aligned with the layer underneath (dotted lines). Scale bars in (b) and (d) are 50 μm .

Expansion compensated mask design

Another problem which frequently arises when dealing with flexible polymer films is the unavoidable enlargement of the substrate due to many environmental factors. This phenomenon has been identified before¹⁹⁰ and its causes are usually related with thermal expansion and solvent swelling conditions experienced by the polymers during processing. Such issues severely complicate the layer-to-layer alignment process during photolithography, especially for feature sizes in the low μm and below. During the fabrication of geomagnetic e-skins (see chapter 5), this alignment became crucial for aligning the 10 μm wide structures, which would have otherwise not worked as intended. Therefore, the dimensions and configuration of the mask designs used for fabrication had to be modified to compensate for substrate expansion. First attempts without compensation resulted in severely misaligned and correspondingly non-functional structures influenced by a radial expansion pattern (Fig. 3.6(a) and (b)). These problems were subsequently resolved by increasing the length of the feature in the direction of greatest expansion and by orienting the structures along the expansion gradient (Fig. 3.6(c) and (d)).

3.3 Thin film deposition

The main goal of photolithographic processes is to define patterned layers of functional materials like metals, oxides or semiconductors on a substrate. Therefore, it is crucial to have a method to grow these layers (also called thin films) in a controlled manner. The most common ways to achieve this involve either electrochemistry to grow films in solution or vapor deposition to produce films from the vapor phase. In this work, we have used vapor deposition techniques, particularly physical vapor deposition (PVD) processes, as they were readily available and yield high purity films. The two PVD growth methods we utilized were magnetron sputter and e-beam deposition.

3.3.1 Magnetron sputter deposition

In this method, the substrate to be coated is placed in a vacuum chamber, opposite to a target (the material to be deposited). Next, an inert gas like argon is allowed in the chamber to serve as seed for the sputtering process. As in conventional sputter deposition, the target and the substrate are subjected to opposite electric potentials in the range of hundreds of volts, thus ionizing the incoming gas. However, in this case, magnets near the target encourage the argon ions to mostly collide with the target and release atoms into the chamber. Due to the presence of both electric and magnetic fields, the electrons are forced to travel in spirals (as in a magnetron), significantly increasing the ionization and collision rate near the target. As the gas ions are more massive, they are not as affected by the magnetic trap and directly collide with the substrate, thus sputtering the target atoms. Because of these modifications, the deposition rates of this technique are superior (at the same process pressure) compared with DC or RF sputtering. Finally, the atoms ejected from the target by the highly energetic ions start forming a thin film on the opposing substrate (Fig. 3.7(a)). The properties of the ensuing film can be controlled by tuning the vacuum level and deposition time.

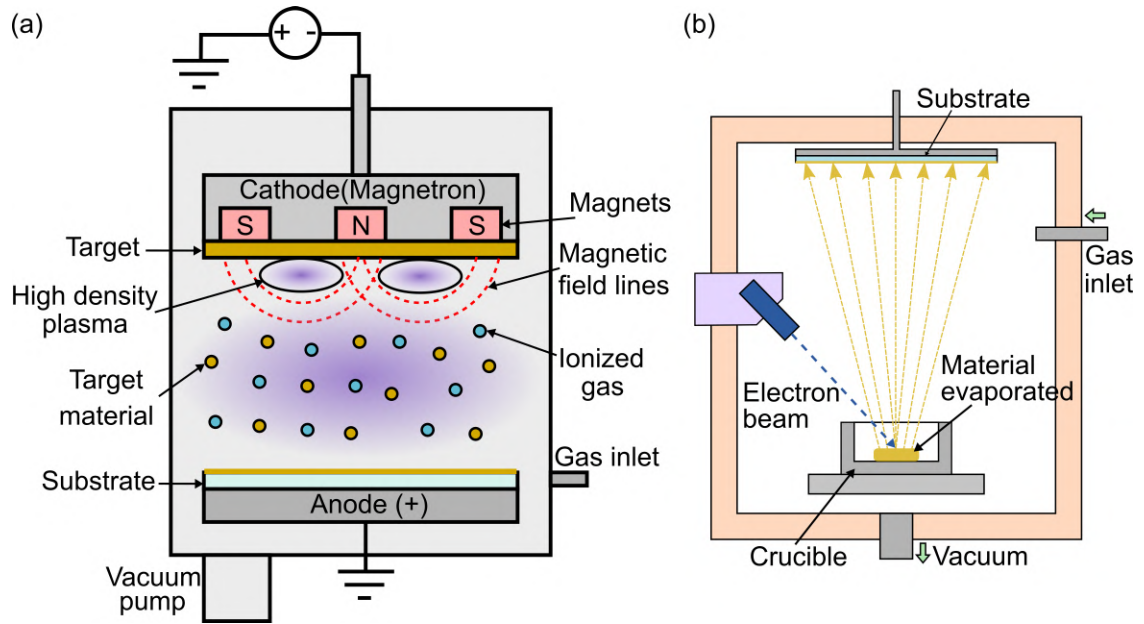


Figure 3.7: **Thin film deposition methods.** Schematics describing the magnetron sputtering (a) and e-beam evaporation (b) processes.

3.3.2 E-beam evaporation

This method uses a different working principle to deposit materials on substrates, as it relies on the evaporation of the “target” material. Very frequently the substrate is placed upside down at the top of the chamber, so that the evaporated material conveniently coats it. In this case, instead of a magnetron to trigger the process, an electron beam is focused on an ingot of the target material inside a crucible. The increased electron flow heats the material, causes it to melt and eventually sublimate, thus producing a vapor which later condensates on the substrate (Fig 3.7 (b)). The evaporation rate can thus be controlled by modifying the intensity of the electron beam current as well as its position and alignment.

3.4 Characterization of device properties

After concluding the fabrication process described in previous sections, it is necessary to verify the functionality of the devices which have been produced. As the devices presented in this work behave as flexible magnetic and thermal sensors, their functionality will be defined by their magneto-resistive, mechanical and thermal properties. In the following subsections, we introduce the setups and techniques used to characterize such properties.

3.4.1 Magneto-resistive characterization

Most of the devices presented in this document are comprise magnetosensitive layers which detect magnetic fields by means of resistance changes. Therefore, measuring electrical properties in the presence of magnetic fields is one of the key characterization aspects of this study. As the operational range of the devices studied is

very broad, the setups presented below are classified according to the magnetic field strength they address.

High magnetic field strength setup

This setup is capable of testing devices which operate in magnetic field ranges of up to 600 mT such as Hall effect or GMR-based sensors. It consists of an electromagnet formed a yoke and two iron pole pieces used to concentrate the field inside the probing area (Fig. 3.8 (a)). The samples are connected by means of a clamping adapter with retractable gold pins, which presses upon the contact pads on the sample (Fig. 3.8(b) and (c)). This adapter is coupled in turn to a NI-6211 (National Instruments, USA) data acquisition box which captures the measured resistance data and generates the control signals for the electromagnet. These signals drive a pair of bipolar BOP power supplies (Kepco, USA), which correspondingly provide the power to regulate the magnetic field of the electromagnet. The data collection is done by an in-house LabVIEW program which can perform magnetic field sweeps while simultaneously measuring the resistance of the sample.

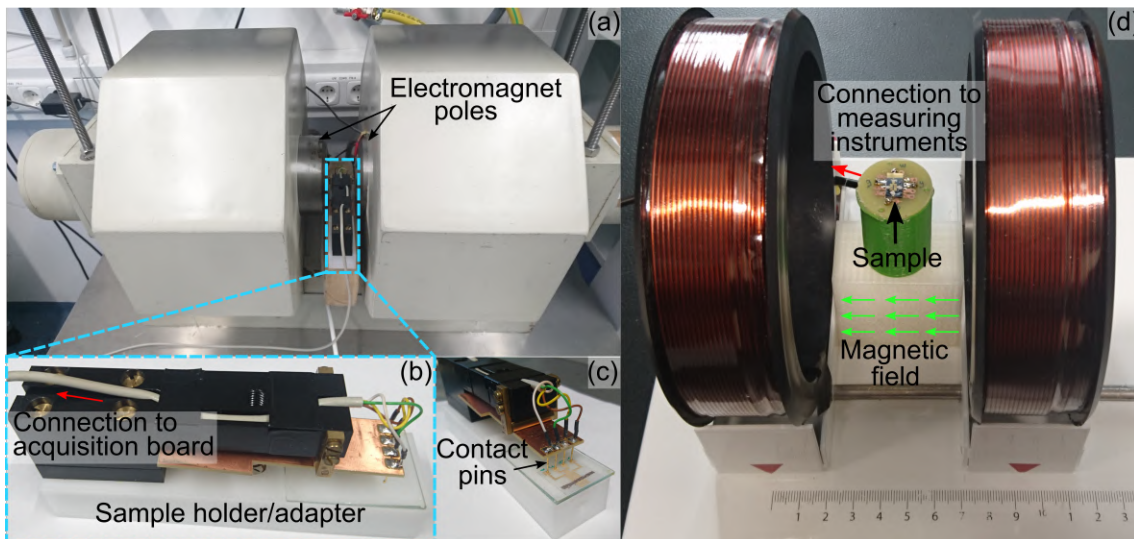


Figure 3.8: **Setups for magnetoresistive characterization.** (a) High field characterization setup (b) Sample holder for adapting and measuring the samples (c) Contact scheme on the sample. Four spring pins allow for four-point probing. (d) Low field characterization setup. The helmholtz coil generates a well-defined and uniform magnetic field all round the volume of the sample.

Low magnetic field strength setup

When characterizing magnetosensitive devices which operate at small fields (< 5 mT), iron core electromagnets have too high remanence and can introduce unwanted offsets while measuring. Hence, we have designed and built a characterization setup based on a Helmholtz coil to measure devices operating in this range (fig 3.8 (d)). The main advantages of this kind of coil are the uniformity, precision and predictability of the field generated. The coil is powered by a B2902A Source Measure Unit (Keysight technologies, USA) and the sample measurements are carried out by

a Keysight 34461A (Keysight technologies, USA) tabletop multimeter. The samples are fixed on a 3D printed plastic holder and contacted with G3303B silver paste (Plano GmbH, Germany) to a cable adapter going to the measuring instruments (fig 3.8 (d)). Prior to all measurements, the magnetic field inside the coils is measured with a HG09 gaussmeter (Goudsmith Magnetic Systems, Netherlands) for different coil currents to derive a calibration curve. The calibration curve provides a reference to determine the strength of the applied magnetic field. In a similar fashion as for the setup above, a LabVIEW program controls the hardware and acquires the measurement data.

3.4.2 Mechanical characterization

Due to the flexible and soft nature of the devices presented in this work, it is critical to understand how the device performance is affected by bending or deformations. In this subsection we present the most prominent tests to address this question.

Static bending tests

In these tests, the samples were measured while being fixed on sample holders with different curvature radii (50 μm – 10 mm in this work). Curvature radii larger than 1 mm were easily achieved with 3D printed plastic holders (Fig. 3.9 (a)) but smaller radii required a custom-made setup based on Si wafer pieces. Two pieces were glued on top of a larger one and a 50 μm diameter enameled copper wire was suspended and fixed between the two support pieces (Fig. 3.9 (b)). The sample to be investigated was then curved around the wire and stuck onto the underlying wafer with double-sided scotch tape. By adjusting the height of the support pieces and the sticking angle on the tape, a variety of very small curvature radii could be achieved. This specific setup was mostly used for SEM imaging as measurements under this configuration are not straightforward. For larger curvature radii, the resistance was acquired as a function of the curvature radius of the sample to determine when and if the device fails due to deformation. In addition, for magnetic sensors the magnetoresistive response was measured at each bending condition.

Cyclic bending tests

In addition to determining the effects of curvature in device performance, it is important to know the endurance of the devices when repeatedly deformed. For this purpose, we have devised an experimental setup for cyclically bending the samples under test. The setup is based on a motorized stage which uses the tray mechanism of a standard optical disk drive, controlled by a NEMA 14 stepper motor (Eckstein, Germany), to precisely bend the samples (Fig. 3.9 (c)). One end of the samples is fixed to the frame of the drive and the other end is attached to the moving tray, so that it cycles back and forth, thereby bending the samples under measurement (Fig. 3.9 (d)). To measure resistance, the samples can be contacted directly with silver paste and copper wires or alternatively with an FFC (Flexible Flat Cable) adapter. The cyclic bending and measurement of the resistance of the samples is done by a custom-made LabVIEW program.

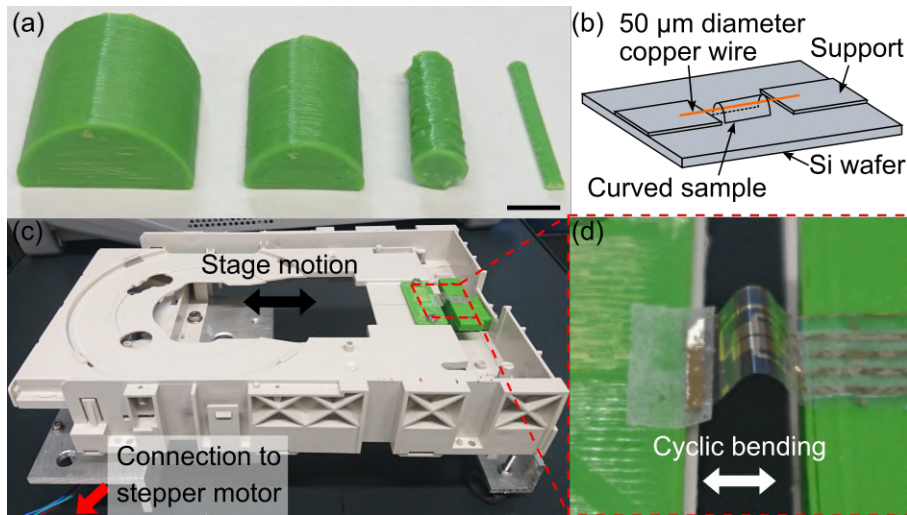


Figure 3.9: **Mechanical characterization tools.** (a) Curved sample holders for static measurements. The scale bar is 3 mm long. (b) Bending setup for sub-mm curvature radii. (c) Motorized cyclic bending stage. The moving tray cycles back and forth to repeatedly bend the sample (area in red). (d) Zoomed image of the sample under bending. Scale bar is 5 mm.

3.4.3 Morphological characterization

Determining the electric response of the fabricated devices can diagnose failure but it does not provide a clear picture of the underlying mechanism which produces it. Hence, it is necessary to image the regions of interest to find out whether breakage, delamination or similar issues have occurred. To do so, morphological information like layer thickness, structure size and shape must be extracted. The methods used to this end in this work are optical microscopy, electron microscopy and focused ion beam cross-sectional cuts.

Optical microscopy

This well-established technique is used to quickly determine the quality of the fabrication during the lithographical process and after the mechanical bending tests. During lithography, it serves as a verification and documentation tool to troubleshoot the process. Later, after the devices are bent or deformed, it can provide information about very notorious cracks or wrinkling which might arise. However, if their morphology and size is hard to distinguish, we analyze the sample in depth with electron microscopy. In this work we have mainly used an Olympus BX51 light microscope for overview characterization of the samples.

Scanning electron microscopy (SEM)

The main advantage of SEM over optical microscopy is that it uses electrons instead of light to image. As electrons have a 4 orders of magnitude smaller de Broglie wavelength than light, their diffraction limit is also smaller, meaning that they can be used to resolve finer structural details. This technique scans a beam of electrons over the sample to create an image by collecting different kinds of electrons which are emitted from the sample. For imaging purposes, the most important ones are

the secondary electrons, which are coming from very close to the sample surface. If the sample is conductive, imaging is relatively straightforward as there will be a path for charge to flow towards ground (usually coupled to the sample holder). However, if the samples are non-conductive, charge build-up occurs at the surface, which severely hinders image acquisition. Therefore, non-conductive samples like the polymer-based devices in this work must be sputter coated with a thin metallic layer (5 nm), typically consisting of chromium (Cr) or carbon (C). The imaging setup used in this thesis is a Zeiss NVision 40 which combines SEM capabilities with a focused ion beam tool for cross-sectional cuts.

Focused ion beam (FIB)

This method utilizes focused beams of ions to probe (low beam currents) or mill (high beam currents) into a sample. The ions typically used for most applications are gallium ions due to their low melting temperature (30°C), low vapor pressure and reasonable wetting of tungsten needles.¹⁹¹ In this thesis, the FIB tool is used for milling purposes to obtain cross-sectional cuts of the fabricated devices. First, the ion beam carves a cavity at the region where the device needs to be studied. Here, the walls of the cavity reveal a cross-sectional cut, which shows a snapshot of how the layers constituting the device are arranged. Then, the imaging plane is corrected to be parallel to the plane of the cut, so that very precise measurements of layer thickness and continuity can be performed. This information is key to determine how the integrity of the devices changes upon bending as it can easily diagnose delamination or rupture of any functional layer.

Chapter 4

Magneto-sensitive e-skins with directional perception

4.1 Introduction

Previous examples of magneto-sensitive e-skins behaved as interactive proximity sensing devices, such as touchless gauges¹⁷ and mapping platforms,¹⁶ based on shapeable magnetoelectronics.¹⁸ However, all these e-skins could not reliably perceive the spatial orientation of incident magnetic fields, an aspect which so far limited their interaction possibilities. Typically, human-computer and human-device interactions rely on buttons and dials which respectively select and regulate variables within the user interface. Buttons can be likened to the point-like functionality offered by previous magneto-sensitive e-skins, yet, to emulate dials it is crucial to harness the directional nature of magnetic fields. Adding this new layer of interaction requires precise and stable access to the angular components of magnetic fields. Though magnetoresistive sensors can detect angular variations by nature, not all of them are suited to work as steady angle sensors. AMR sensors provide small (1 - 3%) MR effects and their angular dependence is square sinusoidal, which limits their angular discrimination to only 180° [112, 192]. Conventional GMR multilayers display a 360° range but their isotropy and lack of a constant resistance operating range does not allow repeatable angle detection. Tunnel magnetoresistance (TMR) devices offer MR effects in the range of 100 - 600%¹⁹³ but upon growing them on flexible polymers, their performance usually decreases.^{194,195} Recent efforts have boosted their performance as flexible sensors,¹⁹³ but they utilize thinned silicon substrates which are not compliant enough for e-skin applications. Furthermore, TMR requires usually non-ductile isolators and a current out of plane fabrication geometry, which complicates their integration in flexible applications. On the other hand, spin-valve sensors combine the ease of integration of GMR systems with a constant resistance operating range, which renders them an ideal option for flexible angle sensors.¹¹² However, to optimally detect the x and y components of an external magnetic field, 8 spin-valve sensors must be combined in two perpendicular Wheatstone bridges.^{112,196} Arranging them in this configuration allows to maximize their signal output and thermal properties. The main challenge arises because of the anisotropic nature of spin-valves, which means that each of them must be placed with a specific magnetization direction. Achieving this feat is especially hard for conventional fabrication as either several material deposition rounds or high precision local annealing would

be required. There have been reports of spin-valve angle sensors fabricated via local laser annealing,¹⁹⁶ yet, this fabrication method is not easily adapted for ultrathin e-skins. In this chapter, we introduce an alternative fabrication method which combines thin film and transfer printing technologies to overcome these manufacturing challenges. The method is applied to assemble 2D angular magnetic sensors and ultimately enable magnetosensitive e-skins with directional perception. These devices operate at low power in conjunction with permanent magnets that do not require energy for operation. Possible upcoming applications range from navigation, motion tracking in robotics, regenerative medicine, sports and gaming to interaction in supplemented reality (Fig. 4.1 (a)). In the latter scenario, the e-skin would monitor body motion of, e.g. a hand when it is rotated with respect to the direction of the external magnetic field (Fig. 4.1 (b) and (c)). Then, the angular position of the hand would be digitized and applied to interact in a touchless way with objects in virtual or augmented reality. Towards the end of this chapter, we demonstrate two application examples of magnetically driven augmented reality systems; a virtual knob for continuous control and a virtual dial pad for discrete encoding.

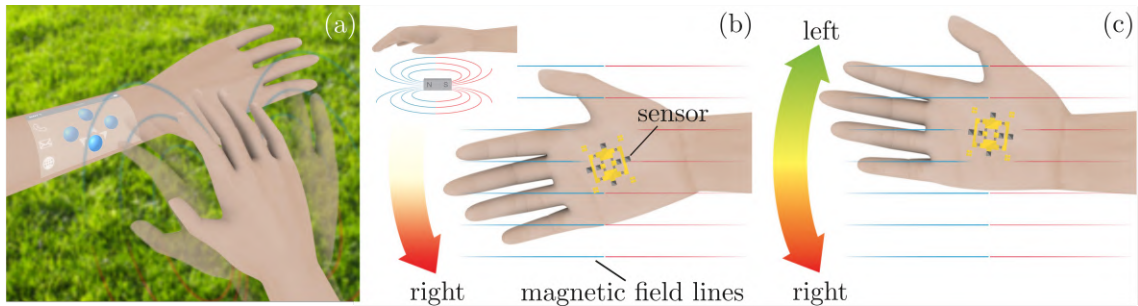


Figure 4.1: **Touchless manipulation of objects based on the interaction with magnetic fields.** (a) Concept of touchless manipulation of an object on a (wearable or virtual) screen by moving a hand. (b) and (c) An on-skin magnetic field sensor is applied to a palm of the hand. Its angular position with respect to the direction of the external magnetic field is monitored and is used to reconstruct the spatial position of the hand. This information can be used to display the position of the hand in a virtual reality scene or/and to enable interaction with objects in virtual or augmented reality. This figure is adapted from.⁴⁰

4.2 Fabrication process

There are many spin-valve configurations which can be used for magnetic field detection, all consisting of antiferromagnetic, pinning, free and spacing layers (chapter 2). In this work we have selected a layer stack which was previously optimized to yield excellent linearity, low hysteresis and high GMR performance.¹⁸¹ The stack comprises a [Py/CoFe]/Cu/[CoFe/Py]/IrMn heterostructure, with IrMn acting as an antiferromagnet pinning the magnetization of the reference [CoFe/Py] bilayer adjacent to it due to exchange bias (EB).¹⁹⁷ The free layer [Py/CoFe] separated by a Cu spacer acts as the sensor layer. These structures are integrated in Wheatstone bridges with orthogonal sensitivity axes to realize entirely flexible 2D magnetic field sensors. The fabrication process was split in two main tasks: sensor chip production

and contact patterning; both sharing the same glass-sacrificial layer-polyimide base stack. To establish the stack, 22 x 22 mm² (VWR International) glasses were left in an aqueous 2 % Alconox (Alconox Inc., USA) detergent solution for 2 h to promote hydrophilicity on their surface. PAA (Polysciences, Inc.) was spin coated on the glasses at 3000 rpm for 30 s, dried at 60°C for 5 min and subsequently crosslinked by rapid dipping in a 2M CaCl₂ solution, to create a sacrificial layer (Fig. 4.2 (a)). In parallel, a polyamic acid solution (precursor for the polyimide foils) was synthesized as described in.^{198,199} In a nutshell: 3,3',4,4'-biphenyltetracarboxylic dianhydride was reacted with 4,4' – Diaminodiphenylmethane in DMAc, modified with dimethylaminoethyl methacrylate and photosensitized using 2% (wt/wt) 2-benzyl-2-(dimethylamino)-4-morpholinobutyrophenone (Sigma-Aldrich LLC). The synthesis occurred by dissolution of 9.93 g of 3,3'-diaminodiphenylsulfone in 20 ml of DMAc with the subsequent addition of 12.8 g of 3,3',4,4'-biphenyltetracarboxylic dianhydride. After mixing for 12 h at 70°C, a solution of polyamic acid in DMAc was obtained. The solution was modified by reaction with 12.5 g of dimethylaminoethyl methacrylate to render the mixture photosensitive. The polyamic acid solution was spin-coated on the sacrificial layer at 3000 rpm for 40 s with a previous acceleration step of 5 s up to 500 rpm. The polymer coated glasses were then heated up at 200°C for 10 min under N₂ to imidize and thereby form a stable polyimide film (Fig. 4.2 (b)). The final film thickness under these conditions was measured to be 1.7 μm by means of profilometry.

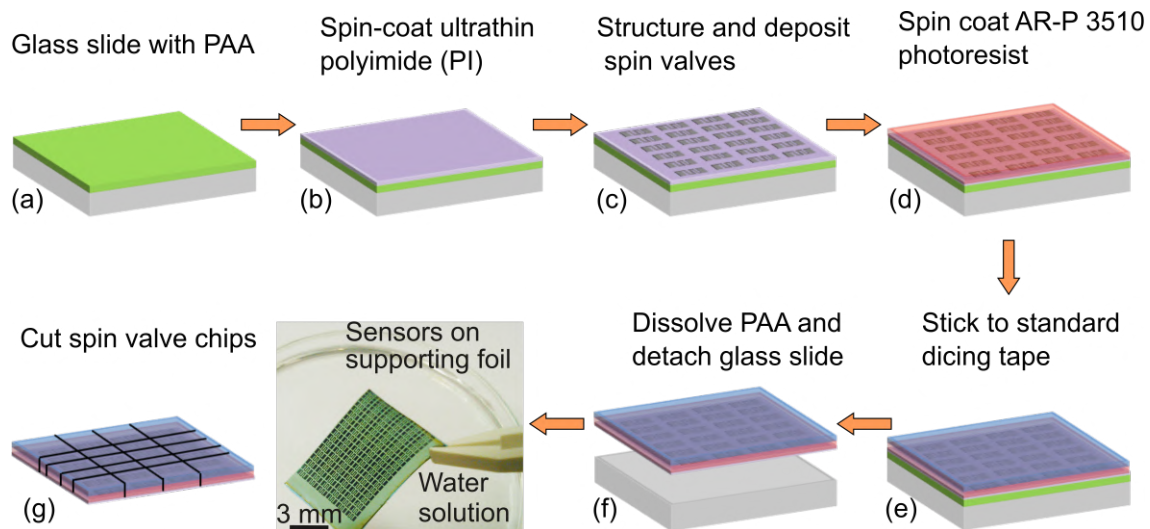


Figure 4.2: **Fabrication of spin-valve sensor chips.**(a) A glass slide is covered with modified polyacrylic acid (PAA) followed by an ultrathin polyimide coating (b). (c) Spin-valve meander sensors are photolithographically patterned over the polyimide and covered with an additional layer of photoresist (d). (e) Standard dicing tape is stuck to the photoresist to serve as transfer support. (f) The PAA sacrificial layer is removed in an aqueous solution of DTPA. (g) The resulting tape hosting the sensor stack is cut in small chips ready to be transferred. This figure is adapted from.⁴⁰

On top of the resulting film, meander sensor chips consisting of a magnetron sputter deposited multilayer spin-valve stack of [Ta(5 nm) / Py(4 nm) / CoFe(1 nm) / Cu(2.4 nm) / CoFe(1 nm) / Py(4 nm) / IrMn(8 nm) / Ta(2 nm)] (base pressure:

$3 \cdot 10^{-7}$ mbar; Ar sputter pressure: $7.5 \cdot 10^{-3}$ mbar; deposition rate: 1 - 2 Å/s depending on the material (36)) were patterned by photolithography (Fig. 4.2 (c)). The spin-valve meanders were prepared an extended array in a single deposition run (17 x 6 sensing devices; total: 102 spin-valves) to facilitate the fabrication and ensure device uniformity. Two permanent magnets were mounted on the sample holder to define the exchange bias direction of the sensors. The resulting spin-valve arrays were covered with AR-P 3510 photoresist by spin coating (3000 rpm for 35 s following by 5 min drying at 50°C) (Fig. 4.2 (d)). Next, standard blue dicing tape was laminated on the stack to aid as a support during further steps of the transfer process (Fig. 4.2 (e)). The final stack was left in an aqueous solution of DTPA until the PAA was fully dissolved and the remaining part of the stack released from the glass (Fig. 4.2 (f)). The free standing tape containing the sensors was blade cut into single spin-valve sensor chips (Fig. 4.2 (g)) which were then transferred to another foil hosting the patterned contacts. The contacts were manufactured on another set of glasses accommodating the same base stack described before. Conventional lift-off photolithography (AR-P 3510 photoresist, 3500 rpm, 35 s) was performed to pattern [Ta(5 nm) / Au(100 nm)] contacts on top of the base stack (Fig. 4.3 (a)). Contact deposition was carried out by magnetron sputtering at room temperature (base pressure: $5 \cdot 10^{-7}$ mbar; Ar sputter pressure: $1 \cdot 10^{-3}$ mbar; deposition rate: 0.41 Å/s for Ta and 1.5 Å/s for Au). The contacts were designed with 8 empty regions to later fit the single spin-valve chips in between the different branches of the bridge.

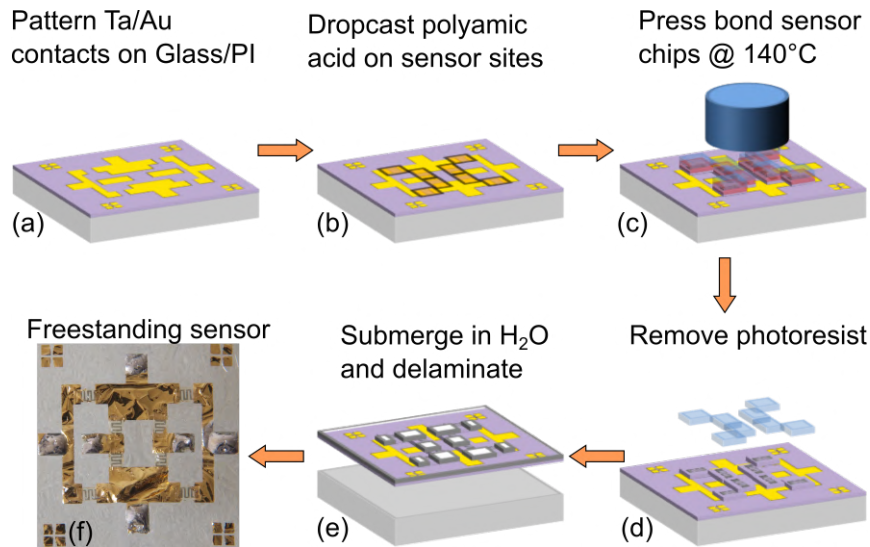


Figure 4.3: **Assembly of a 2D magnetosensitive e-skin.**(a) Standard lithography is used to pattern the contacts and main structure of the e-skin. (b) Polyamic acid droplets are dropcasted on the corresponding transfer spots of the chips. (c) The chips are placed on the droplets and press bonded at 140°C using a weight. (d) After the chips are secured in place, the photoresist is removed in acetone to expose the meander sensors. (e) The meanders are electrically contacted to the underlying layout from (a) and encapsulated with PDMS. Subsequent immersion in water or a saline solution detaches the stack from the glass to yield a freestanding magnetosensitive e-skin (f). This figure is adapted from. ⁴⁰

The transfer of the spin-valve chips to the contacts was done by drop casting liquid

polyamic acid on each of the predetermined spots for the sensors (Fig. 4.3 (b)). Then, the sensors were carefully placed on the droplets and aligned to fit their corresponding magnetization and position within the Wheatstone bridge design. Afterwards, the contacts plus sensor were placed in between two flat glasses and pressed with a 500 g weight for 5 min at 50°C to evaporate the solvent from the liquid polymer. Following this pre-heating, the samples were further pressed in the same way but at 140°C for 10 min to imidize the bonding polymer droplets (Fig. 4.3 (c)). The resulting sensor was let to cool down and then placed in acetone for 2 min to remove the photoresist and delaminate the dicing tape, leaving a fully bonded sensor (Fig. 4.3 (d)). After bonding, the spin-valves were electrically contacted with G3303B silver paste (Plano GmbH, Germany) to the underlying contacts. The output regions of the contacts were subsequently covered with dicing tape and a 5- μm -thick encapsulation layer of PDMS was spin coated on top (6000 rpm, 5 min). Finally, the finished sensor was let dry for 24 h at room temperature to cure PDMS and complete the elaboration process. A final immersion of the device in aqueous solution of DTPA allows it to be released from the rigid glass support (Fig. 4.3 (e)) To achieve its freestanding state (Fig. 4.3 (f) and 4.4 (a)).

4.3 Mechanical characterization and performance

After release, the high mechanical compliance of these slim sensors allows them to intimately conform to curvature radii below 1 mm. Examples of this remarkable behavior can be seen in figures 4.4 (b) and (c), where they seamlessly attach to a human hair (50 μm curvature diameter) and a doctor blade (10 μm curvature diameter), respectively. This extreme performance is mediated by the ultrathin nature of their design. Even these extreme bending trials do not impair the GMR performance of our sensors and no signs of degradation of the metal films, e.g. cracks or layer stack delamination, are observed. This remarkable mechanical performance enables the sensor to be readily applied as on-skin electronics with magnetic functionality (Fig. 4.4 (d) and (e)). An SEM investigation of the sample cross-section (prepared via FIB etching through the layer stack) reveals that the metal layer is firmly attached to the polymer and follows the surface morphology (Fig. 4.4 (f)).

We note that for the FIB/SEM characterization the samples are capped with a 5 nm thick Cr layer to avoid charging. There are no cracks in the spin-valve or delaminated regions observed when investigated at different locations of the sample. We note that bonding of the sensor chips on 1.7- μm -thick foil to the extended 1.7- μm -thick supporting foil results in a perfectly homogeneous polymeric layer with a total thickness of about 3.5 μm at the sensor location. There is no boundary between the two foils visible in the SEM image, which is crucial to assure mechanical integrity of the entirely flexible device. Repeatedly bending the spin-valve sensors during on-skin operation does not hinder their performance during magnetoresistive measurements on the middle joint of a finger (Fig 4.5). This plot depicts to the time evolution of the resistance recorded during our experiments. In the absence of an external magnetic field, a repeated movement of the finger does not alter the sensor response (Fig. 4.5 (a)). Signal change is observed only when the functional element is exposed to a magnetic field, e.g. of a permanent magnet. When the magnet is aligned with the low sensitivity of the device the resistance is variation prone and

the sensitivity is limited (Fig. 4.5 (b)). By contrast, approaching the sensor from the high sensitivity axis yields a stable signal with high sensitivity and a GMR effect of about 4% (Fig. 4.5 (c)).

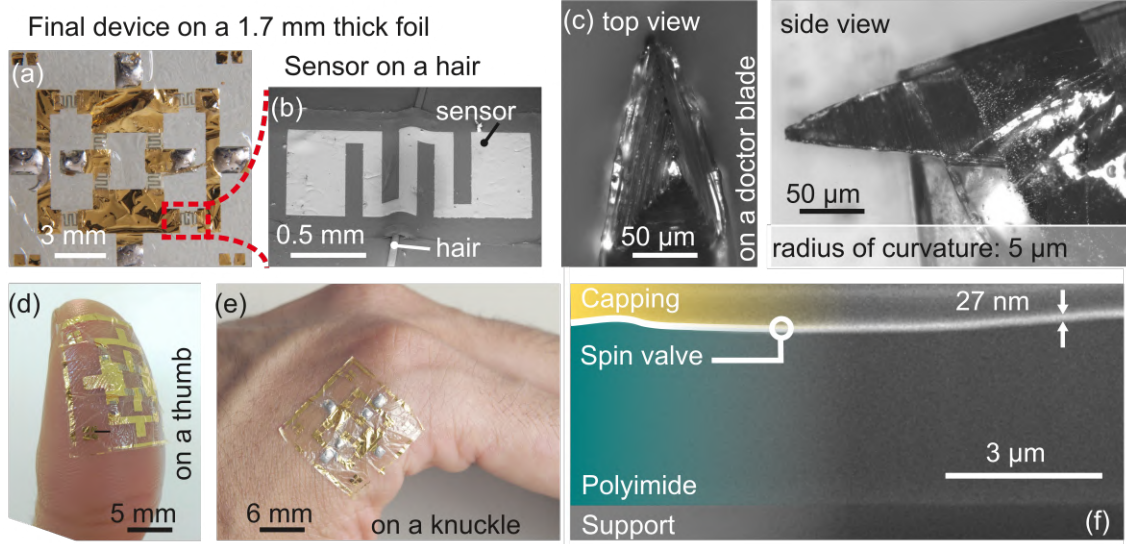


Figure 4.4: **Compliance characterization of the 2D magnetosensitive e-skin.** (a) Optical microscopy image of a 2D sensor containing two Wheatstone bridges accommodating in total 8x spin-valves properly arranged with respect to their exchange bias direction. An individual spin-valve element can compliantly cover a hair (diameter: 50 μm) or a doctor blade (diameter: 10 μm) as shown in panels (b) and (c), respectively. (d and e) Photographs of the entire 2D sensor conveniently placed on skin. (f) An SEM image of the sample cross-section reveals the complete layer stack consisting of a novel polyimide foil covered with a firmly attached 27 nm thick sensing layer, which follows the surface morphology. The total thickness of the polymer is about 3.5 μm , including two bonded 1.7- μm -thick foils. The resulting polymeric layer is perfectly homogeneous, and the bonding plane cannot be resolved. This figure is adapted from.⁴⁰

To analyze the stability of the devices upon bending and the adhesion properties of the metal films to the polymeric support we carried out several cuts using FIB at different locations over the sample. No signs of delamination of the metal layer from the polymer were found. Furthermore, we studied the mechanical integrity of our devices upon bending into radii below 100 μm . To achieve these small bending radii, we laminated our flexible devices onto a pre-stretched very high bonding (VHB) elastomer, inducing wrinkling of the sensor upon strain relaxation of the elastomer. In this way, we achieved sub-10 μm bending radii. The wrinkled structures were studied using SEM following FIB cutting of the samples. Even when bending down to radii of about 30 μm , the film remained intact (Fig. 4.6(a)-(c)). If the radius of curvature reaches below 10 μm , we could occasionally identify cracks in the film (Fig. 4.6(d) and (e)). These noteworthy results are attributed to the enhanced mechanical performance arising from the reduced thickness of the substrate.

By using an ultrathin (1.7- μm -thick) substrate, the strain in the metallic spin-valve film is greatly reduced. This directly follows from analytical mechanical consid-

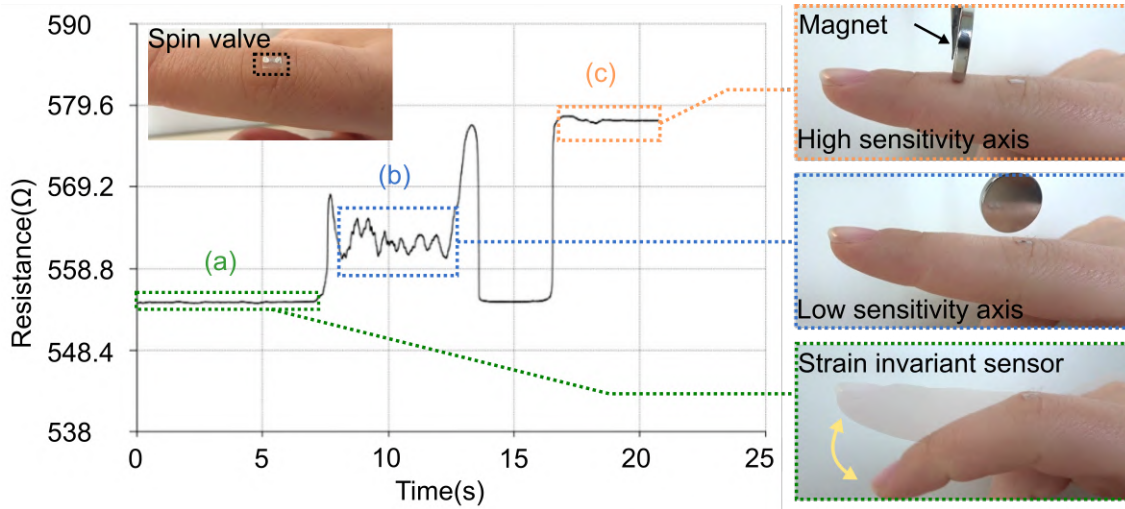


Figure 4.5: **Functional tests of a single spin-valve sensor under mechanical strain.** A spin-valve sensor is affixed to a finger joint (inset) to monitor its response upon on-skin bending. (a) Even upon continuous strain, the resistance of the sensor remains stable. (b) When a permanent magnet is brought near the sensor, its resistance changes almost 2% when approached from the low sensitivity axis of the sensor. The fluctuations observed correspond to the motion of the permanent magnet near the sensor. (c) When the sensor is approached from the high sensitivity axis, the resistance change reaches the expected maximum of 4% with a stable signal.

erations for foldable film-on-foil electronics.⁶⁷ Here, the strain ϵ_{top} in a rigid film (Young's modulus: Y_f , thickness d_f) on a softer substrate (Young's modulus: Y_s , thickness d_s) is computed when bending down to a radius R via 2.3 in chapter 2.

For the polyimide foil in this work, the corresponding parameters are $Y_s = 3$ GPa and $d_s = 3400$ nm (two bonded polyimide layers with each layer being 1700 nm thick). Furthermore, we derived the elastic module of the spin-valve layer (total thickness: $d_f = 27.4$ nm) by its material composition to be 167 GPa (7 nm thick Ta: $Y_{Ta} = 186$ GPa, 8 nm thick Py: $Y_{Py} = 120$ GPa, 2 nm thick CoFe: $Y_{Co} = 209$ GPa, 2.4 nm thick Cu: $Y_{Cu} = 130$ GPa; 8 nm thick IrMn: $Y_{Mn} = 209$ GPa). Using the model by⁶⁷ and considering that the film withstands bending to radii of at least 30 μm , we estimate the strain in the layer to be at maximum 4%. This rough estimate is already near the fracture strain even for Cu. Other relaxation mechanisms, e.g. reducing the film area due to patterning and edge roughness are considered to further reduce the strain in the metal film. We note that increasing the thickness of the polyimide substrate to that of a thin commercial foil (25 μm) will increase the resulting strain up to 40%, values that would result in cracking of the metallic film. These estimations further corroborate the importance of reducing the substrate thickness to improve the overall mechanical performance of the sensors.

Practical applications in wearables will benefit from laminating our ultrathin sensor foils to thin sheets of soft elastomers as strain-buffering interfaces to i.e. the human skin. As detailed below, an approximately 75- μm -thick PDMS sheet would be sufficient to place the spin-valve sensors into the neutral mechanical plane b, greatly reducing the bending-induced strain on the metallic layers. The calculations are based on a model presented by Jeong:²⁰⁰

$$b = \frac{\sum_{i=1}^N \bar{Y}_i d_i (\sum_{j=1}^i d_j - \frac{d_i}{2})}{\sum_{i=1}^N \bar{Y}_i d_i} \quad \text{with} \quad \bar{Y}_i = \frac{Y_i}{1 - \nu_i^2} \quad (4.1)$$

Where Y_i , d_i and ν_i are the Young's modulus, thickness and Poisson's ratio of the layer i in the stack of layers forming the sensor. b is the height from the bottom of the stack, at which the mechanical neutral plane is found in a multilayer system.

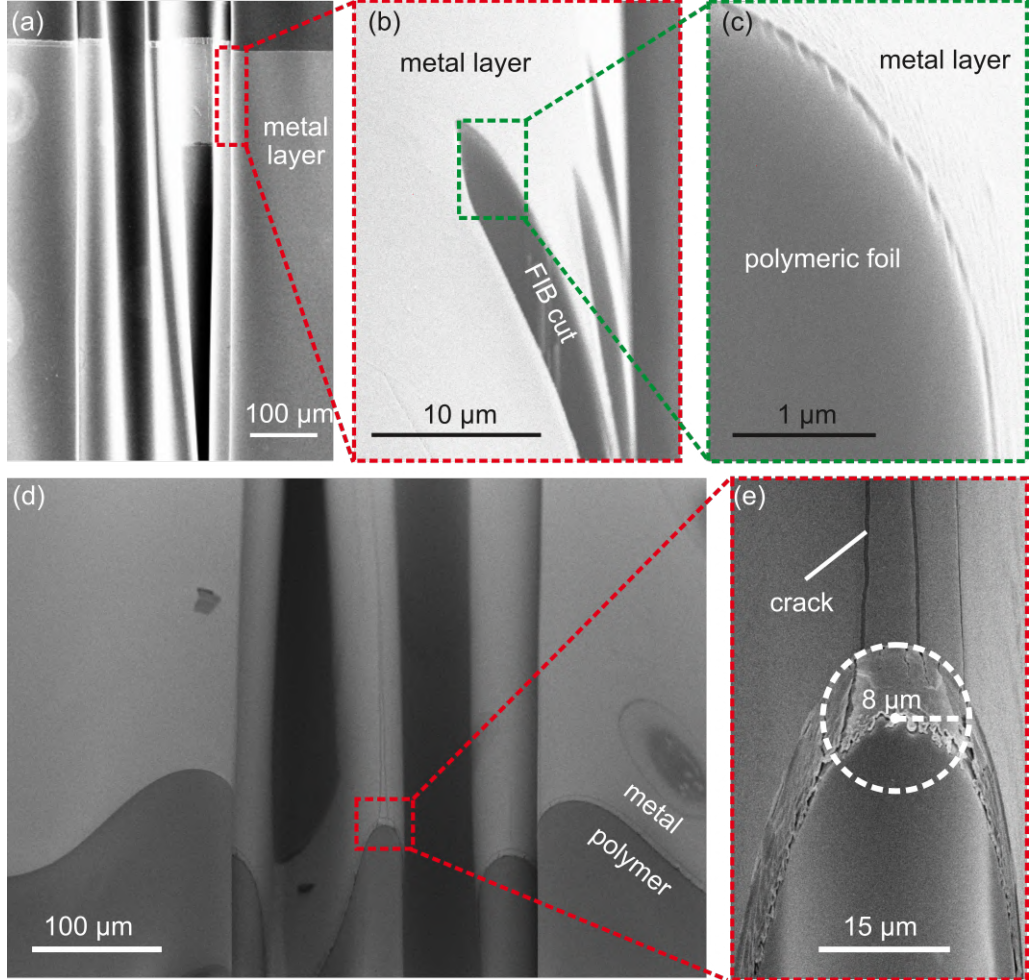


Figure 4.6: **Mechanical stability of the sensor layer stack upon bending.** (a) SEM top view image of a wrinkled spin-valve sensor. The red frame shows the location of a FIB-cut region. The close-up of this region is shown in (b). The zoom of the region indicated with a green frame in panel (c) is shown in (c). (d) SEM top view image of a wrinkled spin-valve sensor. The close-up of the region indicated with a red frame in (d) is shown in (e). Bending radii below $10 \mu\text{m}$ occasionally induce cracking of the metal layers. This figure is adapted from.⁴⁰

The PI film and the spin-valve were considered as a single layer with a weighed equivalent Young's modulus $Y_1 = 4.31 \text{ GPa}$ and Poisson's ratio $\nu_1 = 0.34$. PDMS as the soft layer has $Y_2 = 1.84 \text{ MPa}$ and $\nu_2 = 0.5$. With these parameters, the mechanical neutral plane b is located at about $1.7 \mu\text{m}$ from the bottom of the stack, right where the spin-valve lies. For non-ideal situations where the spin-valve is a distance δ from the neutral plane, we would arrive at a strain of $\epsilon = \frac{\delta}{R}$ with R being the curvature radius. We note that placing the sensor foil on pre-stretched VHB

tape to form a wrinkled structure (and thus a stretchable sensor) will likewise move the active spin-valve close to the neutral plane, as the VHB elastomer used in these experiments has a similar Young's modulus and a thickness in the range of 50 - 100 μm .

Another strategy to improve the strain tolerance of our sensors is to use a 1.7- μm -thick polyimide layer as encapsulation, as the now matching Young's moduli of the substrate and encapsulation will place the spin-valve again in the neutral mechanical plane and thus allow extreme flexibility without damage to the sensor layer.

4.4 Magnetoresistive performance

To gauge whether these 2D sensors remain stable even upon bending, they were tested by placing them onto adapters with pre-defined curvature radii. Individual GMR sensor elements were characterized at room temperature by locating them between the pole shoes of an electromagnet. The magnetic field is applied in the sensor plane along the exchange bias direction and the change of the electrical resistance is measured as a function of the applied magnetic field. The GMR ratio is defined as the magnetic field dependent change of the sample's resistance, $R(H_{ext})$, normalized to the resistance value of the magnetically saturated sample, R_{sat} : $GMR(H_{ext}) = [R(H_{ext}) - R_{sat}]/R_{sat}$. All of the manufactured spin-valves sensor chips displayed the same exchange bias direction and revealed a GMR effect with a magnitude of about 4% (Fig. 4.7 (a)). Bending down to a curvature of 1 mm did not change the response of the sensing layer and the overall GMR performance of the sensor (Fig. 4.7 (a)). Their operating range as angle sensors corresponds to the plateau between 20 and 120 Oe, where the spin-valves present an almost flat response (no variation of the resistance) as a function of the magnetic field. This condition renders our devices ideal for angle sensing, as the only parameter determining the resistance in this magnetic field range is the angle of the incident field.

To gain access to this external field, the 2D sensors rely on a nested configuration to connect two Wheatstone bridges.^{112,196} Each of the bridges includes four spin-valve sensors which are oppositely biased with respect to their adjacent neighbors (Fig. 4.7 (b)). This placement of the spin-valve sensor elements allows us to achieve a bipolar output where the full signal amplitude is that of a single element. In addition, due to the Wheatstone configuration, the temperature dependence of a single flexible sensor is canceled out and their intrinsic output offset is removed.^{186,201} The inner bridge outputs a voltage V_{cos} proportional to the cosine of the angle θ between the bridge magnetization axis and the orientation of the external magnetic field (inset in Fig. 4.7 (b)). Analogously, the outer bridge produces a voltage V_{sin} proportional to the sine of θ . With these two output signals the angle θ is readily determined via $\theta = \tan^{-1} \frac{V_{sin}}{V_{cos}}$.

Next, we validated the angle reconstruction capabilities of our devices with irregular external magnetic fields that would typically occur in realistic settings of a wearable gadget. To this end, we studied the sensor response to discrete angular steps to verify the correspondence of the measured angles with the software calculated ones. For this experiment the sensor was fixed to the center of the sample holder and a permanent magnet was placed at different angles along the perimeter of the holder.

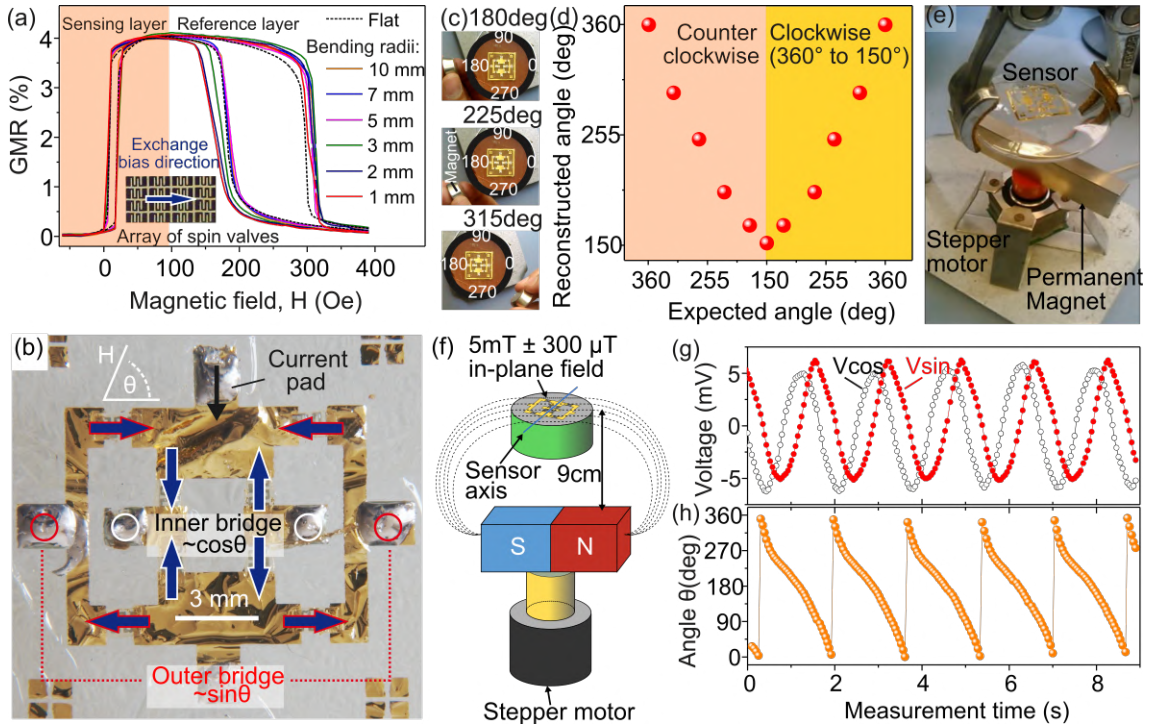


Figure 4.7: **Magneto-resistive characterization of spin-valves and angle reconstruction.** (a) GMR performance of an individual spin-valve sensor. The magnetic field is applied along the exchange bias direction. The sensor response (properties of the sensing layer, orange shaded region) does not change when the sensor is bent down to a radius of curvature of 1 mm. An array of spin-valve sensors prepared on thermally stable polyimide-based ultrathin foils is shown as an inset. The exchange bias direction is set in the same direction for all the sensors in the array. (b) Individual spin-valve sensors are arranged with respect to their EB direction in two Wheatstone bridges, each containing four spin-valve sensors to constitute a 2D magnetic field sensor. The response of the inner/outer Wheatstone bridge (indicated in white/red) is proportional to the cosine/sine of the angle θ between the bridge magnetization axis and the orientation of the external magnetic field, H . (c) Snapshots of the angular reconstruction experiment. A permanent magnet is moved along the perimeter of the sample holder to provide angular input. The most important reference angles are included as reference labels (0° , 90° , 180° , 270°). The three magnetic orientations of the frames (180° , 225° and 315°) are subsequently reconstructed. (d) Reconstruction of the magnetic field angle. The most relevant angles are shown as red spheres in the plot, which correspond to specific snapshots during the experiment. (e) A permanent bar magnet is attached to the shaft of a stepper motor to provide a constant field in the plane of the 2D sensor. The sensor is fixed on a curved glass support suspended over the magnet such that the in-plane field magnitude is 5 mT (50 Oe), which happens at about 9 cm spacing (f). (g) Characterization of the 2D sensor. Voltage output signals of the inner (V_{\cos}) and outer (V_{\sin}) Wheatstone bridges of the 2D sensor. The period of the signals closely corresponds to the rotational speed set by the software (1.6 revolutions/s). There is a phase shift of 90° between the inner and outer bridge signals, which allows the reconstruction of the angle of the magnetic field (h). This figure is adapted from. ⁴⁰

The magnet was rotated around the sample while keeping a distance of about 2.5 cm to the sample’s center in order to provide a field of 50 Oe at each angle (Fig. 4.7 (c)). The selected angles were spaced 45° from each other starting at 0° and going in a clockwise direction up to 180°; the last step was measured at 150°. All of the procedure was simultaneously captured on video. Then, the video was analyzed to extract the angular placement of the magnet. This angle was plotted against the measured angle to determine their resemblance. The data from these measurements revealed good correspondence between the reconstructed and the measured angles (Fig. 4.7 (d)).

To quantify the dynamic response of the sensor, we devised a motorized setup consisting of a rotating permanent magnet placed underneath a disk-like sample holder. The magnet was fixed to the shaft of a stepper motor (Trinamic PD3-110-42) in such a way that the uniform field lines lay parallel to the plane of the sample, therefore allowing a controlled rotation of the in-plane field (Fig. 4.7 (e)). Furthermore, the sample holder was fixed 9 cm over the magnet with an extension clamp to ensure a constant field of 50 Oe (Fig. 4.7 (f)), as measured with a HG09 gaussmeter (Goudsmith Magnetic Systems, Netherlands). We note that this field falls inside the ideal operation region of our spin-valves (20 – 120 Oe). When conducting this experiment, we made sure that the characterization setup used to measure the sensor was designed such that the in-plane field had a variation of less than 300 μ T within the area of the sensor (Fig. 4.7 (f)). This arrangement was achieved by first determining the best geometry and placement for the magnet to generate a constant field over a large enough area to cover the entirety of the sensor. We verified that the magnetic field within the sensor plane varies only minimally (less than 300 μ T) using a gaussmeter.

The sensor was then placed on the holder and connected to two B2902A Source and Measure Units (Keysight Technologies, USA). One of the units was used to source a constant voltage of 1 V to bias the sensor and the other one was used to measure the outputs of each of the two nested bridges. The second unit was remotely programmed and controlled with custom software to acquire the output voltages of the sensor, compute the corresponding angle value and visualize the results on screen. The stepper motor’s software (TMCL-IDE v. 3.0.10.0) drove the motor at a constant rotational speed of 1.6 revolutions per second during the experiments to facilitate data analysis. We measured a sinusoidal response from each of the bridges with an expected 90° phase shift between outputs (Fig. 4.7 (g)) and a corresponding real-time reconstruction of the magnetic field angle (Fig. 4.7 (h)). The acquired voltage signals were fit to a sine function to determine how much they resembled the ideal case. We found that for a standard fitting function of the form $y = y_0 + A \sin[\pi \frac{(x-x_c)}{w}]$ (A - Amplitude of the peak and w - peak width) the standard error was 0 for all parameters but w , for which the error was only $4 \cdot 10^{-4}$. These results were obtained both in the pre- as well as post-transfer states.

4.5 Application examples

4.5.1 Virtual keypad

We devised a demonstrator where the magnetosensitive e-skin is mounted on an elastic wristband to create a device capable of transducing local magnetic fields into

discrete values. A permanent magnet providing magnetic input is attached to the index finger of a volunteer, who then places his finger above distinct angular positions of the e-skin. The local in plane magnetic field changes at these locations and the e-skin converts the magnet positions into pre-defined characters, thereby turning the wristband into a virtual keypad which is addressed in a touchless manner. We encode the characters “+”, “9”, “4” and “1” to the angular segments around 270° , 180° , 90° and 0° , respectively (Fig. 4.8 (a)). Approaching the wristband with the finger at given angles allows to type a predefined sequence of symbols, e.g. the initial part of a phone number +4914... as an example (Fig. 4.8 (b)).

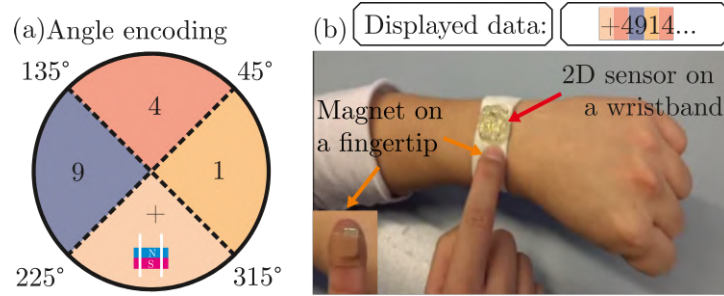


Figure 4.8: **Virtual keypad addressed in a touchless manner.**(a) Characters “+”, “9”, “4” and “1” are encoded in angular segments around 270° , 180° , 90° and 0° , respectively. (b) Photograph showing a 2D sensor mounted on an elastic wristband resembling a virtual keypad. The encoded symbols are displayed when a corresponding angular segment of a sensor is exposed to a magnetic field of a small permanent magnet at the fingertip. This figure is adapted from. ⁴⁰

4.5.2 Interactive light dimming by touchless manipulation

The on-skin directional sensors allow controlling a physical property of an object in virtual reality relying on the interaction with magnetic fields exclusively. We develop a demonstrator based on a magnetic source made of a plastic ring-like support with a permanent magnet in the middle. One of our angle sensors is fixed to the palm of a hand and connected with a computer for visualization purposes (Fig. 4.9 (a)). The software encodes the angles received into 7 luminescence regions. Each of the regions corresponds to a particular light intensity translating into control of an on-screen virtual light source. The visual representation also includes a virtual dial corresponding to the current position of the hand on the physical magnetic dial. Here, angles between 0 and 180° are encoded to replicate the typical movement of a hand when operating a real dial. In the absence of an incident magnetic field on the sensor the dial does not react and there’s no dimming response (Fig. 4.9 (a)). When the hand is placed over the magnetic dial at a suitable distance range, the virtual dial displays a signal proportional to the angle between sensor and magnetic field axes (Fig. 4.9 (b) and Fig. 4.1). As the encoding is limited to 180° , when the user reaches the limit value, the virtual dial and light bulb show maximum intensity (Fig. 4.9 (c)). This methodology allows us to realize a light dimming application of a virtual bulb, manipulated solely upon rotation of a volunteer’s hand above a magnetic source.

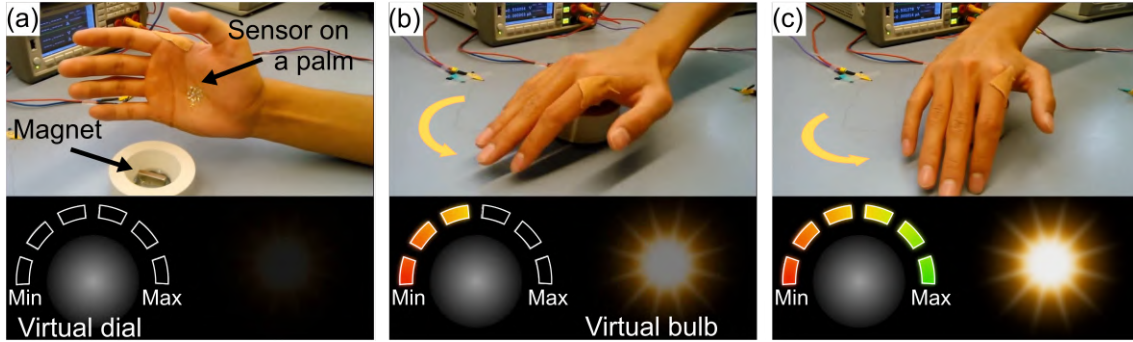


Figure 4.9: **Light dimming of a virtual bulb.**(a) Skin-applied 2D sensor as on-skin electronics with directional perception. (b and c) Movie snapshots demonstrating touchless manipulation of a virtual object using our on-skin 2D magnetic field sensor. The hand is turned with respect to the direction of the magnetic field lines of a permanent magnet. This motion of the hand is monitored and the angular position is transformed into the setting of a virtual dial, in turn controlling the light intensity of a virtual bulb. This figure is adapted from. ⁴⁰

4.6 Reliability tests

On-skin electronics must withstand specific operating conditions which could damage some of its functional components. Therefore, besides from the mechanical stability which has been shown so far, the influence of additional parameters like humidity, geometrical constraints and temperature is studied in this section.

4.6.1 Encapsulation performance

Usual applications of on-skin electronics involve continuous monitoring of variables in the presence of body fluids which can potentially disrupt proper operation. The most common of these fluids is sweat, which not only contains water but is also ionic in nature. To test how such an environment would affect our spin-valve sensors, we prepared a PDMS encapsulated version of a single spin-valve on a flexible PCB. Next, we recorded the resistance of the sensor before and during immersion in water and salt solutions with a table top multimeter (Keysight 34461A). We found the initial resistance value to be 565.125Ω (Fig 4.10 (a)), which increased only about 0.2 % upon immersion in a deionized water solution (Fig 4.10 (b)). Further immersion in a sweat-like saline solution with a concentration of 40 mmol/L of sodium chloride showed a negligible increase of 0.02 %, showcasing a remarkable stability (Fig 4.10 (c)). Long-term stability studies have shown so far that even after 30 seconds immersion no significant change is observed; however, further tests must be run to confirm this trend. These initial results make us confident that our sensor platform is a viable solution for wearable magnetic field-based interfaces.

4.6.2 Angular resolution

A crucial parameter for analyzing the data acquired by the ultrathin sensors presented above is their angular resolution. In our experiments, we estimated it using the intrinsic noise of the sensor and the total voltage range over 180° . We observed a measurement noise of $200 \mu\text{V}_{pp}$ (after software filtering), which together with a

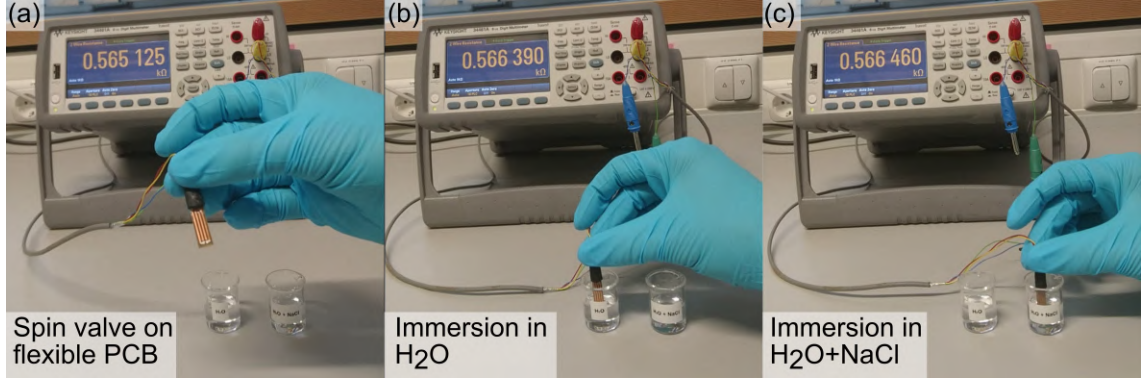


Figure 4.10: **Encapsulation experiments for a spin-valve sensor.** Upon submerging a spin-valve sensor on a flexible PCB (a) in DI water (b) and sweat-like saline solution of 40 mmol/L (c) the resistance of the device changes only slightly. This figure is adapted from. ⁴⁰

detection range of $180^\circ / 5 \text{ mV}_{pp}$ yielded an effective resolution of about 7° . These calculations would allow in principle to encode more angles, however, there are additional factors to be taken into account. These are: (i) the output voltage offset, (ii) the transition regions between encoded values, and (iii) the size and shape of the source magnet used to actuate the sensor.

(i) The output voltage offset is crucial as the angle is reconstructed from:

$$\theta_{rec} = \tan^{-1}\left(\frac{V_{sin}}{V_{cos}}\right) \quad (4.2)$$

Under ideal circumstances V_{sin} and V_{cos} have the form $A\sin(\theta)$ and $A\cos(\theta)$, with A being the signal amplitude. However, upon the introduction of an offset they become $A\sin(\theta) + V_{sin,off}$ and $A\cos(\theta) + V_{cos,off}$, resulting in a less trivial reconstruction:

$$\theta_{rec} = \tan^{-1}\left(\frac{A\sin(\theta) + V_{sin,off}}{A\cos(\theta) + V_{cos,off}}\right) \quad (4.3)$$

Therefore, it is crucial to include offset compensation. We used a software-based compensation scheme that updates itself at every run to cancel out the V_{sin} and V_{cos} offsets.

(ii) The transition regions are required to leave enough spacing between the encoded values and avoid cross-talking between two adjacent values. Angles falling inside these regions are not encoded and thus serve as separators. If we determine the transition regions of being 2 times the angular resolution ($= 14^\circ$), we can calculate a theoretical maximum for the number of encoded values by assuming the case when the span of the transition region equals that of the encoding region. In this case, the total number of sectors is given by $360^\circ / 14^\circ = 25$ and as half of them are used as transition regions, we arrive at a maximum of 12 values that can be reliably encoded.

(iii) The size of the magnetic flux area and the uniformity of the magnetic source (permanent magnet attached to the finger in Fig. 4.8 (b)) are additional aspects to be considered. If the area of influence of the source is larger than the physical area spanned by a particular encoded value, crosstalk will occur even if the sensor performs as desired. Also, if the magnet is too small (comparable to a single spin-

valve), it will not be able to activate all spin-valves simultaneously and the reading will be inaccurate. We therefore used a magnet size that allows an efficient reading for 90° spacing. However, reducing the size of the magnetic flux area is possible (here by about 4 times), allowing encoding of up to 8 values. Further expansion of the values is feasible and will require additional optimization of the encoding and the magnetic source.

4.6.3 Temperature stability

Due to the operating requirements of these e-skins sensors, their substrate and functional layers must withstand temperatures of up to 200°C and tolerate possible fluctuations. Therefore, special attention was paid to the design of robust materials and temperature compensation schemes.

Robust polymeric support

We developed temperature stable polyimide-based foils to comply with the need of temperature treatment of the sensor while processing. Being only 1.7- μm -thick, these foils assured mechanical imperceptibility and highest possible conformability of the devices as needed for on-skin appliances. Despite their thinness, the foils can withstand long-term annealing at 300°C even when exposed to a constant stress and allow soldering to contact pads that are lithographically defined on a foil. Furthermore, they possess a very small surface roughness of about 1 nm (Fig. 4.11 (a)), which is essential for the successful growth of high-performance magnetic sensor layers. The foils offer good adhesion for functional elements processed on it using standard deposition and lithography techniques (see, e.g. Fig.4.3. The synthesized polymeric foil reveals remarkable thermal stability even allowing for regular soldering to be performed. In the following we characterize the thermal stability of the polymeric support and compare it to the commercially available counterparts. For this study we devised a strain-temperature experiment at constant stress. In order to have well characterized references, we used standard high performance polymer films like 100- μm -thick polyethylene terephthalate (PET), 100- μm -thick polyetheretherketone (PEEK) and 2.5- μm -thick Dupont’s Mylar (Table 4.1). In this experiment, the films were vertically fixed with a spring clip to a clamp stand and pulled downwards by another 10 g spring clip which provided constant stress during the measurements (inset in Fig. 4.11 (b)). Then, the films were heated up progressively with a ZD-939L hot air rework station (Ningbo Zhongdi Industry & Trade Co.) until reaching their breaking point. The heat was supplied through a 4 mm diameter nozzle for ultrathin foils (2.5- μm -thick Mylar and the polymeric foil synthesized in this work) and without a nozzle (2.1 mm heating diameter) for 100- μm -thick samples. The reason for this heating area modification was to assure that the thinnest samples remained perpendicular to the temperature source without being pushed away by an excessive airflow. Next, the behavior of the films was captured on video to determine their deformation upon heating. The quantitative deformation analysis was done by comparing the length L of the films at each of the frames of the video with their original length L_0 . Using this information, we calculated the elongation as $\frac{(L-L_0)}{L_0}$ as a function of temperature for each of the investigated polymer films. By plotting the elongation as a function of the temperature, we observed that our polyimide foils can withstand temperatures up to 344°C, when it finally breaks. This

performance is quite remarkable given that its cross sectional area is two orders of magnitude smaller than that of the other evaluated polymers except for Mylar. Thicker polymers like PET and PEEK could not reach more than 150°C without breaking and also Mylar, the ultrathin version of PET, could not withstand beyond this temperature. Considering the small thickness of the foil, loading it with 10 g corresponds to a surface pressure of 58 kPam. In addition to this rather high pressure, the foil withstands temperatures of up to 340°C (Fig. 4.11 (b)) by far outperforming commercially available PET foils. This remarkable thermal stability of a 1.7- μm -thick foil allows for a regular soldering of electrical contacts directly to the lithographically defined contact pads (Fig. 4.11 (c) and (d)). An SEM image of the sample cross-section reveals that the contact pad is firmly attached to the polymer even when in the direct vicinity to the soldered contact (Fig. 4.11 (e) and (f)).

Another observation from this experiment is that our polyimide foil presents an S-shaped deformation curve (Fig. 4.11 (g)) with a sudden increase before 100°C, a stable plateau between 100 and 300°C and finally a steep increase up to 344°C, when it breaks. This behavior suggests that during the first transition the polymer dries and excess solvent is removed. Then, chain elongation ensues and stabilizes during the observed plateau when the polymer reaches its final hard and stable form. Finally, as the temperature further increases, the film becomes more fluid as it approaches its melting point and a sudden deformation follows. At this point, the constant stress causes substantial necking on the polymer film, which further debilitates its structure and provokes its final rupture before reaching the melting point. In necking, the cross-sectional area of a material is reduced faster than its hardening ratio, causing a concentration of the strain in the regions of highest stress. For our experiments, this change in the cross-sectional area was mediated by the decreasing polymer’s viscosity as the temperature was increased. This deformation mode can explain the premature failure of the other polymer films studied, which also experienced a decrease in local cross-sectional area before their melting point.

Polymer	t(μm)	T_0	$T_m(^{\circ}\text{C})$	$T_{br}(^{\circ}\text{C})$	$A(\text{m}^2)$
PET	100	73.3 ²⁰²	250 ²⁰²	75	$2 \cdot 10^{-6}$
PEEK	100	145 ²⁰³	340 ²⁰³	150	$2 \cdot 10^{-6}$
Mylar	2.5	73.3 ²⁰²	250 ²⁰²	140	$5 \cdot 10^{-8}$
This work	1.7	300	325	344	$4 \cdot 10^{-8}$

Table 4.1: **Comparison of commercial polymers with the novel ultrathin polyimide foils.** The table summarizes the most important parameters involved in our study such as, thickness (t), glass transition temperature (T_g), melting temperature (T_m), breaking temperature (T_{br}) and cross-sectional area (A). This table is adapted from.⁴⁰

Temperature compensation via Wheatstone bridge

One of the most common strategies for temperature compensation for sensors and thin film applications is the Wheatstone bridge conditioning circuit. This methodology cancels out the fluctuations which are common to the elements comprising the bridge and allows scaling up sensitivity compared to the single sensor case. To

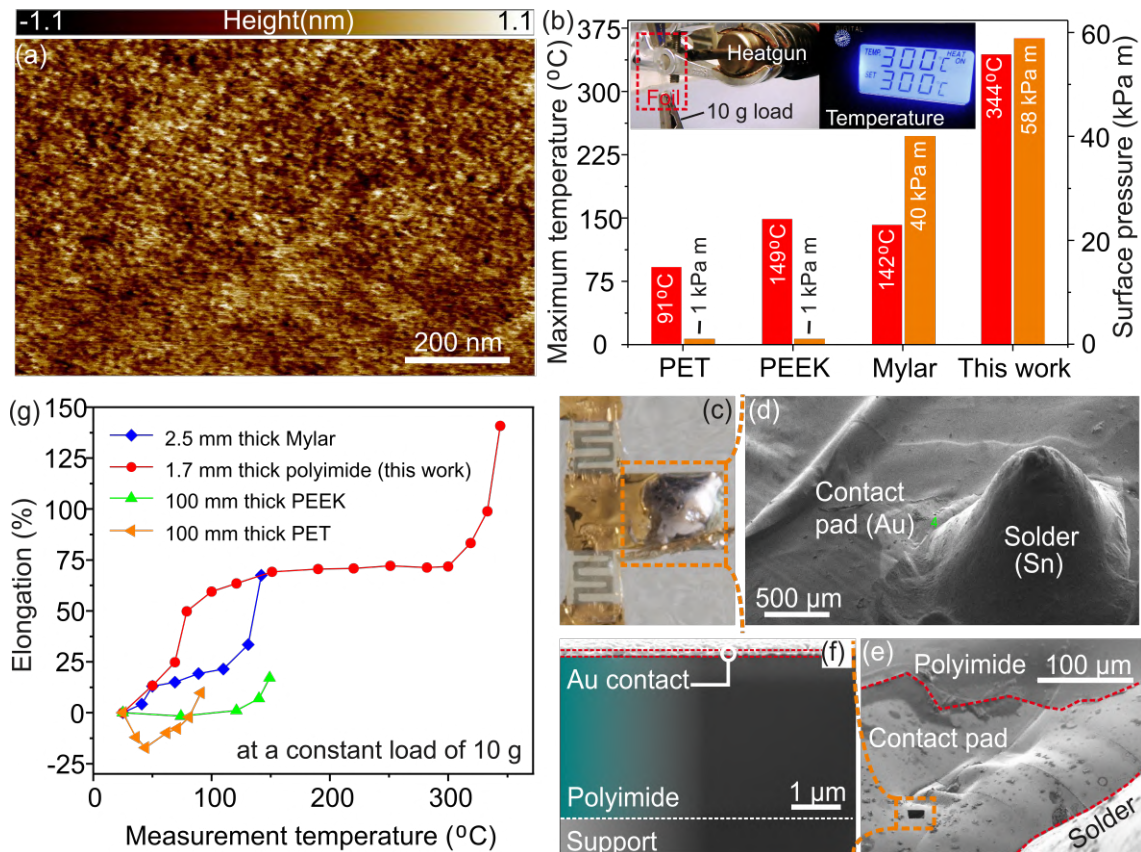


Figure 4.11: **Morphology and thermal performance of the polyimide foils.**(a) Atomic force microscopy (AFM) image of the 1.7- μm -thick foils. A height map of the imaged $1 \times 1 \mu\text{m}^2$ region of the foil reveals a flat surface with a root mean squared roughness of below 1 nm. (b) Maximum temperature, which the foils withstand (red-colored bars). For comparison, we used high performance commercial foils like 100- μm -thick PET, 100- μm -thick polyetheretherketone (PEEK) and 2.5- μm -thick Dupont's Mylar. During the experiment, each of the foils is clamped at the top and a constant load of 10 g is attached to the bottom. The foils are exposed to a heat flow of a heatgun. The 1.7- μm -thick polyimide foil withstands a continuous heating at 300°C at a constant load of 10 g attached to the bottom of the foil (inset in a). The corresponding surface pressure experienced by each foil is presented with orange-colored bars. Optical microscopy image revealing one of the locations with a soldered contact (c) and a corresponding SEM image (d). (e) Magnified SEM image (top view) of the surface next to the solder. (f) SEM image of the sample cross-section taken at the location of the contact pad next to the solder. The foils are clamped at the top and a constant load of 10 g is attached to the bottom of the foil. (g) Elongation of the foil as a function of the applied temperature as determined from experiment videos. The novel ultrathin polyimide foil, which is 1.7- μm -thick only outperforms commercial foils and carries the load up to the temperature of 344°C . Upon increasing the temperature, two transition regions are observed for the case of the polyimide foils. The first one at 100°C suggests a glass to rubber transition and the second one at 340°C points towards a sudden increase in fluidity (melting) before failure. This figure is adapted from. ⁴⁰

verify its effect in our experiments, we characterized the response of a single spin-valve sensor and its Wheatstone-bridge-conditioned version upon heating using a heat gun. A single sensor strongly responds even to slight temperature variation, however, no change in the readout of the bridge is observed upon the same heat treatment (Fig. 4.12).

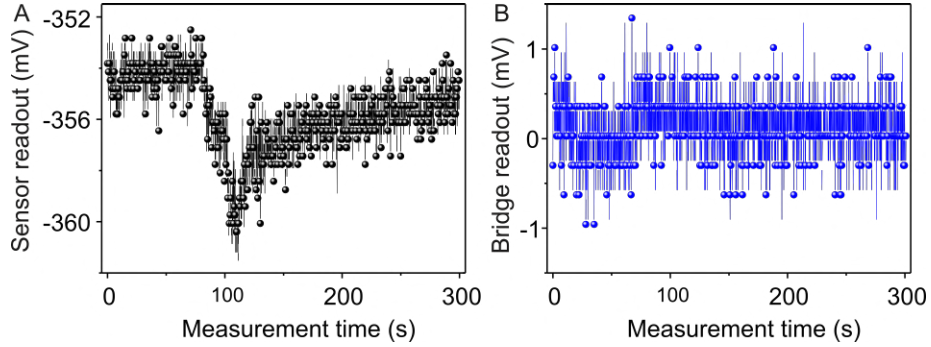


Figure 4.12: **Temperature compensation of the sensor bridge.** Time evolution of the electrical resistance of an individual spin-valve sensor (a) and a sensor bridge (b) upon heating. At about 60 s, both devices are simultaneously exposed to a heat flow from a heat gun. We find that the Wheatstone bridge arrangement successfully cancels out the temperature response of the individual sensors. This figure is adapted from.⁴⁰

This behavior arises from the intrinsic compensation properties of the Wheatstone bridge. The typical output characteristic V_{out}/V_{bias} of a Wheatstone bridge with resistors R_1 to R_4 can be written as in equation 2.16 in chapter 2. If $R_1 = R_3 = R_2 = R_4 = R_0$, the output voltage is 0 and the offset is fully compensated. In reality, however, the resistors vary (e.g. with temperature) and produce unwanted offsets. Assuming the case of varying resistors, with $R_1 = R_3 = R_2 = R_4 = R_0$ and a variation smaller than the nominal value of the resistors, second order terms can be neglected and the output/input ratio can be written as:

$$\frac{\Delta V_{out}}{V_{bias}} = \frac{\Delta R_1 - \Delta R_2 + \Delta R_3 - \Delta R_4}{4R_0} \quad (4.4)$$

If the resistance variation is produced by the change of temperature ΔT , it can be written as $\Delta R = R_0\alpha\Delta T$ (α is the temperature coefficient of resistivity):

$$\frac{\Delta V_{out}}{V_{bias}} = \frac{R_0\alpha\Delta T - R_0\alpha\Delta T + R_0\alpha\Delta T - R_0\alpha\Delta T}{4R_0} = 0 \quad (4.5)$$

As all the elements are expected to respond in the same way to temperature, they compensate mutually and the temperature-induced variations in the output voltage are eliminated.

Chapter 5

Geomagnetosensitive e-skins

5.1 Introduction

While the magnetosensitive e-skins in the previous chapter exploit the potential of common magnetic field sources, they require additional items like permanent magnets to create interactive stimuli. Eliminating these requirements could enable magnetosensitive e-skins to freely operate in any environment and ubiquitously interact with their surroundings. One way of reaching this goal is to tap into an omnipresent source of magnetic fields around us, like the earth's magnetic field or geomagnetic field. To this end, a new on-skin sensing concept relying on e-skin sensors capable of detecting the earth's magnetic field, must be developed. Numerous applications like artificial magnetoception or e-skin geomagnetic VR devices are envisioned to stem from this concept. To achieve this feat, the operating range of these new gadgets must match the small geomagnetic field of about 50 μT , which is out of reach for the magnetosensitive e-skins introduced in previous chapters.^{18,40} Consequently, a different technological approach must be implemented.

Technologies like flux-gate^{204,205} and Hall effect^{206,207} among other sensors,^{102,103,208} can be employed to measure the geomagnetic field. However, flux gate sensors cannot be easily manufactured in a thin film format and Hall effect sensors entail the use of overly complex readout circuits, which limits their application in flexible electronics. GMI approaches have also shown some promise,^{209,210} but they require the use of AC power supplies, which is again not easily translatable into a flexible format. MR methods, on the other hand, are straightforward to manufacture into thin films and their readout reduces to conventional DC resistance measurements. Nevertheless, not all MR sensors are suitable to detect the earth's magnetic field.

GMR and spin valve sensors offer large effects and potentially high sensitivity but their operating range ($> 1\text{mT}$) is way over the geomagnetic field. Some biasing or enhancing techniques²¹¹⁻²¹⁴ can be applied to tune their response for smaller fields, but the increase in fabrication complexity renders this endeavor too cumbersome for flexible technologies. A more viable alternative is to use AMR sensors (see chapter 2), which are smoothly integrated in flexible electronics and can be readily adjusted to detect the earth's magnetic field. For AMR sensors to detect the geomagnetic field, they must be geometrically conditioned to modify their intrinsic response. One of the most prominent methodologies for this purpose is the barber pole method,^{106,215-217} which is further explained in chapter 2. The following sections describe the fabrication and characterization of geomagnetosensitive e-skins

based on this methodology, and which application examples are envisioned to stem from them. The material presented next is adapted from a previously published work.⁴¹

5.2 Barber-pole-based geomagnetosensitive e-skins

In this method, stripes of ferromagnetic material are covered with slabs of a conductive material, oriented at 45° with respect to the long axis of the stripes. By performing this modification, the current is forced to flow at 45° in the stripes, which effectively linearizes their AMR response around zero magnetic field (see chapter 2 for more details). In this work, the barber pole structures were fabricated on ultrathin polymeric foils of Mylar, permalloy (Py) was selected as the ferromagnetic material and gold (Au) for the conductive slabs. The Py sensing structures were designed as meander structures, which are functionally equivalent to arrays of stripes connected in parallel and can be manufactured within a compact footprint

5.2.1 Fabrication and mechanical performance

To fabricate the barber pole geomagnetic e-skin we began with 6- μm -thin Mylar foils laminated to a rigid support based on polydimethylsiloxane (PDMS) coated glass slides. Separately, a 3D printed polylactic acid frame covering an area of $80 \times 50 \text{ mm}^2$ was used to pre-stretch 6- μm -thin foils by means of adhesive stripes on the frame edges. After pre-stretching, the PDMS coated glasses were flipped over, carefully pressed over the pre-stretched foil and cut by the edges with a scalpel for release. The resulting Mylar covered glasses were used as substrate for preparing the geomagnetic e-skin devices. Next, a standard two-step photolithography was performed on the Mylar foils using S1813 photoresist to define the stack of Py meanders and Au contacts (Fig. 5.1(a)). During the first step, 50-nm-thick films of Py were deposited on the Mylar foils by e-beam evaporation (pressure: $1 \cdot 10^{-8}$ mbar, rate: 0.3 \AA/s) preceded by a 5-nm-thin adhesion layer of titanium (Ti, pressure: $3.1 \cdot 10^{-8}$ mbar, rate: 0.3 \AA/s). In the next photolithographic step, Au contacts with a thickness of 100 nm were evaporated (pressure: $4 \cdot 10^{-8}$ mbar, rate: 3 \AA/s) and preceded by the same adhesion layer. The layout of the compass was designed as a full Wheatstone bridge where each of the 4 elements is a geometrically conditioned AMR sensor based on Py meander stripes (Fig. 5.1 (b)-(e)). This configuration is generally used to compensate for any thermal effects intrinsic to the metallic nature of the single sensors. In addition, it provides a way to scale the bridge output sensitivity as a function of the bias voltage of the bridge.

To evaluate the mechanical performance of the Py sensing layer on ultrathin foils, we measured the AMR response of single meanders under different curvature radii (Fig. 5.2 (a)). The meanders were placed in between pole shoes of an electromagnet and mounted on different curved sample holders with curvature radii ranging from 150 μm to 10 mm (Fig. 5.2 (b)). To ensure uniform in-plane incidence of the magnetic field, the sensors were mounted with their curvature axes perpendicular to the pole shoes axis (Fig. 5.2 (c)). The magnetic field of the electromagnet was swept between -10 and 10 mT and the AMR response of the sensors was simultaneously recorded. From the measurements, it was observed that the AMR effect remains unchanged at about 1.4% until bending radius of 150 μm when it slightly decreases to about

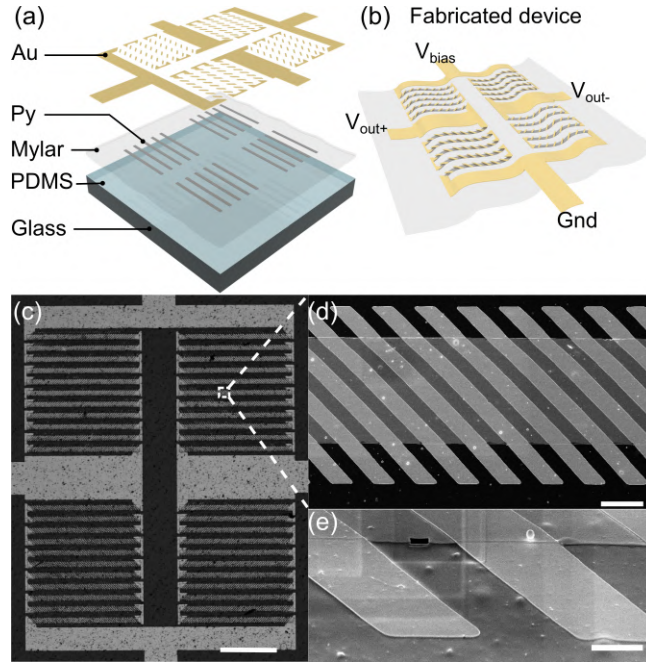


Figure 5.1: **Fabrication of the barber pole geomagnetic e-skin.** (a) Fabrication scheme (b) Device after fabrication and connection layout. (c) Optical micrograph of the fabricated device. The scale bar is 500 μm long. (d,e) Close-up SEM images of the upper right meander of the device. Scale bars are 20 and 5 μm , respectively. This figure is adapted from. ⁴¹

1.1% (Fig. 5.2 (d), upper panel). This change was accompanied by an increase in the electrical resistance, which suggests there might be some cracking involved as the Py film approaches its fracture strain (Fig. 5.2 (d), lower panel). The attained performance is at least one order of magnitude boost in bendability compared to AMR sensors prepared on thicker substrates [218, 219]. To examine the effects of dynamic bending, we carried out cyclic bending tests, where a single meander sensor is repeatedly bent from its flat state up to a curvature radius of 1 mm for 2000 cycles. The tests were performed on a LabVIEW-controlled motorized stage driven by a stepper motor (Eckstein, Germany). For the bending trials, the sample was laminated on a 5- μm -thin PDMS film (10 mm x 50 mm) and fixed to the frame of the motorized stage using a pair of clamps. One bending cycle was defined as bending the sample from its initial flat state to a bent state with a radius of 1 mm and back to its initial position (Fig. 5.2 (e)). Using these settings, two types of experiments were performed: one with an external magnetic field and the second one without. In both cases, the sample resistance was monitored using a multimeter (Keysight 34461A; Keysight technologies, USA). For the experiment without an external magnetic field, the sample was repeatedly bent for 2000 cycles and its resistance was simultaneously measured. For the experiment with an applied external magnetic field, all conditions were the same as indicated above, but a neodymium magnet was periodically brought near the sensor with an in-plane configuration during the cycling procedure. The collected resistance data in this experiment allowed us to compare the resistance change upon mechanical deformations with the one caused by the presence of the magnetic field (Fig. 5.2 (e)). We observed that the AMR response remains stable at about 1.4% even after 2000 bending cycles. At the same time the change of the

electrical resistance of the sensor due to mechanical deformations does not exceed 0.2% (Fig. 5.2(f)).

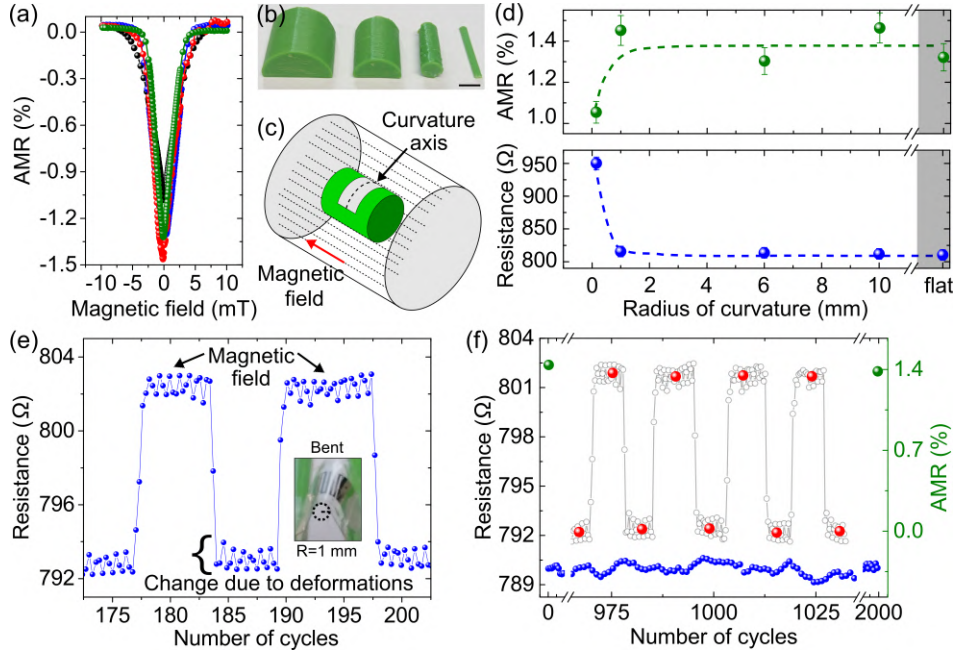


Figure 5.2: **Mechanical performance of the barber pole geomagnetic e-skin.** (a) AMR response of a single meander bent to different radii of curvature (150 μm in black). (b) Plastic curved holders used to bend the e-skin to different curvature radii. (c) Schematic showing how the curvature axis of the samples (in grey over the green holder) was placed perpendicular to the electromagnet poles to ensure that all the sample gets the same in-plane field. (d) AMR effect and nominal resistance for a single meander as a function of the radius of curvature. (e) Resistance as a function of the number of bending cycles. The fluctuations on the baseline correspond to the resistance change during the continuous cyclic bending tests. When a magnetic field is applied, the change is much larger as indicated by the two plateaus on the plot. (f) Comparison of the AMR performance and resistance change of a single meander as a function of the number of bending cycles. The blue dots represent the resistance variation upon mechanical cycling without a magnetic field. The inset with black open circles depicts the resistance change when an external magnetic field is applied (plateaus) during mechanical cycling. The red dots are introduced to highlight the average values at the baseline (no magnetic field) and the plateaus (with a magnetic field). This figure is adapted from. ⁴¹

To gauge the impact of mechanical deformations on the functional layer stack of the geomagnetic e-skin, we studied the morphology and integrity of its functional layers using scanning electron microscopy (SEM). We imaged the top surface of the devices as well as the cross-sectional cuts realized via FIB milling. The geomagnetic e-skin does not experience any film damage even for curvature radii as low as 200 μm (Fig. 5.3 (a),(b)). This result is about an order of magnitude smaller compared to the previous reports on flexible AMR sensors prepared on 100-μm-thick foils⁴⁹. This superior bendability of geomagnetosensitive e-skins is enabled by using ultrathin foils, which reduce the effective strain in the functional layers of the device [8, 17, 67, 82]. The following analytical calculations allow us to estimate the minimum bending

radius, defined by the critical strain in the layer stack, of the e-skin. Our analysis is based on the theoretical model for strain in curved thin film electronics shown in equation 2.3. For the Mylar[®] foil in this work, the corresponding parameters are $Y_s = 5$ GPa and $d_s = 6$ μm and for the compass layer stack: $Y_f = 119$ GPa and $t_f = 150$ nm. The value of 119 GPa corresponds to the thickness weighted average of the Py and Au films. First, this model can provide an insight on the maximum strain on the device by introducing the minimum experimentally measured bending radius of 200 μm (Fig. 5.3 (a),(b)). Using this parameter yields a maximum strain at the compass layer of 1%, which is not yet near the fracture strain (2%) for thin films of Py [220]. This indicates that the film can be bent below this value. Now, we can solve the model equation for the bending radius to define a minimum theoretical bending radius given by the 2% fracture strain of Py. Inserting this value in the equation gives a minimum bending radius of 100 μm .

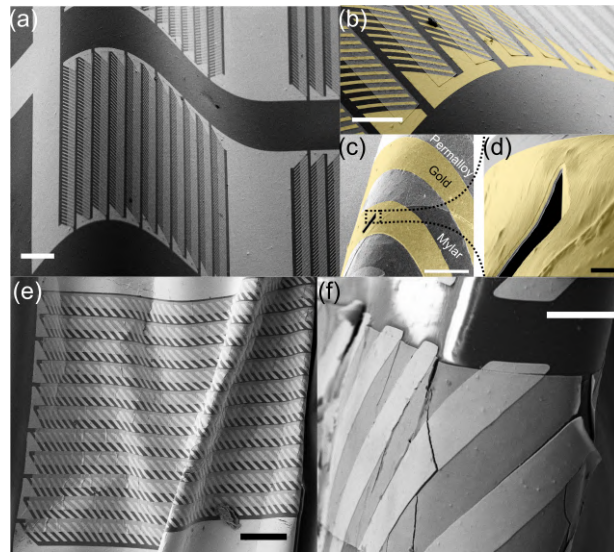


Figure 5.3: Morphological characterization of the barber pole geomagnetic e-skin upon bending. (a) SEM close-up image of the geomagnetic e-skin under a bending radius of 200 μm . (b) Structural details on the curved region. No damage is observed. Scalebars are 100 μm for images (a) and (b). (c) SEM close-up image of a region of the e-skin bent to a bending radius of 10 μm . The black square indicates the area examined via FIB. (d) Close-up of the FIB cross sectional cut depicted in (c). Scalebars are 10 and 1 μm , respectively. (e) Overview of the geomagnetic skin during extreme bending conditions (f) Close-up of the bent region showing an emerging crack in the structure. This figure is adapted from. ⁴¹

For comparison purposes, if we increase the thickness of the Mylar foil to that of a commercially available PET foil (100 μm) keeping $R = 200$ μm the resulting strain raises up to 24%, a value that would certainly induce cracking in the metallic films. These calculations further accentuate the importance of diminishing the substrate thickness to improve the overall mechanical performance of flexible sensors. This prediction agrees with experimental data, as occasional fracturing is observed when the sample is bent to a radius below 100 μm , also correlated with an increase of the sample resistance. When the sample bending occurs in a controlled manner, allowing for gradual stress relaxation to happen, only very incipient cracks occur (Fig. 5.3 (c)). Investigating the cross-section within the crack region reveals that

even in these extremely bent areas of the device, the integrity of the functional layers is preserved, and no delamination can be perceived (Fig. 5.3 (d)). However, when the bending is performed abruptly, e.g., by laminating the sample to a pre-stretched elastomer and allowing it to compress, pronounced dents and cracks can be observed (Fig. 5.3 (e),(f)). Thus, highlighting the importance of studying the stress dynamics in the sample for future works. Another advantage of the reduced thickness of the sensor on ultrathin films is the diminished stress (1% at 200 μm bending radius) on the metal layer. This is caused by the rather close positioning of the neutral mechanical plane (see chapter 2 for details) to the metal layer stack. The distance to the neutral mechanical plane can be readily calculated by means of Jeong's model presented in equation 4.1. The system was considered to have two layers: the Mylar foil ($Y_1 = 5 \text{ GPa}$, $\nu_1 = 0.38$) and the compass layer (Py and Au, $Y_2 = 119 \text{ GPa}$, $\nu_2 = 0.33$). With these parameters, the mechanical neutral plane b is located 4.2 μm above the bottom of the stack, i.e., 1.8 μm below the functional layer stack. The calculated strain in this situation with a distance $\delta = 1.8 \mu\text{m}$ from the neutral plane to the metallic layer is defined by $\epsilon = \frac{\delta}{R} = 0.94\%$ with a curvature radius $R = 200 \mu\text{m}$. With 100- μm -thick foils, the distance to the neutral mechanical plane is about 20 times larger, which also means a 20-fold increase in the strain at the functional sensing. Such a strain value would inevitably damage the functional layers of the device. However, if a capping encapsulation layer of about 6 μm is included, the strain at the layer could be nulled by placing the sensing layer exactly at the neutral mechanical plane.

5.3 Conditioning and magnetoresistive characterization

AMR sensors can detect magnetic fields in the range of mT, which are much larger than the earth's magnetic field (50 μT). However, upon geometric conditioning with slabs of gold oriented at 45° or 135° with respect to the long axis of the sensor stripes, the sensor response becomes linearized around zero field and the geomagnetic field can be detected (Fig. 5.4 (a)). This type of conditioning is known as barber pole method, which is the industry standard approach for AMR sensor conditioning.^{106,215–217} To select an optimal barber pole geometry, we studied the effect of geometrical parameters (slab separation, stripe length and stripe width) on the sensor response of single barber pole modified Py stripes (Fig 5.4 (a)). We checked how the separation between the slabs influences the sensor output and found out that the linearization effect aroused only at the separations of 10 μm for 50 μm wide Py stripes. Larger separation between slabs (25 μm) showed very little or no linearization effect at all (Fig 5.4 (b)).

This result can be attributed to the fact that at larger separations, the portion of the current which effectively flows skewed, is greatly reduced. Multiphysics simulations (COMSOL Multiphysics 5.2, USA) performed for this sensor geometry support this claim as seen in the surface current density plots for 10 and 30 μm slab separations (Fig 5.4 (c),(d)). When the separation is 10 μm , the surface current density is uniform over the majority of the permalloy regions (in cyan) and pinned at an angle of 45° (Fig 5.4 (c)). In contrast, when the separation increases to 30 μm , the current density is not uniform anymore, its magnitude decreases, and it is not fully pinned

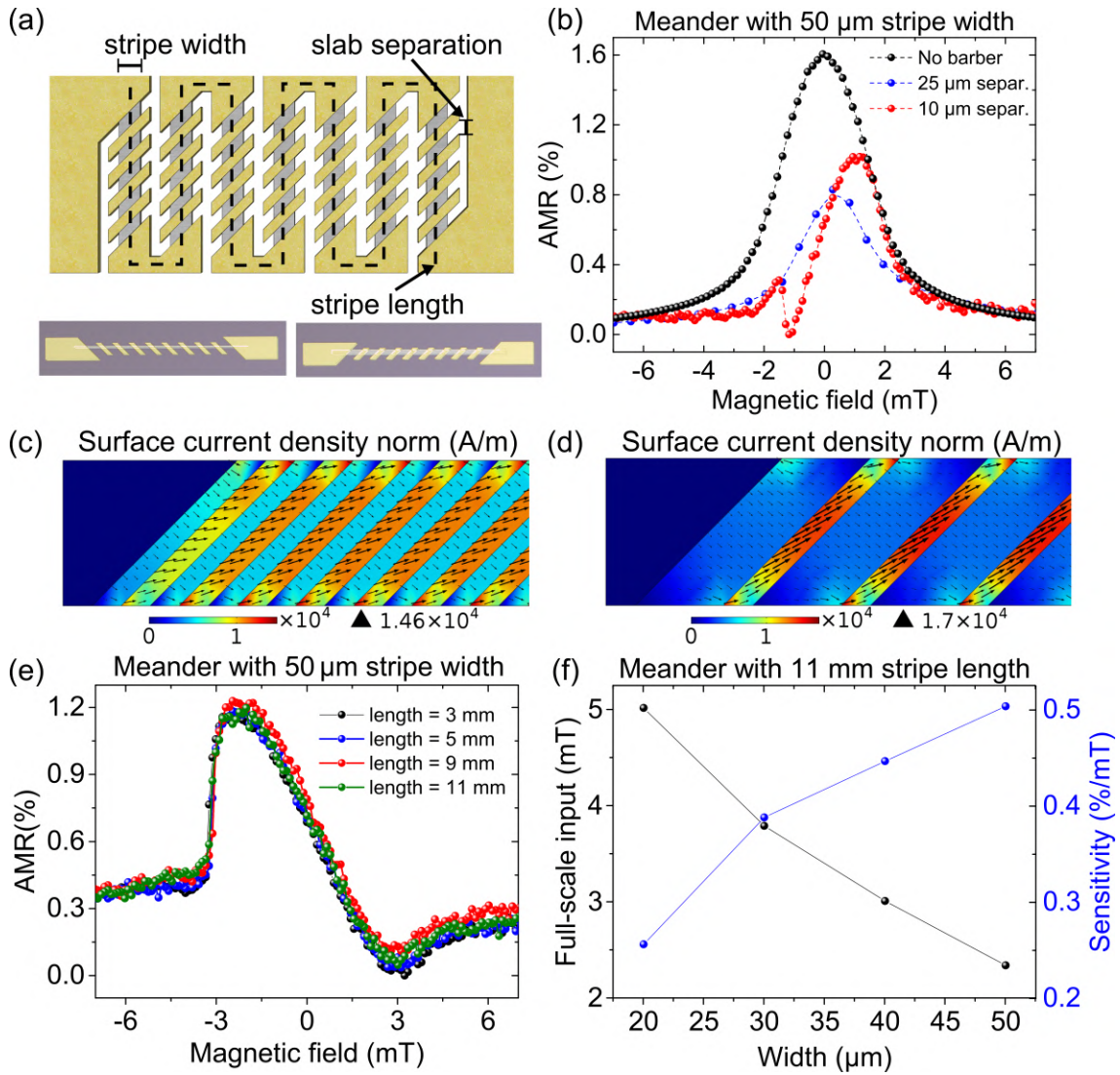


Figure 5.4: **Tuning effects of the geometric conditioning and aspect ratio of the sensors.** (a) Schematics describing the parameters of the meander sensors: stripe width, slab separation and stripe length, which were screened in this study to optimize the AMR response. The stripe length is signaled with a dotted line over the meander serpentine pattern. The stripe width refers to the width of the Py stripes drawn in gray underneath the gold contacts. (b) Effect of the slab separation on the linearization response. Only after a separation of 10 μm is reached (for the case of Py stripes with a width of 50 μm), the linearizing effect of the geometric conditioning dominates the AMR response. (c) Screening of the meander length for 50- μm -wide meander sensors. The length does not influence the AMR response of the sensor. (d) Full-scale input and sensitivity as a function of the stripe width for meanders with 11 mm strip length. As the stripe width increases, the sensitivity increases due to magnetic switching becoming easier with the Py size increase. However, at the same time, the full-scale input (linear region) of the sensor decreases, as the magnetic anisotropy is reduced, and the magnetic state of the sensor becomes less stable. This figure is adapted from. ⁴¹

at 45° (Fig 5.4 (d)). These results indicate that a smaller portion of the current travels pinned through permalloy, thus reducing the expected effect of the barber pole slabs. Next, we explored how the length and width of the ferromagnetic stripes affected the overall sensor response. For this purpose, we prepared meanders with stripe widths of 20, 30, 40 and 50 μm and monitored their AMR characteristics with and without modification. Changes in length did not affect the overall AMR response of the samples (Fig 5.4 (e)). For the modified meanders, it was observed that as the width of Py stripes decreased, the full-scale input (linear range) increased from ± 1 mT at 50 μm up to ± 2 mT at 20 μm . However, as the linear range increased, the sensitivity decreased from 0.54 %/mT at 50 μm down to 0.26 %/mT at 20 μm (Fig 5.4 (f)). This behavior is expected due to the larger shape anisotropy in narrower stripes, which renders the magnetization more stable (linear) but also much harder to switch (less sensitive).

As sensitivity is a more crucial performance metric for our geomagnetsensitive e-skins, we chose a stripe width of 50 μm for subsequent experiments. By controlling the orientation angle of the slabs, the sensor response can have a positive (for slabs oriented at 45°) or negative (for slabs oriented at 135°) slope (Fig. 5.5 (a),(b)). By contrast, if no conditioning is applied the sensor response is flat in the sub-mT range as shown by the black trace on Fig. 5.5(b). We combine both slab orientations within the same branch of a Wheatstone bridge to maximize the thermal stability and signal output range of the bridge. Optimizing the response of the bridge also requires tuning its bias voltage (Fig. 5.5 (c)). For a bridge with 20 μm wide stripes and single sensor sensitivity of 0.26 %/mT, its output sensitivity can be tuned from 5 $\mu\text{V}/\mu\text{T}$ at a bias of 2 V, up to 13 $\mu\text{V}/\mu\text{T}$ at a bias of 5 V (Fig. 5.5 (b)). However, it was found that bias voltages of 5 V dissipate too much heat and can damage the device due to the increased current density. Values of current of 1 mA were sufficient to ensure detection but also low enough to avoid unwanted thermal effects. Under these conditions, for a Wheatstone bridge with 50 μm wide stripes, a bias voltage of 2 V was found to be optimal.

Using the parameters obtained above (50 μm stripe width, 10 μm slab separation and 2V bias voltage), we achieved a single sensor sensitivity of 0.54 %/mT (Fig. 5.5 (b)). Upon arranging the sensors in a Wheatstone bridge configuration, the device operates as a compass and allows the detection of the earth's magnetic field. To evaluate its geomagnetic field detection capabilities, we designed an experiment where the device output voltage was monitored while being rotated in the absence of non-geomagnetic sources (Fig. 5.5 (d)). The output voltage was then plotted as a function of the angle between sensing axis of the device and magnetic north controlled by a reference smartphone compass (Fig. 5.5 (e)). The control of the setup was realized using a LabVIEW 2015 program (National Instruments, USA) to determine the angular position of a sample holder mounted on a stepper motor (green in Fig. 5.5 (e)). The samples were positioned 3 cm above the end of the shaft of the motor to ensure no disturbances from the in-plane component of the magnetic field generated by the motor.

As seen in figure 5.5 (d), the output voltage reconstructs a sinusoidal wave pattern with a maximum when the sensor directly aligns with north and a minimum when it points south. This behavior suggests that the signal detected might correspond to geomagnetic field. However, further experiments were performed to differentiate the

earth's magnetic field signal from possible spurious signals, as will be presented in the next section. A final remark about the operating range of these geomagnetsensitive e-skins is the, so called flipping effect.^{106,216} This effect arises when an incident magnetic field exceeds the linear operating range of the devices and causes their magnetization to flip and cause a hysteretic behavior. More specifically, the device response will be inverted upon successive magnetic field sweep rounds (black trace in Fig. 5.5 (f)), which is an undesired behavior. To correct for this, one methodology is to use a biasing field along the sensor axis (H_x), which stabilizes the magnetization and avoids flipping (Fig. 5.5 (f)). However, this implies the integration of permanent magnets or set reset coils which are both impractical for flexible electronic circuits.

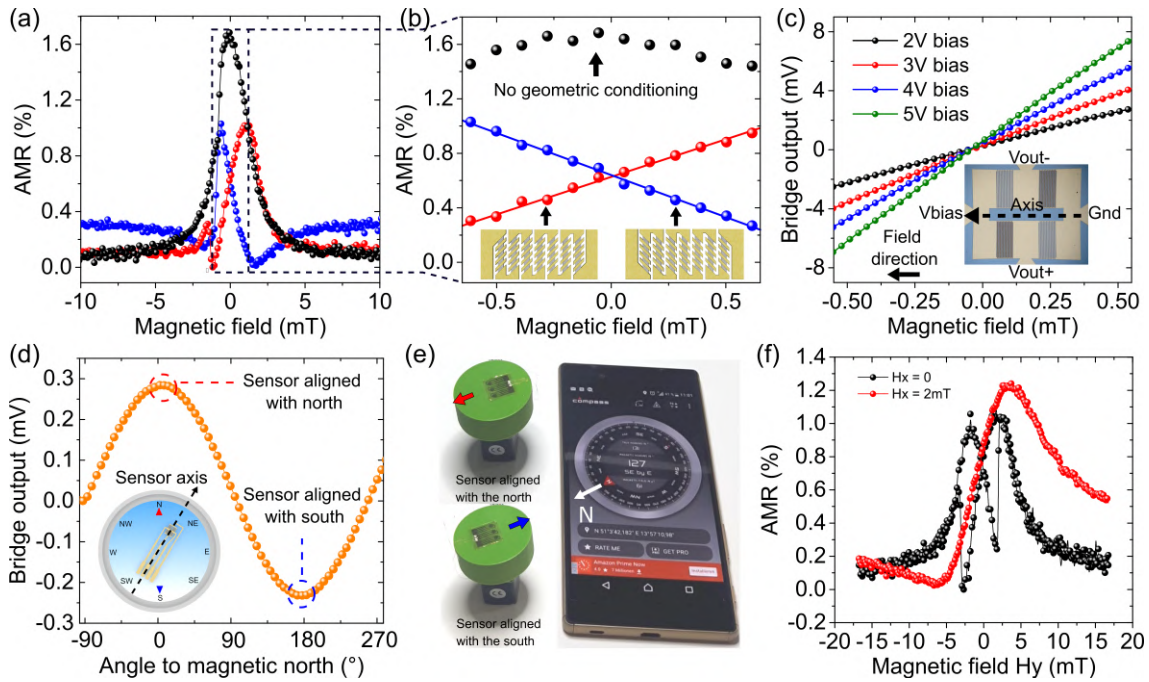


Figure 5.5: Magneto-resistive characterization and flipping effects in the geomagnetic e-skin. (a) Comparison of the AMR response of meander sensors with (red and blue) and without (black) geometric conditioning. (b) Close-up of the AMR response around the zero-field region. Without conditioning (black symbols), the sensors are not sensitive to small magnetic fields, i.e. geomagnetic field. Upon modification with barber pole structures, the sensitivity around zero field is substantially enhanced (red and blue symbols). Insets show the modified sensors with right and left oriented barber pole slabs, respectively, corresponding to the red and blue curves. (c) Bridge output voltage as a function of the magnetic field applied along the sensor axis. (d) Bridge output voltage as a function of the angle of the sensor axis to the magnetic north. (e) A reference compass monitored the direction of the magnetic north during these experiments and was used to track the geomagnetic alignment. (f) Flipping effects in the geomagnetic e-skin. The black trace indicates the AMR response in the absence of a biasing magnetic field along the sensor axis. The field was swept from negative to positive and back to negative to record the hysteresis of the system. The red trace indicates the results of the same field sweeping experiment in the presence of a biasing field of 2 mT. No hysteresis is observed. This figure is adapted from.⁴¹

5.4 Geomagnetic field measurements

To determine if the peaks detected by the e-skin compass always arise at the same geographical location (angular position), deliberate offsets of 90° and -90° with respect to the starting configuration (-108° to magnetic north) were introduced (Fig. 5.6 (a)-(c)). For each case (0° , 90° and -90°), the sample was rotated for 2 complete turns and the output voltage was recorded (Fig. 5.6 (d)). The acquired data was used to evaluate the corresponding phase shift of the signals. The extrema of the three measured curves are phase shifted according to their offset angle, indicating that the detected peak is consistently present at the same location (Fig. 5.6 (e)). To clarify if the detected output voltage peaks univocally correspond to the geomagnetic field, we introduced an external biasing magnetic field H_{coil} of $43 \mu\text{T}$ using a Helmholtz coil and measured the resulting output voltage V_{meas} (Fig. 5.6 (f)). From this voltage, we calculated the detected magnetic field from the bridge sensitivity given by: $S_{WB} = V_{bias} \cdot S_S$, in our case, with $V_{bias} = 1 \text{ V}$ and $S_S = 0.54 \text{ \%}/\text{mT}$, $S_{WB} = 5.4 \text{ mV}/\text{mT}$. Using this sensitivity and the linear relationship between voltage V and field H in the sensor ($V = S \cdot H$), we calculated the measured field H_{meas} from the peak voltage of V_{meas} ($68.91 \mu\text{V}$), which yields $12.76 \mu\text{T}$. Then, by subtracting the coil's magnetic field vector H_{coil} from the measured vector H_{meas} , we determined a reconstructed field H_{rec} as (Fig. 5.6 (g)):

$$|H_{rec}| = \sqrt{H_{meas}^2 + H_{coil}^2} = 44.85 \mu\text{T} \quad H_{rec}\angle = \tan^{-1} \frac{H_{coil}}{H_{meas}} = 73.47^\circ \quad (5.1)$$

Where $|H_{rec}|$ is the magnitude of the reconstructed vector and $H_{rec}\angle$ its angle to the sensor axis. These two values quantitatively correspond to those measured by the nearby reference compass. For further confirmation, we repeated the measurement in the absence of an external biasing magnetic field. In this case, the measured peak voltage V_{meas} was $242.78 \mu\text{V}$, which, using the same sensitivity as above, translated into a measured field H_{meas} of $44.95 \mu\text{T}$ (Fig. 5.6 (h)). This value closely agrees with the reconstructed value obtained before. Furthermore, by using the temporal shift between V_{meas} with the coil on and V_{meas} with the coil OFF, we estimated the angle between both vectors. This was accomplished by determining the time needed for a 180° turn to be completed (13.35 s) and comparing this time with the temporal shift between the detection peaks in the on and off cases (5.283 s). The ratio of these two quantities multiplied by 180 gives the approximate angle between detection events (71.21°); in close agreement with the previously reconstructed angle $H_{rec}\angle$.

The above-mentioned results demonstrate the consistent reconstruction of the geomagnetic field signature (magnitude and orientation) and confirm the detection capabilities of our device. In all detection events, the measured peak-to-peak voltage was $496 \mu\text{V}$, which defines the available voltage range for encoding 180° and yields an angular sensitivity of $2.5 \mu\text{V}/^\circ$. The effective resolution of the device is ultimately restricted by the noise, which was measured to be $0.9 \mu\text{V}_{RMS}$. Assuming a detection margin of twice the noise, i.e. $1.8 \mu\text{V}$, the resolution of the geomagnetic e-skin is about 0.7° , which is in the same order of magnitude as commercial rigid compasses⁵⁸. In addition, thermal drift effects were found not to hinder the performance of the sensor, as shown by thermal (Johnson) noise calculations. The intrinsic Johnson noise for the Wheatstone bridge output of our device (equivalent resistance of $1 \text{ k}\Omega$) at room temperature (300K) is given by:

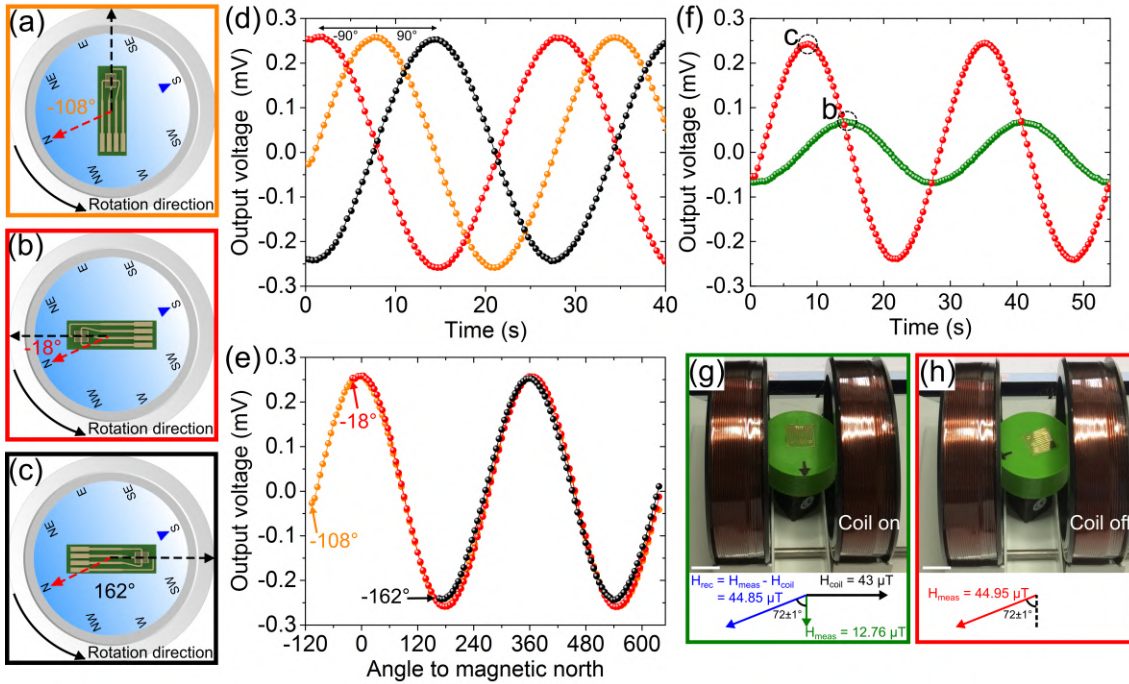


Figure 5.6: **Detection of the earth's magnetic field upon rotational offset.** (a-c) Starting positions of the geomagnetic-skin superimposed to a virtual compass highlighting their orientation with respect to magnetic north. The sensor axis is given by the black dotted arrow and magnetic north is indicated in red. All samples were rotated counter clockwise. (d) Output voltage curves during a rotation experiment for the e-skin compass starting from 3 distinct positions respectively offset 90° to each other. The maxima and minima in the plot closely follow the deliberate offsets introduced indicating that magnetic north and south arise always at the same geographical locations. (e) Output voltage as a function of the angle to magnetic north. Plotting with respect to the angle reveals that the detection of magnetic north and south occur at the same angle for the 3 offsets introduced in panel (d). (f) Measured output voltage curves of the e-skin compass upon counter-clockwise rotations in the presence (green) and absence (red) of an external biasing magnetic field of $43 \mu T$ provided by a pair of Helmholtz coils. (g) Snapshot showing the instant corresponding to the detection peak in the presence of a biasing magnetic field (coil ON). From the orientation and the magnitude of the measured magnetic field vector (H_{meas}), the geomagnetic field can be reconstructed (H_{rec}) by subtracting the known applied biasing field (H_{coil}) from H_{meas} . (h) Snapshot of the showing the instant corresponding to the detection peak in the absence of a biasing magnetic field (coil OFF). With no biasing magnetic field, the only measured field (H_{meas}) must be the geomagnetic field. The orientation and magnitude of the measured vector closely correspond to the values reconstructed in (g), further confirming the detection of the geomagnetic field. This figure is adapted from. ⁴¹

$$\frac{V_n}{\sqrt{\Delta f}} = \sqrt{4K_BTR} \quad (5.2)$$

Which yields a value of $4.06 \text{ nV}/\sqrt{\text{Hz}}$. Effectively, the thermal noise of our measurements is defined by that of the read-out electronics ($55 \text{ nV}/\sqrt{\text{Hz}}$ [Keithley 34461A datasheet]), since it is significantly larger than that of the sensor. To acquire a full picture of the noise spectrum, we measured the output voltage noise over 50 thousand samples and converted it to the frequency domain via FFT (Fast Fourier Transform). From the frequency plot we determined the corner frequency of the measurement to be about 20 Hz (Fig. 7). Using this frequency, the previously determined output sensitivity of 5 V/T @ 2 V and the Johnson noise value for the electronics, the detection limit was found to be 49 nT . Introducing low noise electronics of about $15 \text{ nV}/\sqrt{\text{Hz}}$ would further enhance the limit of detection of our device to 13 nT . Overall, these results represent a two orders of magnitude improvement in the field detection range over previous e-skin angle sensors[40]. Furthermore, contrary to magnetoimpedance based flexible sensors[210], the geomagnetic e-skin does not require any external biasing magnetic field and operates at 1 mA direct current.

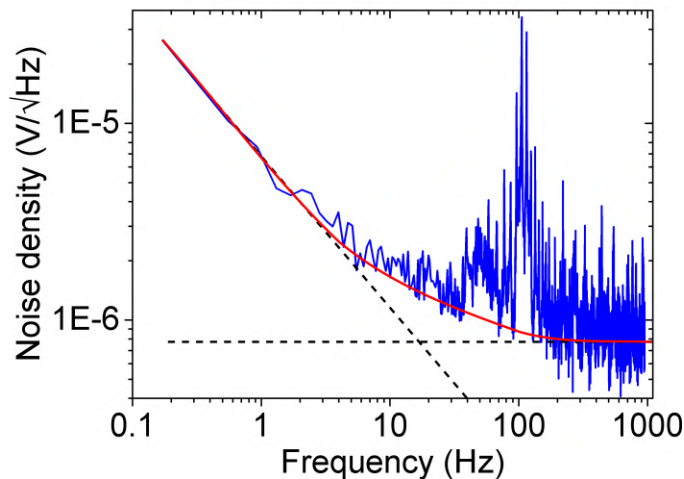


Figure 5.7: **Thermal noise of the e-skin compass.** Noise density as a function of frequency for the e-skin compass. By determining the crossing of noise base level and the $1/f$ noise portion of the data, the corner frequency of the device can be determined. This figure is adapted from. ⁴¹

5.5 Application examples

5.5.1 E-skin geomagnetic orientation in the outdoors

The key part of demonstrating artificial magnetoception with geomagnetsensitive e-skins, is to prove that in total absence of man-made magnetic sources they can still detect the geomagnetic field. Hence, we devised an open-air experiment, where the e-skin was attached to a person's index finger to indicate his current orientation (Fig. 5.8 (a)). Then, the person rotated his body within the geomagnetic field and the output voltage of the geomagnetic e-skin was read out in a computer. During

the experiment, the e-skin compass was connected to and powered by a NI-USB 6211 data acquisition box (National Instruments, USA) interfaced with a laptop running a LabVIEW program. The software was used for visualizing the collected output voltage both as a trace and as an on-screen virtual compass indicator. The measurements were performed in a nearby meadow at the coordinates 51.061851 N, 13.950389 E with the setup shown in Fig. 5.8 (a) and the computer screen facing northeast. The output voltage of the e-skin was stored as a function of time while simultaneously filming the experiment during a north-south-north transition (valley in Fig. 5.8 (b)).

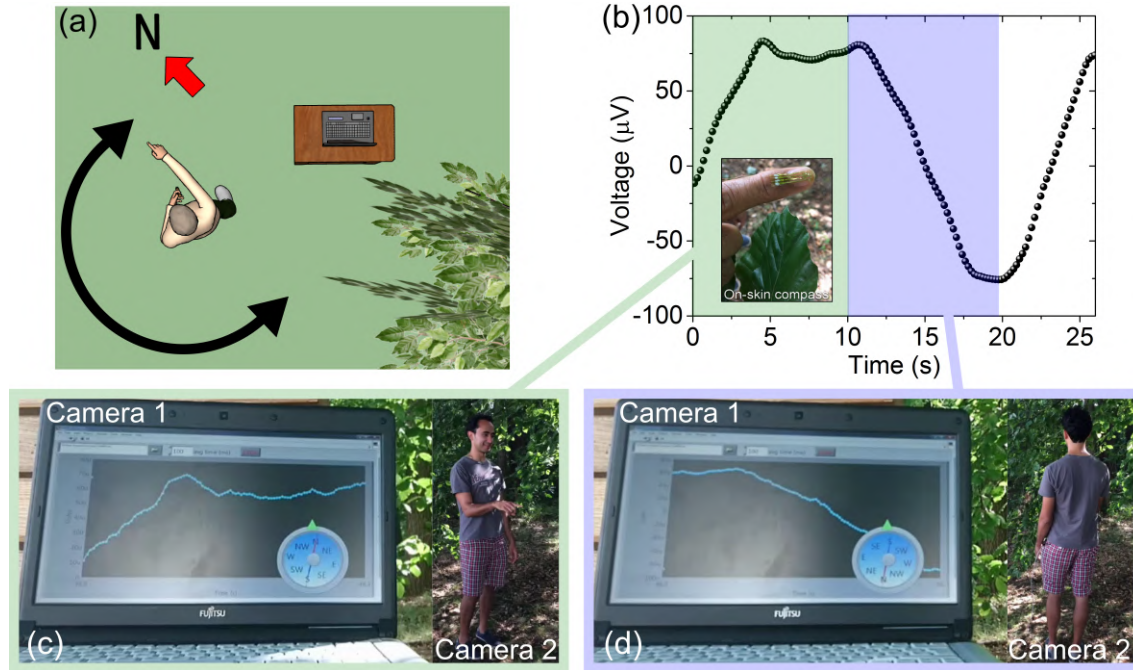


Figure 5.8: **On-skin geomagnetic orientation setup.** Time evolution of the output signal and snapshots of the Supplementary Movie 4. (a) Setup of the experiment showing the rotation of the person wearing the e-skin compass. The direction of the magnetic north is depicted with a red arrow. (b) Time evolution of the output voltage during a recorded video of the experiment. The plateau between 5 and 10 s corresponds to the magnetic north and the small one between 17 and 20 s to the magnetic south. Movie snapshots corresponding to the first (c) and last (d) parts of the trace, corresponding to north and south rotations respectively. This figure is adapted from.⁴¹

Two cameras were used to film the experiment, the first one recorded mainly the laptop screen and the second one recorded the full body motion of the person (Fig. 5.8 (c) and (d)). The snapshot in Fig. 5.8 (c) depicts the transition from the initial position up to north where the position was held for approximately 5 s (plateau). Correspondingly, the snapshot in Fig. 5.8 (d) shows the transition from north to south and back to north again (valley). Throughout the experiment, the finger bearing the geomagnetic e-skin (Fig 5.9 (a)) was kept parallel to the ground to read only the in-plane component of the field. The rotation was performed back and forth between magnetic north (N) and south (S) via west (W) (Fig 5.9 (b)), with all the orientations being verified by a reference compass. From the video

we selected several representative frames (N, S, and W) which are shown in Fig. 5.9 (c)-(e) together with a superimposed dial indicating the current heading of the person. These results show for the first time an on-skin device, which can replicate the functionality of a compass and enable artificial magnetoception for humans.

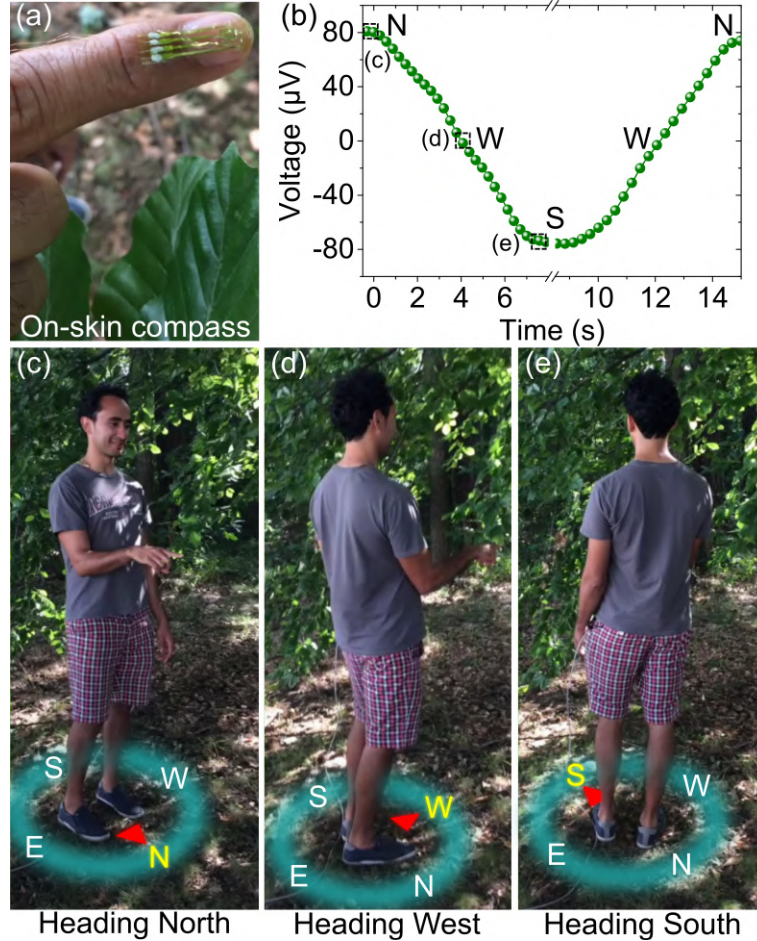


Figure 5.9: **Outdoor geomagnetic detection.** (a) Geomagnetic e-skin attached to the finger of a person. (b) Time evolution of the output voltage of the geomagnetic e-skin when the person rotates back and forth from the magnetic north (N) to magnetic south (S) via west (W). (c-e) Snapshots of a movie showing the instants when the person points to N, W and S. A dial with the cardinal points is overlaid on the snapshots to signal the corresponding orientations. This figure is adapted from.⁴¹

5.5.2 Geomagnetic virtual reality control

Another application area where we foresee the potential of geomagnetsensitive e-skins is AR or VR. In this case, the geomagnetic e-skin will act as a mechanically compliant interactive input device capable of directly translating the real world magnetoception into the virtual realm. To evaluate the functionality of the e-skin compass within a virtual reality environment, we set up an experiment where we used the output voltage of the compass to control the orientation of a virtual panda inside Panda3D, a python-based game engine[221]. First, the compass was placed on a person’s middle finger to define an axis of directionality and interfaced to a

computer using a NI-USB 6211 data acquisition box. On the computer side, the acquired data was processed in LabVIEW and then read by a Python script. The script calls the Panda3D (Disney / Carnegie Mellon, USA) game engine for Python and C++, which used the incoming compass data to correspondingly control the orientation of an animated panda on-screen. A python script commanded the virtual panda to move forward at a constant speed and the angular rotation was determined by the relative angle of the hand to the magnetic north. This angle was attained by encoding the output voltage of the e-skin compass between 0 and 180°, with magnetic north (0°) corresponding to a hand rotation towards the left of the screen. Sequential movement of the hand was used to move the panda within a defined trajectory in the virtual environment (Fig. 5.10).

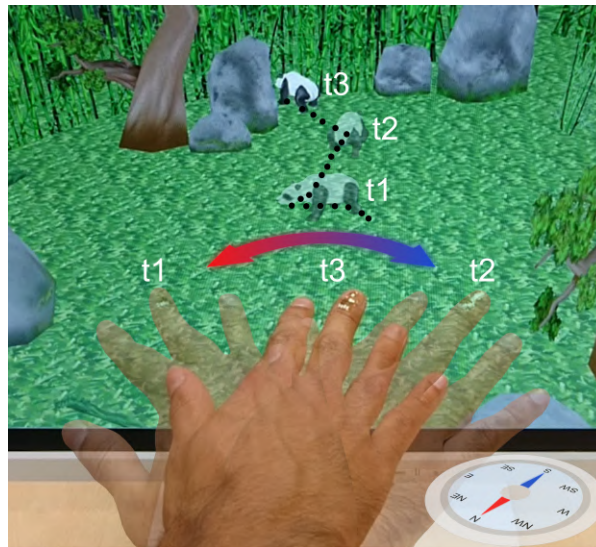


Figure 5.10: **Geomagnetic interaction with a virtual reality environment.** Control of the trajectory of a virtual character (panda) by hand motion in the geomagnetic field. Moving the hand closer to magnetic north (to the left) commands the panda to face left (t_1). An opposite movement to the right directs the panda towards the screen (t_2). A hand motion to the center steers the panda slightly to the left at an angle in between the first two orientations (t_3). This figure is adapted from. ⁴¹

All of this was achieved without the aid of any permanent magnet or optical sensory system as typically used in VR applications. The entire experiment was recorded in a video from which we selected and superimposed three representative frames, correspondingly displayed on Fig. 5.10. On the lower right, a compass drawing is included to indicate the physical location of north during the experiment. Here, the trajectory of the panda is highlighted as a dotted line and the frames of interest are correspondingly labeled with the times t_1 to t_3 . In the first frame (t_1), the person moved his hand to the left, moving closer to magnetic north and thereby orientating the panda to the left of the screen. In the following frames, the hand swung back to the right, i.e., towards magnetic south (t_2) and then came back to the center at a neutral position (t_3). In each case the virtual panda correspondingly rotated within its local reference axis going into the screen and then diagonally towards the left to reach its last position. These results showcase the first on-skin and entirely compliant gadget able to manipulate a virtual object in a geomagnetic field.

Chapter 6

Sub- μT magnetosensitive e-skins

6.1 Introduction

A natural progression beyond geomagnetosensitive e-skins is the development of even more sensitive e-skins which can access not only ambient but also biomagnetic fields. Usually, these fields are extremely small, ^{222,223} ranging from nT (chest) to fT (brain) and require very bulky detection schemes like induction coils ^{224,225} or SQUIDs. ²²³ Furthermore, point-of-care diagnostics could also greatly benefit from the development of more advanced magnetosensitive e-skins which can detect magnetic fields below 1 μT . Accessing tiny fields enables the development of versatile and accurate biomedical platforms for magneto-cytometry, imaging, magneto-cardiography and encephalography. ^{184,226,227} Similarly, as explained in previous chapters, the fabrication process must be simple and compatible enough with flexible electronic techniques, which so far has not been accomplished. Some attempts have been made using GMR ²²⁸ or GMI ^{209,210} devices, yet the complexity of the fabrication or the biasing schemes limits their integration in flexible platforms. In addition, the approach used for developing geomagnetosensitive e-skins in the previous chapter requires considerable modification in order to reliably detect sub- μT magnetic fields. An alternative approach is to employ another effect present in thin films, namely, the planar Hall effect (PHE), which is intrinsically linear and very sensitive ²²⁹ around zero field. In addition, as this effect is present in metallic thin films, it can be seamlessly adapted to flexible electronics without the need for any geometric conditioning. In this section, we present the development and characterization of sub- μT magnetosensitive e-skins based on the PHE and illustrate some of the possible applications of such an approach. The material presented next is based on fabrication technologies and characterization techniques developed by me, and experimentally carried out by Pablo Granell and Gouliang Wang, who worked under my supervision. The sections below describe the most prominent results of a recently published paper ⁴² stemming from this collaboration.

6.2 Fabrication process

For preparing compliant PHE sensors, commercial 6- μm -thick PET based Mylar foils (Chemplex Inc., USA) were attached to a glass slides for convenient manipulation during lithography and metal evaporation. The layout of the PHE sensors was conceived as 20- μm -thick Py Hall crosses deposited on the previously established

support (Figure 6.1 (a)). The Py structures were photolithographically defined using the same methodology described in the fabrication section of chapter 6. After patterning, a 20-nm-thick layer of Permalloy ($\text{Ni}_80\text{Fe}_{20}$) was deposited by electron beam evaporation (pressure: $8 \cdot 10^{-8}$ mbar; deposition rate: 1.3 \AA/s), followed by the evaporation of a protecting 3-nm-thick Au capping layer (pressure: $6.2 \cdot 10^{-8}$ mbar; deposition rate: 2.4 \AA/s). To improve sensor performance, each stripe of the Hall cross was prepared with a high aspect ratio of 10:1 to induce a preferred magnetization axis of the Py structure by shape anisotropy. Further enhancement was achieved by patterning an elliptically-shaped stripe instead of a rectangular one.²³⁰ In a second fabrication step, electrical contact pads consisting of [Au(100 nm) / Ti(3 nm)] bilayers were e-beam evaporated (pressure: $2.2 \cdot 10^{-8}$ mbar (Ti) and $5.5 \cdot 10^{-8}$ mbar (Au); deposition rate: 0.2 \AA/s (Ti) and 5.5 \AA/s (Au)) to interface the Hall crosses with the outside electronics. Lastly, the fabricated devices were delaminated to obtain freestanding ultrathin PHE sensors (Fig 6.1 (a)) to be investigated for their mechanical properties. Upon bending the sensor perpendicularly to its elliptical arm, down to a radius of $500 \mu\text{m}$, no cracks or signs of structural damage were found (Fig 6.1 (b)).

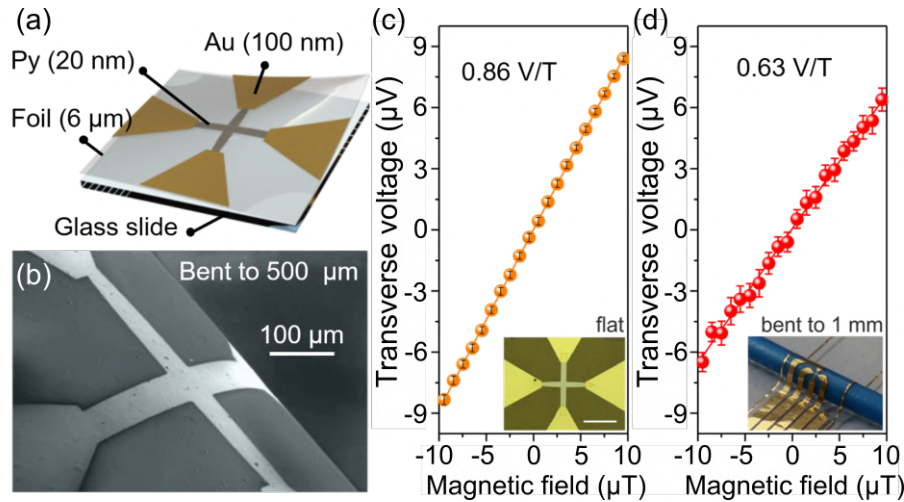


Figure 6.1: **Fabrication, imaging and measurement of PHE e-skins.** (a) Main components of the highly compliant PHE sensors. (b) SEM imaging of a compliant PHE sensor in bent to a curvature radius of $500 \mu\text{m}$. (c) Transverse voltage (planar Hall voltage) measured for a compliant PHE sensor in the flat state (average of 5 measurements) and (d) bent to a radius of 1 mm (average of 7 measurements). This figure is adapted from.⁴²

6.3 Magnetoresistive characterization

To assess the magnetotransport properties of the fabricated sensors, they were probed in a setup comprising a Helmholtz coil, supplied with DC current by a Keysight B2902A SMU. The magnetic field generated by the Helmholtz coils was calibrated with a Gaussmeter (Goudsmith Magnetic Systems, Netherlands). A second channel of the Keysight B2902A was used to source a DC current bias of 5 mA to the sensor during the measurements. The DC output voltage from the perpendicular arms of the cross was read out with a Keysight 34461A multimeter.

To define a preferential magnetization on the sensor, a magnetic field parallel to the elliptical arm of the Hall cross was applied and swept in the range of ± 3 mT. This field value drives the elliptically-shaped Py stripe into saturation and initializes the device for further experiments.²³¹ According to this alignment, the sensitivity axis of the sensors was defined to be for magnetic fields applied parallel to the elliptical axis. Figure 6.1 (c) and (d) show a comparison between the magnetoresistive response of the sensors when measured flat and when bent to a curvature radius of 1 mm. In the flat state, the sensors showed a maximum sensitivity value of 0.86 V/T and a highly linear response when biased with a 5 mA DC. These measurements also indicate that the minimum magnetic field strength detected can be lower than 200 nT in the flat state, as observed in the error bars of Fig. 6.1 (c). Even when bent to 1 mm, their sensitivity still achieves a remarkably high value of 0.63 V/T and a limit of detection of 500 nT, as observed in Fig. 6.1 (d). The observed change in the sensitivity after bending can be attributed to the modification of the magnetic domain pattern due to magnetostrictive effects. To assure a direct comparison of the measurements of the same sensor between the bent and flat states, the magnetic state of the sensor was not reinitialized between the measurements in the flat and bent states. The change of the magnetic domain pattern in magnetic thin films upon bending has been investigated in other works.^{227,232,233}

One of the great advantages of metal-based PHE sensors is their small resistance, which yields very low intrinsic sensor noise values. Noise in planar Hall effect sensors comprises $1/f$ noise (drift) and Johnson noise.²³⁴ The $1/f$ noise (drift) part of the noise spectrum is mainly caused by ambient, mechanical, magnetic or electrical contact sources. It must be noted that especially the mechanical drift is much higher when the sensor is bent, leading to a larger scatter in the data for our bent sensor (Fig. 6.1 (d)). The intrinsic thermal noise density of the sensor was calculated using Equation 5.2 with $R = 105 \Omega$, and $T = 300$ K; to yield a noise figure of $1.3 \text{ nV}/\sqrt{\text{Hz}}$. This notably low noise figure represents a 4 times improvement with respect to barber pole conditioned AMR sensors (6.1). In practice, this value is only compromised by the external noise of the read-out electronics, $55 \text{ nV}/\sqrt{\text{Hz}}$ in our case. Using low noise electronics with typical white noise densities of $15 \text{ nV}/\sqrt{\text{Hz}}$, would enhance the limit of detection of the compliant PHE sensors to 10 nT.

E-skin type	Thermal noise ($\text{nV}/\sqrt{\text{Hz}}$)	Min. detected field (nT)
Barber pole AMR	4	1000
PHE	1.3	200

Table 6.1: Comparison of e-skins with high sensitivity at low magnetic fields.

6.4 Compliant PHE sensors for detecting magnetic stray fields

Owing to their excellent mechanical properties, these sensor devices are versatile enough to curve around small magnetoelectric objects and detect the tiny magnetic fields emanating from them. This advantage could be used for example when monitoring magnetically functionalized objects flowing in a fluidic channel, or the

stray magnetic field generated by a current-carrying wire. As a proof of concept, the performance of the PHE sensors was evaluated by measuring the magnetic field generated by a pulsing DC current in a stranded copper wire with an outer diameter of 2 mm (nominal insulation thickness of 0.45 mm). During the measurement, the sensor was wrapped around the wire to be in the closest proximity to the magnetic field source, while 100 mA current pulses were applied (Figure 6.2 (a)). The estimated magnetic field around the wire was calculated to be about $20 \mu\text{T}$, which is in the same range as those arising in magneto-fluidic experiments.^{184,235} Throughout the experiment, the PHE voltage was recorded while manually switching the DC current circulating through the wire between its ON and OFF states. The results of this experiment show that the output voltage signal follows the polarity and magnitude of the manual pulses applied (Figure 6.2 (b)). Furthermore, the linearity of our sensor is preserved, as the voltage magnitude of the signal remains unchanged even when the current is reversed. From this result, it can be inferred that true magnetic field effects are being measured, instead of just the temperature variation upon Joule heating of the wire. Moreover, the performance of the compliant PHE sensors is comparable with the conventional bulky and rigid clamp meters applied for current sensing.²³⁶

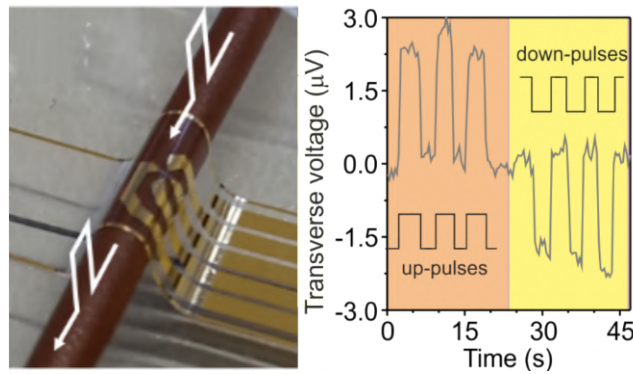


Figure 6.2: **Magnetic stray field detection with PHE sensors.** (a) A compliant PHE sensor wrapped around a copper wire with a radius of 1 mm. White arrows represent schematically DC current pulses in the wire. (b) Transverse voltage measured by the sensor, clearly separating the incoming current pulses of different polarity. This figure is adapted from.⁴²

Chapter 7

Summary and outlook

7.1 Summary

The aim of this thesis was to realize ultrathin and flexible magnetosensitive e-skins, to mediate human-machine interactions by fully exploiting the directionality of magnetic fields. We researched three possible sources for magnetic field interactions; permanent magnets (chapter 4), the geomagnetic field (chapter 5) and sub- μT magnetic fields (chapter 6), as we now recapitulate:

- **Magnetosensitive e-skins with directional perception:** Here, the concept of magnetosensitive e-skins with directionality was first introduced, with the aim of enabling touchless interactions which involve turning or rotation. As a proof-of-concept, the sensing range of the e-skins was selected to span the magnetic field range of standard permanent magnets. A fabrication scheme based on a nested Wheatstone bridge design consisting of spin-valve sensors on ultrathin polymeric substrates was presented and completed. To this end, a transfer printing method for ultrathin foils was developed and established. Numerous magnetoresistive tests were conducted to validate the angular reconstruction capabilities of the manufactured e-skins. The outcome of these tests was a theoretical angular resolution of 7° , which can be modified by changing the size of the external magnetic source. Mechanical and morphological experiments were run to determine the reliability of the e-skins under extreme bending conditions. SEM investigations showed no cracks for bending radii as low as $30\ \mu\text{m}$. Only for curvature radii below $10\ \mu\text{m}$ occasional cracks were identified. Strategies to reduce the mechanical strain on the sensing layers were proposed and implemented based on available theoretical models. Application examples involving discrete (touchless keypad) and continuous (touchless dial) angular encoding for virtual reality were showcased. Reliability tests were carried out to address possible encapsulation, angular resolution and temperature stability issues. Overall, it was demonstrated that these magnetosensitive e-skins can withstand bending radii of about $100\ \mu\text{m}$ while remaining functional, a feat which conventional magnetic sensors cannot achieve. This remarkable behaviour owes to their ultrathin nature which drastically reduces mechanical strain at the sensing plane of the e-skins. It can be concluded from the magnetoresistive, mechanical and reliability tests performed that magnetosensitive e-skins can successfully operate under the stringent conditions required by wearable on-skin electronics. These results represent the first mechanically

imperceptible and ultraflexible electronic skin able to track body motion via magnetic stimuli.

- **Geomagnetosensitive e-skins:** In this chapter, a new kind of magnetosensitive e-skins able to detect the earth's magnetic field was presented. The core of this development consisted of barber-pole modified AMR sensors in a Wheatstone bridge arrangement, fabricated on ultrathin plastic substrates. For this purpose, special processes were developed to counter the lithographic alignment problems arising due to the malleable nature of the substrates. The effects of the barber pole geometry were studied and understood to find the optimal configuration in terms of linearity and sensitivity. It was determined that barber pole separations of 10 μm are required to observe a substantial linearization effect. Several experiments were conducted to probe the angular geomagnetic detection capabilities of the fabricated e-skins under different orientations and magnetic configurations. Vectorial reconstruction experiments unambiguously showed that the detected magnetic field corresponded to the geomagnetic field of about 50 μT . Calculations of the thermal noise during the measurements were carried out to establish the minimum magnetic field resolution of the system. The results yielded a detection limit of 49 nT, which can be improved to 15 nT if low-noise read-out electronics are used. Static and dynamic bending tests were carried out to determine when and if the fabricated e-skins would fail. The geomagnetosensitive e-skins do not experience any film damage even for curvature radii as low as 200 μm . This result is about an order of magnitude smaller compared to previous reports on flexible AMR sensors prepared on 100- μm -thick foils²¹⁹ and is explained by their ultrathin form factor. Dynamic bending tests demonstrated unaffected magnetic field detection even upon 2000 cycles to a curvature radius of 1 mm, which is a state-of-the-art result for e-skin magnetic sensors. The results of this chapter showcase with two demonstrators, the first e-skin, which can enable artificial magnetoception for humans and geomagnetic manipulation of virtual objects.
- **Sub- μT magnetosensitive e-skins:** This chapter exhibited a new magnetosensitive e-skin based on the planar Hall effect (PHE), to detect magnetic fields below the μT range illustrated in the previous chapter. A fabrication scheme comprising Py Hall crosses and an in-plane magnetic field configuration was established for measuring the PHE e-skins. Transversal voltage measurements in flat and curved conditions revealed sensitivities of 0.86 V/T and 0.63 V/T which allow detecting magnetic fields of about 200 nT. The reduced sensitivity in the curved case was attributed to the higher levels of 1/f noise probably stemming from mechanical vibrations in the contacts. Dynamic bending tests to a 1 mm bending radius for 200 cycles revealed only a slight voltage variation, associated with the changing contact geometry during the measurements. Finally, two experiments illustrating the proximity and angular detection capabilities were performed on the PHE e-skins. The first one demonstrated the capability of the e-skins to easily reconstruct the magnetic stray fields (20 μT) produced by current pulses through a copper wire. Such sensitivity could be already applied to magnetofluidic setups¹⁸⁴ to detect magnetic particles at the microfluidic channels. The second experiment, validated the $\sin(2\theta)$ angular detection of PHE e-skins at higher fields (4 mT),

which can be readily used for soft robotics applications.

7.2 Outlook

As seen throughout this thesis, magnetosensitive e-skins could be applied in a wide spectrum of topics where human-machine interfaces or measurement systems are required. However, for them to achieve their full potential, improvements in robustness, communication, powering and circuit integration will need to be addressed. In this section, we explore some possibilities to expand the field of magnetosensitive e-skins beyond the boundaries set by this work.

- **On-site or direct sensory feedback:** Up until now, magnetosensitive e-skins rely on additional electronic interfaces like computer screens to provide feedback to the user. Nevertheless, to be really portable and integrated with the human body, they would require ultrathin displays or actuators to communicate the detected signals to the user. Recent works have demonstrated how to achieve ultrathin photonic skins^{84,237} and actuating circuits,²³⁸ which could readily be combined with magnetosensitive e-skins. Moreover, this feedback could be extended to the biological interfaces of humans like nerves or muscles, as shown in recent works on neural^{45,239} and muscular²⁴⁰ stimulation. If this feat could be accomplished, magnetosensitive e-skins would become a full-fledged "sixth sense".
- **Wireless communication and powering:** The most obvious limitation of the e-skins described in this thesis is the use of wired interfaces for power and read-out, which reduces their autonomy and flexibility. In this respect, two approaches can be adopted for achieving circuit autonomy, respectively, the use of passive or active circuitry. In the first case, using radio frequency (RF) power harvesting units^{77,241,242} coupled with low-power microcontrollers²⁴³ could simultaneously provide energy and communication capabilities to magnetosensitive e-skins. In the second scenario, the use of active circuits would increase the measurement possibilities and transmission range of the system at the cost of increasing the bulkiness and compliance of the circuitry. Due to the low-power nature of magnetic sensors, the first alternative would be the preferred way to go.
- **Integration with flexible active electronics:** Another foreseeable improvement would be to use state-of-the-art flexible active electronics using both organic or inorganic approaches. Organic electronics can provide cheap and scalable circuits which could address low frequency applications. Furthermore, if higher performance is required, inorganic technologies could provide on-site conditioning for the readout signals of magnetosensitive e-skins. This approach has been realized before with IGZO,¹⁸⁶ but it could be extended also to rectifying circuits^{244,245} or basic logic units²⁴⁶ which would enable entirely flexible detection and computing modules.
- **Out-of-plane magnetic sensing:** So far, all the sensors that this thesis explored are sensitive to the in-plane component of the magnetic field. However, achieving a full three-dimensional mapping of the magnetic field would allow

a whole new set of interaction and gesture control possibilities. To achieve this, out-of-plane sensors like Hall effect devices would need to be combined with the current method. Possible routes to this goal would imply the use of thin film semimetal-based Hall effect sensors using Bismuth¹⁶ or graphene.²⁴⁷ Another possible path would be to use geometrical curvature²⁰¹ to enable different detection axes by careful placement of the sensors.

- **Encapsulation layer:** Although the mechanical performance demonstrated by the magnetosensitive e-skins of this work is remarkable, adding a matching encapsulation layer can significantly boost their robustness. This strategy is necessary for commercial or advance prototyping applications where outstanding reliability is a must. Placing a matching encapsulation layer as described in section 2.1.3 locates the sensing layer at the neutral mechanical plane where no mechanical strain is expected. Furthermore, the encapsulation process is also critical to isolate the electrical connections in wet or electrically active environments. Recent studies,²⁴⁸ have provided a possible route based on SiO_2 layers for overcoming this fundamental problem of flexible electronic devices, yet, at the expense of reduced mechanical flexibility. Nevertheless, as magnetosensitive e-skins do not need to be implanted inside the body, they can readily use polymeric encapsulations.

Bibliography

- [1] Shancang Li, Li Da Xu, and Shanshan Zhao. “The internet of things: a survey”. *Information Systems Frontiers* 17 (2), **2015**, pp. 243–259.
- [2] Stuart Russell and Peter Norvig. *Artificial Intelligence: A Modern Approach, Global Edition*. 3rd ed. Addison Wesley, **2016**.
- [3] Jenny Preece, Yvonne Rogers, and Helen Sharp. *Interaction Design: Beyond Human-Computer Interaction*. John Wiley & Sons, **2015**.
- [4] Alan Dix. “Human-Computer Interaction”. *Encyclopedia of Database Systems*. Ed. by LING LIU and M. TAMER ÖZSU. Boston, MA: Springer US, 2009, pp. 1327–1331. URL: https://doi.org/10.1007/978-0-387-39940-9_192.
- [5] Puja Varsani, Ralph Moseley, Simon Jones, Carl James-Reynolds, Eris Chinelato, and Juan Carlos Augusto. “Sensorial Computing”. *New Directions in Third Wave Human-Computer Interaction: Volume 1 - Technologies*. Ed. by Michael Filimowicz and Veronika Tzankova. Human-Computer Interaction Series. Cham: Springer International Publishing, 2018, pp. 265–284. URL: https://doi.org/10.1007/978-3-319-73356-2_15.
- [6] Yuhao Liu, Matt Pharr, and Giovanni Antonio Salvatore. “Lab-on-Skin: A Review of Flexible and Stretchable Electronics for Wearable Health Monitoring”. *ACS Nano* 11 (10), **2017**, pp. 9614–9635.
- [7] Amay J. Bandodkar, Itthipon Jeerapan, and Joseph Wang. “Wearable Chemical Sensors: Present Challenges and Future Prospects”. *ACS Sensors* 1 (5), **2016**, pp. 464–482.
- [8] Takao Someya, Siegfried Bauer, and Martin Kaltenbrunner. “Imperceptible organic electronics”. *MRS Bulletin* 42 (2), **2017**, pp. 124–130.
- [9] A. Nathan, A. Ahnood, M. T. Cole, S. Lee, Y. Suzuki, P. Hiralal, F. Bonaccorso, T. Hasan, L. Garcia-Gancedo, A. Dyadyusha, S. Haque, P. Andrew, S. Hofmann, J. Moultrie, D. Chu, A. J. Flewitt, A. C. Ferrari, M. J. Kelly, J. Robertson, G. A. J. Amaratunga, and W. I. Milne. “Flexible Electronics: The Next Ubiquitous Platform”. *Proceedings of the IEEE* 100 (Special Centennial Issue), **2012**, pp. 1486–1517.
- [10] Mallory L. Hammock, Alex Chortos, Benjamin C.-K. Tee, Jeffrey B.-H. Tok, and Zhenan Bao. “25th Anniversary Article: The Evolution of Electronic Skin (E-Skin): A Brief History, Design Considerations, and Recent Progress”. *Advanced Materials* 25 (42), **2013**, pp. 5997–6038.

-
- [11] D.-H. Kim, N. Lu, R. Ma, Y.-S. Kim, R.-H. Kim, S. Wang, J. Wu, S. M. Won, H. Tao, A. Islam, K. J. Yu, T.-i. Kim, R. Chowdhury, M. Ying, L. Xu, M. Li, H.-J. Chung, H. Keum, M. McCormick, P. Liu, Y.-W. Zhang, F. G. Omenetto, Y. Huang, T. Coleman, and J. A. Rogers. “Epidermal Electronics”. *Science* 333 (6044), **2011**, pp. 838–843.
- [12] Darren J. Lipomi and Zhenan Bao. “Stretchable and ultraflexible organic electronics”. *MRS Bulletin* 42 (02), **2017**, pp. 93–97.
- [13] Suji Choi, Hyunjae Lee, Roozbeh Ghaffari, Taeghwan Hyeon, and Dae-Hyeong Kim. “Recent Advances in Flexible and Stretchable Bio-Electronic Devices Integrated with Nanomaterials”. *Advanced Materials* 28 (22), **2016**, pp. 4203–4218.
- [14] Seung-Kyun Kang, Jahyun Koo, Yoon Kyeong Lee, and John A. Rogers. “Advanced Materials and Devices for Bioresorbable Electronics”. *Accounts of Chemical Research*, **2018**.
- [15] Yaping Zang, Fengjiao Zhang, Chong-an Di, and Daoben Zhu. “Advances of flexible pressure sensors toward artificial intelligence and health care applications”. *Materials Horizons* 2 (2), **2015**, pp. 140–156.
- [16] Michael Melzer, Jens Ingolf Mönch, Denys Makarov, Yevhen Zabala, Gilbert Santiago Cañón Bermúdez, Daniil Karnaushenko, Stefan Baunack, Falk Bahr, Chenglin Yan, Martin Kaltenbrunner, and Oliver G. Schmidt. “Wearable Magnetic Field Sensors for Flexible Electronics”. *Advanced Materials* 27 (7), **2015**, pp. 1274–1280.
- [17] Michael Melzer, Martin Kaltenbrunner, Denys Makarov, Dmitriy Karnaushenko, Daniil Karnaushenko, Tsuyoshi Sekitani, Takao Someya, and Oliver G. Schmidt. “Imperceptible magnetoelectronics”. *Nature Communications* 6 (1), **2015**.
- [18] Denys Makarov, Michael Melzer, Daniil Karnaushenko, and Oliver G. Schmidt. “Shapeable magnetoelectronics”. *Applied Physics Reviews* 3 (1), **2016**, p. 011101.
- [19] Robin Baker. *Human Navigation and Magnetoreception: 30th Anniversary Edition*. Google-Books-ID: qAM7DwAAQBAJ. Hard Nut Books Ltd, **2017**.
- [20] Wolfgang Wiltschko and Roswitha Wiltschko. “Magnetic orientation and magnetoreception in birds and other animals”. *Journal of Comparative Physiology A* 191 (8), **2005**, pp. 675–693.
- [21] Le-Qing Wu and J. David Dickman. “Neural Correlates of a Magnetic Sense”. *Science* 336 (6084), **2012**, pp. 1054–1057.
- [22] Henrik Mouritsen. “Long-distance navigation and magnetoreception in migratory animals”. *Nature* 558 (7708), **2018**, p. 50.
- [23] Eric Hand. “What and where are the body’s magnetometers?” *Science* 352 (6293), **2016**, pp. 1510–1511.
- [24] R. Bansal. “The Sixth Sense? [Microwave Surfing]”. *IEEE Microwave Magazine* 18 (4), **2017**, pp. 16–18.
- [25] Daniel-Robert Chebat, Shachar Maidenbaum, and Amir Amedi. “Navigation Using Sensory Substitution in Real and Virtual Mazes”. *PLOS ONE* 10 (6), **2015**, e0126307.

- [26] Paul Bach-y-Rita and Stephen W. Kercel. “Sensory substitution and the human–machine interface”. *Trends in Cognitive Sciences* 7 (12), **2003**, pp. 541–546.
- [27] Yvette Hatwell, Arlette Streri, and Edouard Gentaz. *Touching for Knowing: Cognitive psychology of haptic manual perception*. John Benjamins Publishing, **2003**.
- [28] Daniel-Robert Chebat, Vanessa Harrar, Ron Kupers, Shachar Maidenbaum, Amir Amedi, and Maurice Ptito. “Sensory Substitution and the Neural Correlates of Navigation in Blindness”. *Mobility of Visually Impaired People: Fundamentals and ICT Assistive Technologies*. Ed. by Edwige Pissaloux and Ramiro Velazquez. Cham: Springer International Publishing, 2018, pp. 167–200. URL: https://doi.org/10.1007/978-3-319-54446-5_6.
- [29] Saskia K. Nagel, Christine Carl, Tobias Kringe, Robert Märtin, and Peter König. “Beyond sensory substitution—learning the sixth sense”. *Journal of Neural Engineering* 2 (4), **2005**, R13–R26.
- [30] S. Levy-Tzedek, S. Maidenbaum, A. Amedi, and J. Lackner. “Aging and Sensory Substitution in a Virtual Navigation Task”. *PLOS ONE* 11 (3), **2016**, e0151593.
- [31] Carol Stock Kranowitz. *The Out-of-sync Child: Recognizing and Coping with Sensory Processing Disorder*. Google-Books-ID: 3gtL9XaZ8GwC. Penguin, **2005**.
- [32] Roianne R. Ahn, Lucy Jane Miller, Sharon Milberger, and Daniel N. McIntosh. “Prevalence of parents’ perceptions of sensory processing disorders among kindergarten children”. *American Journal of Occupational Therapy* 58 (3), **2004**, pp. 287–293.
- [33] STAR Institute for Sensory Processing Disorder. *About SPD*. **2018**. URL: <https://www.spdstar.org/basic/about-spd>.
- [34] Great Kids Place. *Great Kids Place in Rockaway, NJ*. **2019**. URL: <https://greatkidsplace.com/>.
- [35] Sensebridge - making the invisible visible » North Paw. *Sensebridge - making the invisible visible » North Paw*. **2009**. URL: <https://sensebridge.net/projects/northpaw/>.
- [36] Smithsonian. *This Artificial Sixth Sense Helps Humans Orient Themselves in the World*. **2017**. URL: <https://www.smithsonianmag.com/innovation/artificial-sixth-sense-helps-humans-orient-themselves-world-180961822/>.
- [37] Robert Herbert, Jong-Hoon Kim, Yun Soung Kim, Hye Moon Lee, and Woon-Hong Yeo. “Soft Material-Enabled, Flexible Hybrid Electronics for Medicine, Healthcare, and Human-Machine Interfaces”. *Materials* 11 (2), **2018**, p. 187.
- [38] Jae-Woong Jeong, Woon-Hong Yeo, Aadeel Akhtar, James J. S. Norton, Young-Jin Kwack, Shuo Li, Sung-Young Jung, Yewang Su, Woosik Lee, Jing Xia, Huanyu Cheng, Yonggang Huang, Woon-Seop Choi, Timothy Bretl, and John A. Rogers. “Materials and Optimized Designs for Human-Machine Interfaces Via Epidermal Electronics”. *Advanced Materials* 25 (47), **2013**, pp. 6839–6846.

- [39] Sungmook Jung, Ji Hoon Kim, Jaemin Kim, Suji Choi, Jongsu Lee, Inhyuk Park, Taeghwan Hyeon, and Dae-Hyeong Kim. “Reverse-Micelle-Induced Porous Pressure-Sensitive Rubber for Wearable Human-Machine Interfaces”. *Advanced Materials* 26 (28), **2014**, pp. 4825–4830.
- [40] Gilbert Santiago Cañón Bermúdez, Dmitriy D. Karnaushenko, Daniil Karnaushenko, Ana Lebanov, Lothar Bischoff, Martin Kaltenbrunner, Jürgen Fassbender, Oliver G. Schmidt, and Denys Makarov. “Magnetosensitive e-skins with directional perception for augmented reality”. *Science Advances* 4 (1), **2018**, eaao2623.
- [41] Gilbert Santiago Cañón Bermúdez, Hagen Fuchs, Lothar Bischoff, Jürgen Fassbender, and Denys Makarov. “Electronic-skin compasses for geomagnetic field-driven artificial magnetoreception and interactive electronics”. *Nature Electronics* 1 (11), **2018**, p. 589.
- [42] Pablo Nicolás Granell, Guoliang Wang, Gilbert Santiago Cañón Bermudez, Tobias Kosub, Federico Golmar, Laura Steren, Jürgen Fassbender, and Denys Makarov. “Highly compliant planar Hall effect sensor with sub 200 nT sensitivity”. *npj Flexible Electronics* 3 (1), **2019**, p. 3.
- [43] John Bardeen and Walter Houser Brattain. “Physical principles involved in transistor action”. *Physical Review* 75 (8), **1949**, p. 1208.
- [44] Siegfried Bauer. “Flexible electronics: Sophisticated skin”. *Nature Materials* 12 (10), **2013**, pp. 871–872.
- [45] Sung Il Park, Daniel S. Brenner, Gunchul Shin, Clinton D. Morgan, Bryan A. Copits, Ha Uk Chung, Melanie Y. Pullen, Kyung Nim Noh, Steve Davidson, Soong Ju Oh, Jangyeol Yoon, Kyung-In Jang, Vijay K. Samineni, Megan Norman, Jose G. Grajales-Reyes, Sherri K. Vogt, Saranya S. Sundaram, Kellie M. Wilson, Jeong Sook Ha, Renxiao Xu, Taisong Pan, Tae-il Kim, Yonggang Huang, Michael C. Montana, Judith P. Golden, Michael R. Bruchas, Robert W. Gereau Iv, and John A. Rogers. “Soft, stretchable, fully implantable miniaturized optoelectronic systems for wireless optogenetics”. *Nature Biotechnology* 33 (12), **2015**, pp. 1280–1286.
- [46] Wei Zeng, Lin Shu, Qiao Li, Song Chen, Fei Wang, and Xiao-Ming Tao. “Fiber-Based Wearable Electronics: A Review of Materials, Fabrication, Devices, and Applications”. *Advanced Materials* 26 (31), **2014**, pp. 5310–5336.
- [47] Matteo Stoppa and Alessandro Chiolerio. “Wearable Electronics and Smart Textiles: A Critical Review”. *Sensors* 14 (7), **2014**, pp. 11957–11992.
- [48] Morteza Amjadi, Ki-Uk Kyung, Inkyu Park, and Metin Sitti. “Stretchable, Skin-Mountable, and Wearable Strain Sensors and Their Potential Applications: A Review”. *Advanced Functional Materials* 26 (11), **2016**, pp. 1678–1698.
- [49] Ducas Charles. “Electrical apparatus and method of manufacturing the same”. US1563731A. **1925**.
- [50] Lilienfeld Julius Edgar. “Device for controlling electric current”. US1900018A. **1933**.
- [51] Oskar Heil. “Improvements in or relating to electrical amplifiers and other control arrangements and devices”. GB439457A. **1935**.

- [52] P. K. Weimer. “The TFT A New Thin-Film Transistor”. *Proceedings of the IRE* 50 (6), **1962**, pp. 1462–1469.
- [53] Peter Brody and Derrick Page. “Flexible thin-film transistors stretch performance, shrink cost(Thin film transistors fabrication from flexible substrates, discussing heat conductivity, properties and costs)”. *Electronics* 41, **1968**, pp. 100–103.
- [54] T. P. Brody. “The thin film transistor—A late flowering bloom”. *IEEE Transactions on Electron Devices* 31 (11), **1984**, pp. 1614–1628.
- [55] K. A. Ray. “Flexible Solar Cell Arrays for Increased Space Power”. *IEEE Transactions on Aerospace and Electronic Systems* AES-3 (1), **1967**, pp. 107–115.
- [56] Harve Bennet. *The Six Million Dollar Man*. American Broadcasting Company. **1974**.
- [57] Irvin Kershner. *Star Wars Episode V: The Empire Strikes Back*. **1980**.
- [58] James Cameron. *The Terminator*. **1984**.
- [59] Frank W Clippinger. “A Sensory Feedback System for an Upper-Limb Amputation Prosthesis”. *Bulletin of Prosthetics Research*, **1974**, p. 12.
- [60] Vladimir J. Lumelsky. *Sensing, Intelligence, Motion: How Robots and Humans Move in an Unstructured World*. Google-Books-ID: mAEoB2uRLcAC. John Wiley & Sons, **2005**.
- [61] K. W. Johnson, J. J. Mastrototaro, D. C. Howey, R. L. Brunelle, P. L. Burden-Brady, N. A. Bryan, C. C. Andrew, H. M. Rowe, D. J. Allen, B. W. Noffke, W. C. McMahan, R. J. Morff, D. Lipson, and R. S. Nevin. “In vivo evaluation of an electroenzymatic glucose sensor implanted in subcutaneous tissue”. *Biosensors and Bioelectronics* 7 (10), **1992**, pp. 709–714.
- [62] Ernö Lindner, Vasile V. Cosofret, Stefan Ufer, Richard P. Buck, Robert P. Kusy, R. Bruce Ash, and H. Troy Nagle. “Flexible (Kapton-based) microsensor arrays of high stability for cardiovascular applications”. *Journal of the Chemical Society, Faraday Transactions* 89 (2), **1993**, pp. 361–367.
- [63] M. Uesaka, K. Hakuta, K. Miya, K. Aoki, and A. Takahashi. “Eddy-current testing by flexible microloop magnetic sensor array”. *IEEE Transactions on Magnetics* 34 (4), **1998**, pp. 2287–2297.
- [64] D. Um, B. Stankovic, K. Giles, T. Hammond, and V. Lumelsky. “A modularized sensitive skin for motion planning in uncertain environments”. *Proceedings. 1998 IEEE International Conference on Robotics and Automation (Cat. No.98CH36146)*. Vol. 1. **1998**, 7–12 vol.1.
- [65] E. Cheung and V. Lumelsky. “Motion planning for a whole-sensitive robot arm manipulator”. , *IEEE International Conference on Robotics and Automation Proceedings*. **1990**, 344–349 vol.1.
- [66] Gwo-Bin Lee, F. K. Jiang, T. Tsao, Y. C. Tai, and C. M. Ho. “Macro aerodynamic devices controlled by micro systems”. *1997 IEEE Aerospace Conference*. Vol. 3. **1997**, 255–263 vol.3.

- [67] Z. Suo, E. Y. Ma, H. Gleskova, and S. Wagner. “Mechanics of rollable and foldable film-on-foil electronics”. *Applied Physics Letters* 74 (8), **1999**, pp. 1177–1179.
- [68] Karl Ziemelis. “Putting it on plastic”. *Nature* 393 (6686), **1998**, pp. 619–620.
- [69] V. J. Lumelsky, M. S. Shur, and S. Wagner. “Sensitive skin”. *IEEE Sensors Journal* 1 (1), **2001**, pp. 41–51.
- [70] Sigurd Wagner, Stéphanie P. Lacour, Joyelle Jones, Pai-hui I. Hsu, James C. Sturm, Teng Li, and Zhigang Suo. “Electronic skin: architecture and components”. *Physica E: Low-dimensional Systems and Nanostructures*. Proceedings of the 13th International Winterschool on New Developments in Solid State Physics - Low-Dimensional Systems 25 (2), **2004**, pp. 326–334.
- [71] T. Someya, Y. Kato, T. Sekitani, S. Iba, Y. Noguchi, Y. Murase, H. Kawaguchi, and T. Sakurai. “Conformable, flexible, large-area networks of pressure and thermal sensors with organic transistor active matrixes”. *Proceedings of the National Academy of Sciences* 102 (35), **2005**, pp. 12321–12325.
- [72] Vikram C. Sundar, Jana Zaumseil, Vitaly Podzorov, Etienne Menard, Robert L. Willett, Takao Someya, Michael E. Gershenson, and John A. Rogers. “Elastomeric Transistor Stamps: Reversible Probing of Charge Transport in Organic Crystals”. *Science* 303 (5664), **2004**, pp. 1644–1646.
- [73] Dahl-Young Khang, Hanqing Jiang, Young Huang, and John A. Rogers. “A Stretchable Form of Single-Crystal Silicon for High-Performance Electronics on Rubber Substrates”. *Science* 311 (5758), **2006**, pp. 208–212.
- [74] Jong-Hyun Ahn, Hoon-Sik Kim, Keon Jae Lee, Seokwoo Jeon, Seong Jun Kang, Yugang Sun, Ralph G. Nuzzo, and John A. Rogers. “Heterogeneous Three-Dimensional Electronics by Use of Printed Semiconductor Nanomaterials”. *Science* 314 (5806), **2006**, pp. 1754–1757.
- [75] Heung Cho Ko, Mark P. Stoykovich, Jizhou Song, Viktor Malyarchuk, Won Mook Choi, Chang-Jae Yu, Joseph B. Geddes Iii, Jianliang Xiao, Shuodao Wang, Yonggang Huang, and John A. Rogers. “A hemispherical electronic eye camera based on compressible silicon optoelectronics”. *Nature* 454 (7205), **2008**, pp. 748–753.
- [76] Dae-Hyeong Kim, Nanshu Lu, Roozbeh Ghaffari, Yun-Soung Kim, Stephen P. Lee, Lizhi Xu, Jian Wu, Rak-Hwan Kim, Jizhou Song, Zhuangjian Liu, Jonathan Viventi, Bassel de Graff, Brian Elolampi, Moussa Mansour, Marvin J. Slepian, Sukwon Hwang, Joshua D. Moss, Sang-Min Won, Younggang Huang, Brian Litt, and John A. Rogers. “Materials for multifunctional balloon catheters with capabilities in cardiac electrophysiological mapping and ablation therapy”. *Nature Materials* 10 (4), **2011**, pp. 316–323.
- [77] Xian Huang, Yuhao Liu, Gil Woo Kong, Jung Hun Seo, Yinji Ma, Kyung-In Jang, Jonathan A. Fan, Shimin Mao, Qiwen Chen, Daizhen Li, Hank Liu, Chuxuan Wang, Dwipayana Patnaik, Limei Tian, Giovanni A. Salvatore, Xue Feng, Zhenqiang Ma, Yonggang Huang, and John A. Rogers. “Epidermal radio frequency electronics for wireless power transfer”. *Microsystems & Nanoengineering* 2 (1), **2016**.

- [78] Federico Carpi, Siegfried Bauer, and Danilo De Rossi. “Stretching Dielectric Elastomer Performance”. *Science* 330 (6012), **2010**, pp. 1759–1761.
- [79] Christoph Keplinger, Tiefeng Li, Richard Baumgartner, Zhigang Suo, and Siegfried Bauer. “Harnessing snap-through instability in soft dielectrics to achieve giant voltage-triggered deformation”. *Soft Matter* 8 (2), **2011**, pp. 285–288.
- [80] Siegfried Bauer, Reimund Gerhard-Multhaupt, and G. M. Sessler. “Ferroelectrets : soft electroactive foams for transducers”, **2004**.
- [81] Martin Kaltenbrunner, Matthew S. White, Eric D. Głowacki, Tsuyoshi Sekitani, Takao Someya, Niyazi Serdar Sariciftci, and Siegfried Bauer. “Ultrathin and lightweight organic solar cells with high flexibility”. *Nature Communications* 3, **2012**, p. 770.
- [82] Martin Kaltenbrunner, Tsuyoshi Sekitani, Jonathan Reeder, Tomoyuki Yokota, Kazunori Kuribara, Takeyoshi Tokuhara, Michael Drack, Reinhard Schwödau, Ingrid Graz, Simona Bauer-Gogonea, Siegfried Bauer, and Takao Someya. “An ultra-lightweight design for imperceptible plastic electronics”. *Nature* 499 (7459), **2013**, pp. 458–463.
- [83] Matthew S. White, Martin Kaltenbrunner, Eric D. Głowacki, Kateryna Gutnichenko, Gerald Kettlgruber, Ingrid Graz, Safae Aazou, Christoph Ulbricht, Daniel A. M. Egbe, Matei C. Miron, Zoltan Major, Markus C. Scharber, Tsuyoshi Sekitani, Takao Someya, Siegfried Bauer, and Niyazi Serdar Sariciftci. “Ultrathin, highly flexible and stretchable PLEDs”. *Nature Photonics* 7 (10), **2013**, pp. 811–816.
- [84] Tomoyuki Yokota, Peter Zalar, Martin Kaltenbrunner, Hiroaki Jinno, Naoji Matsuhisa, Hiroki Kitanosako, Yutaro Tachibana, Wakako Yukita, Mari Koizumi, and Takao Someya. “Ultraflexible organic photonic skin”. *Science Advances* 2 (4), **2016**, e1501856.
- [85] Tsuyoshi Sekitani, Tomoyuki Yokota, Kazunori Kuribara, Martin Kaltenbrunner, Takanori Fukushima, Yusuke Inoue, Masaki Sekino, Takashi Isoyama, Yusuke Abe, Hiroshi Onodera, and Takao Someya. “Ultraflexible organic amplifier with biocompatible gel electrodes”. *Nature Communications* 7, **2016**, p. 11425.
- [86] Robert A. Nawrocki, Naoji Matsuhisa, Tomoyuki Yokota, and Takao Someya. “300-nm Imperceptible, Ultraflexible, and Biocompatible e-Skin Fit with Tactile Sensors and Organic Transistors”. *Advanced Electronic Materials* 2 (4), **2016**, p. 1500452.
- [87] Martin Kaltenbrunner, Getachew Adam, Eric Daniel Głowacki, Michael Drack, Reinhard Schwödau, Lucia Leonat, Dogukan Hazar Apaydin, Heiko Groiss, Markus Clark Scharber, Matthew Schuette White, Niyazi Serdar Sariciftci, and Siegfried Bauer. “Flexible high power-per-weight perovskite solar cells with chromium oxide–metal contacts for improved stability in air”. *Nature Materials* 14 (10), **2015**, pp. 1032–1039.

- [88] Suk-Won Hwang, Hu Tao, Dae-Hyeong Kim, Huanyu Cheng, Jun-Kyul Song, Elliott Rill, Mark A. Brenckle, Bruce Panilaitis, Sang Min Won, Yun-Soung Kim, Young Min Song, Ki Jun Yu, Abid Ameen, Rui Li, Yewang Su, Miaomiao Yang, David L. Kaplan, Mitchell R. Zakin, Marvin J. Slepian, Yonggang Huang, Fiorenzo G. Omenetto, and John A. Rogers. “A Physically Transient Form of Silicon Electronics”. *Science* 337 (6102), **2012**, pp. 1640–1644.
- [89] Ki Jun Yu, Duygu Kuzum, Suk-Won Hwang, Bong Hoon Kim, Halvor Juul, Nam Heon Kim, Sang Min Won, Ken Chiang, Michael Trumpis, Andrew G. Richardson, Huanyu Cheng, Hui Fang, Marissa Thompson, Hank Bink, Delia Talos, Kyung Jin Seo, Hee Nam Lee, Seung-Kyun Kang, Jae-Hwan Kim, Jung Yup Lee, Younggang Huang, Frances E. Jensen, Marc A. Dichter, Timothy H. Lucas, Jonathan Viventi, Brian Litt, and John A. Rogers. “Bioresorbable silicon electronics for transient spatiotemporal mapping of electrical activity from the cerebral cortex”. *Nature Materials* 15 (7), **2016**, pp. 782–791.
- [90] Ting Lei, Ming Guan, Jia Liu, Hung-Cheng Lin, Raphael Pfattner, Leo Shaw, Allister F. McGuire, Tsung-Ching Huang, Leilai Shao, Kwang-Ting Cheng, Jeffrey B.-H. Tok, and Zhenan Bao. “Biocompatible and totally disintegrable semiconducting polymer for ultrathin and ultralightweight transient electronics”. *Proceedings of the National Academy of Sciences* 114 (20), **2017**, pp. 5107–5112.
- [91] Hsin-Liu (Cindy) Kao, Miren Bamforth, David Kim, and Chris Schmandt. “Skinmorph: Texture-tunable On-skin Interface Through Thin, Programmable Gel”. *Proceedings of the 2018 ACM International Symposium on Wearable Computers*. ISWC ’18. New York, NY, USA: ACM, **2018**, pp. 196–203.
- [92] Hsin-Liu (Cindy) Kao, Christian Holz, Asta Roseway, Andres Calvo, and Chris Schmandt. “DuoSkin: Rapidly Prototyping On-skin User Interfaces Using Skin-friendly Materials”. *Proceedings of the 2016 ACM International Symposium on Wearable Computers*. ISWC ’16. New York, NY, USA: ACM, **2016**, pp. 16–23.
- [93] Hsin-Liu (Cindy) Kao. “Hybrid Body Craft”. *Proceedings of the 2017 ACM Conference Companion Publication on Designing Interactive Systems*. DIS ’17 Companion. New York, NY, USA: ACM, **2017**, pp. 391–392.
- [94] T. Someya, T. Sekitani, S. Iba, Y. Kato, H. Kawaguchi, and T. Sakurai. “A large-area, flexible pressure sensor matrix with organic field-effect transistors for artificial skin applications”. *Proceedings of the National Academy of Sciences* 101 (27), **2004**, pp. 9966–9970.
- [95] Sungwon Lee, Amir Reuveny, Jonathan Reeder, Sunghoon Lee, Hanbit Jin, Qihan Liu, Tomoyuki Yokota, Tsuyoshi Sekitani, Takashi Isoyama, Yusuke Abe, Zhigang Suo, and Takao Someya. “A transparent bending-insensitive pressure sensor”. *Nature Nanotechnology* 11 (5), **2016**, pp. 472–478.
- [96] Akihito Miyamoto, Sungwon Lee, Nawalage Florence Cooray, Sunghoon Lee, Mami Mori, Naoji Matsuhisa, Hanbit Jin, Leona Yoda, Tomoyuki Yokota, Akira Itoh, Masaki Sekino, Hiroshi Kawasaki, Tamotsu Ebihara, Masayuki Amagai, and Takao Someya. “Inflammation-free, gas-permeable, lightweight, stretchable on-skin electronics with nanomeshes”. *Nature Nanotechnology* 12 (9), **2017**, pp. 907–913.

- [97] Hitoshi Araki, Jeonghyun Kim, Shaoning Zhang, Anthony Banks, Kaitlyn E. Crawford, Xing Sheng, Philipp Gutruf, Yunzhou Shi, Rafal M. Pielak, and John A. Rogers. “Materials and Device Designs for an Epidermal UV Colorimetric Dosimeter with Near Field Communication Capabilities”. *Advanced Functional Materials* 27 (2), **2017**, p. 1604465.
- [98] H. Gleskovas, S. Wagner, and Z. Suo. “Rugged a-Si:H TFTs on Plastic Substrates”. *MRS Online Proceedings Library Archive* 557, **1999**.
- [99] Bob McGinty. *Beam Bending*. **2013**. URL: <http://www.continuummechanics.org/beambending.html>.
- [100] Kurt Gramoll. *Mechanics eBook: Bending Strain and Stress*. **2008**. URL: http://www.ecourses.ou.edu/cgi-bin/eBook.cgi?doc=&topic=me&chap_sec=04.1&page=theory.
- [101] Michael J Caruso, Tamara Bratland, Dr Carl H Smith, and Robert Schneider. “A New Perspective on Magnetic Field Sensing”. *Honeywell Inc.* **1998**, p. 19.
- [102] J.E. Lenz. “A review of magnetic sensors”. *Proceedings of the IEEE* 78 (6), **1990**, pp. 973–989.
- [103] D. Robbes. “Highly sensitive magnetometers—a review”. *Sensors and Actuators A: Physical* 129 (1-2), **2006**, pp. 86–93.
- [104] Thomson William. “XIX. On the electro-dynamic qualities of metals:—Effects of magnetization on the electric conductivity of nickel and of iron”. *Proceedings of the Royal Society of London* 8, **1857**, pp. 546–550.
- [105] G. Giuliani. “A general law for electromagnetic induction”. *EPL (Europhysics Letters)* 81 (6), **2008**, p. 60002.
- [106] H. Hauser, G. Stangl, W. Fallman, R. Chabicovsky, and K. Riedling. “Magnetoresistive Sensors”. Vienna, **2000**.
- [107] Uwe Dibern. “Magnetoresistive Sensors”. *Sensors*. John Wiley & Sons, Ltd, 2008, pp. 341–380. URL: <https://onlinelibrary.wiley.com/doi/abs/10.1002/9783527620166.ch9>.
- [108] Janice Nickel. “Magnetoresistance Overview”. *Hewlett-Packard Laboratories, Technical Publications Department*, **1995**, p. 12.
- [109] Charles Wheatstone. “An Account of Several New Instruments and Processes for Determining the Constants of a Voltaic Circuit. [Abstract]”. *Abstracts of the Papers Printed in the Philosophical Transactions of the Royal Society of London* 4, **1837**, pp. 469–471.
- [110] S. Ekelof. “The genesis of the Wheatstone bridge”. *Engineering Science & Education Journal* 10 (1), **2001**, pp. 37–40.
- [111] Karl Hoffmann. *Applying the wheatstone bridge circuit*. HBM Germany, **1974**.
- [112] Andrew Johnson. “Spin Valve Systems for Angle Sensor Applications”. phd. Darmstadt: Technische Universität, 2004. URL: <http://elib.tu-darmstadt.de/diss/000511>.

- [113] C. C. Finlay, S. Maus, C. D. Beggan, T. N. Bondar, A. Chambodut, T. A. Chernova, A. Chulliat, V. P. Golovkov, B. Hamilton, M. Hamoudi, R. Holme, G. Hulot, W. Kuang, B. Langlais, V. Lesur, F. J. Lowes, H. Lühr, S. Macmillan, M. Manda, S. McLean, C. Manoj, M. Menvielle, I. Michaelis, N. Olsen, J. Rauberg, M. Rother, T. J. Sabaka, A. Tangborn, L. Tøffner-Clausen, E. Thébault, A. W. P. Thomson, I. Wardinski, Z. Wei, and T. I. Zvereva. “International Geomagnetic Reference Field: the eleventh generation”. *Geophysical Journal International* 183 (3), **2010**, pp. 1216–1230.
- [114] K. Kuijk, W. van Gestel, and F. Gorter. “The barber pole, a linear magnetoresistive head”. *IEEE Transactions on Magnetics* 11 (5), **1975**, pp. 1215–1217.
- [115] Donald O. Smith. “Anisotropy in Permalloy Films”. *Journal of Applied Physics* 30 (4), **1959**, S264–S265.
- [116] B. A. Belyaev, V. P. Kononov, and S. G. Ovchinnikov. “Anisotropy characteristics in a Permalloy film induced by a nonuniform magnetic field”. *Physics of the Solid State* 40 (7), **1998**, pp. 1175–1177.
- [117] H. Katada, T. Shimatsu, I. Watanabe, H. Muraoka, Y. Sugita, and Y. Nakamura. “Induced uniaxial magnetic anisotropy field in very thin NiFe and CoZrNb films”. *IEEE Transactions on Magnetics* 36 (5), **2000**, pp. 2905–2908.
- [118] Colman Goldberg and R. E. Davis. “New Galvanomagnetic Effect”. *Physical Review* 94 (5), **1954**, pp. 1121–1125.
- [119] A. D. Henriksen, B. T. Dalslet, D. H. Skieller, K. H. Lee, F. Okkels, and M. F. Hansen. “Planar Hall effect bridge magnetic field sensors”. *Applied Physics Letters* 97 (1), **2010**, p. 013507.
- [120] Forrest G. West. “Rotating-Field Technique for Galvanomagnetic Measurements”. *Journal of Applied Physics* 34 (4), **1963**, pp. 1171–1173.
- [121] François Moutaigne, Alain Schuhl, Frédéric Nguyen Van Dau, and Armando Encinas. “Development of magnetoresistive sensors based on planar Hall effect for applications to microcompass”. *Sensors and Actuators A: Physical* 81 (1), **2000**, pp. 324–327.
- [122] M. N. Baibich, J. M. Broto, A. Fert, F. Nguyen Van Dau, F. Petroff, P. Etienne, G. Creuzet, A. Friederich, and J. Chazelas. “Giant Magnetoresistance of (001)Fe/(001)Cr Magnetic Superlattices”. *Physical Review Letters* 61 (21), **1988**, pp. 2472–2475.
- [123] G. Binasch, P. Grünberg, F. Saurenbach, and W. Zinn. “Enhanced magnetoresistance in layered magnetic structures with antiferromagnetic interlayer exchange”. *Physical Review B* 39 (7), **1989**, pp. 4828–4830.
- [124] Eric E. Fullerton, M. J. Conover, J. E. Mattson, C. H. Sowers, and S. D. Bader. “150% magnetoresistance in sputtered Fe/Cr(100) superlattices”. *Applied Physics Letters* 63 (12), **1993**, pp. 1699–1701.
- [125] P. Grünberg, R. Schreiber, Y. Pang, M. B. Brodsky, and H. Sowers. “Layered Magnetic Structures: Evidence for Antiferromagnetic Coupling of Fe Layers across Cr Interlayers”. *Physical Review Letters* 57 (19), **1986**, pp. 2442–2445.

- [126] S. S. P. Parkin, N. More, and K. P. Roche. “Oscillations in exchange coupling and magnetoresistance in metallic superlattice structures: Co/Ru, Co/Cr, and Fe/Cr”. *Physical Review Letters* 64 (19), **1990**, pp. 2304–2307.
- [127] S. S. P. Parkin, Z. G. Li, and David J. Smith. “Giant magnetoresistance in antiferromagnetic Co/Cu multilayers”. *Applied Physics Letters* 58 (23), **1991**, pp. 2710–2712.
- [128] M. A. Ruderman and C. Kittel. “Indirect Exchange Coupling of Nuclear Magnetic Moments by Conduction Electrons”. *Physical Review* 96 (1), **1954**, pp. 99–102.
- [129] P. Bruno. “Interlayer exchange coupling: a unified physical picture”. *Journal of Magnetism and Magnetic Materials*. Proceedings of the International Symposium on Magnetic Ultrathin Films, Multilayers and Surfaces 121 (1), **1993**, pp. 248–252.
- [130] J Barnaś, A Fuss, R. E Camley, U Walz, P Grünberg, and W Zinn. “Layered magnetic structures: magnetoresistance due to antiparallel alignment”. *Vacuum*. Selected proceedings of the 11th international vacuum congress (IVC-11) 7th international conference on solid surfaces (ICSS-7) 41 (4), **1990**, pp. 1241–1243.
- [131] C. Dupas, P. Beauvillain, C. Chappert, J. P. Renard, F. Trigui, P. Veillet, E. Vélú, and D. Renard. “Very large magnetoresistance effects induced by antiparallel magnetization in two ultrathin cobalt films”. *Journal of Applied Physics* 67 (9), **1990**, pp. 5680–5682.
- [132] Mott Nevill Francis. “The resistance and thermoelectric properties of the transition metals”. *Proceedings of the Royal Society of London. Series A - Mathematical and Physical Sciences* 156 (888), **1936**, pp. 368–382.
- [133] B. Dieny, V. S. Speriosu, S. S. P. Parkin, B. A. Gurney, D. R. Wilhoit, and D. Mauri. “Giant magnetoresistive in soft ferromagnetic multilayers”. *Physical Review B* 43 (1), **1991**, pp. 1297–1300.
- [134] W. H. Meiklejohn and C. P. Bean. “New Magnetic Anisotropy”. *Physical Review* 102 (5), **1956**, pp. 1413–1414.
- [135] Th. G. S. M. Rijks, W. J. M. de Jonge, W. Folkerts, J. C. S. Kools, and R. Coehoorn. “Magnetoresistance in Ni₈₀Fe₂₀/Cu/Ni₈₀Fe₂₀/Fe₅₀ Mn₅₀ spin valves with low coercivity and ultrahigh sensitivity”. *Applied Phys. Letters* 65 (7), **1994**, pp. 916–918.
- [136] J. C. S. Kools. “Exchange-biased spin-valves for magnetic storage”. *IEEE Transactions on Magnetics* 32 (4), **1996**, pp. 3165–3184.
- [137] A. Chaiken, P. Lubitz, J. J. Krebs, G. A. Prinz, and M. Z. Harford. “Low-field spin-valve magnetoresistance in Fe-Cu-Co sandwiches”. *Applied Physics Letters* 59 (2), **1991**, pp. 240–242.
- [138] B. Dieny. “Giant magnetoresistance in spin-valve multilayers”. *Journal of Magnetism and Magnetic Materials* 136 (3), **1994**, pp. 335–359.
- [139] Stuart K. Card. *The psychology of human-computer interaction*. CRC Press, **2017**.

- [140] Brad A. Myers. “A brief history of human-computer interaction technology”. *interactions* 5 (2), **1998**, pp. 44–54.
- [141] Ivan E. Sutherland. “Sketch Pad a Man-machine Graphical Communication System”. *Proceedings of the SHARE Design Automation Workshop*. DAC '64. New York, NY, USA: ACM, **1964**, pp. 6.329–6.346.
- [142] W. K. English, D. C. Engelbart, and M. L. Berman. “Display-Selection Techniques for Text Manipulation”. *IEEE Transactions on Human Factors in Electronics* HFE-8 (1), **1967**, pp. 5–15.
- [143] Douglas C. Engelbart and William K. English. “A Research Center for Augmenting Human Intellect”. *Proceedings of the December 9-11, 1968, Fall Joint Computer Conference, Part I*. AFIPS '68 (Fall, part I). New York, NY, USA: ACM, **1968**, pp. 395–410.
- [144] William M. Newman. “A System for Interactive Graphical Programming”. *Proceedings of the April 30–May 2, 1968, Spring Joint Computer Conference*. AFIPS '68 (Spring). New York, NY, USA: ACM, **1968**, pp. 47–54.
- [145] A. Kay and A. Goldberg. “Personal Dynamic Media”. *Computer* 10 (3), **1977**, pp. 31–41.
- [146] Shneiderman. “Direct Manipulation: A Step Beyond Programming Languages”. *Computer* 16 (8), **1983**, pp. 57–69.
- [147] Ivan E. Sutherland. “A head-mounted three dimensional display”. *Proceedings of the December 9-11, 1968, fall joint computer conference, part I on - AFIPS '68 (Fall, part I)*. San Francisco, California: ACM Press, **1968**, p. 757.
- [148] Dave Curbow. *DigiBarn: The Xerox Star 8010 (Dandelion)*. **2006**. URL: <http://www.digibarn.com/collections/systems/xerox-8010/>.
- [149] Myron W. Krueger and Stephen Wilson. “VIDEOPPLACE: A Report from the ARTIFICIAL REALITY Laboratory”. *Leonardo* 18 (3), **1985**, pp. 145–151.
- [150] H. Creagh. “Cave Automatic Virtual Environment”. *Proceedings: Electrical Insulation Conference and Electrical Manufacturing and Coil Winding Technology Conference (Cat. No.03CH37480)*. **2003**, pp. 499–504.
- [151] Malcolm R. Davis and Tom O. Ellis. “The RAND tablet: a man-machine graphical communication device”. *Proceedings of the October 27-29, 1964, fall joint computer conference, part I*. ACM, **1964**, pp. 325–331.
- [152] Cyrus Levinthal. “Molecular Model-building by Computer”. *Scientific American* 214 (6), **1966**, pp. 42–53.
- [153] Ivan E. Sutherland. “The ultimate display”. *Multimedia: From Wagner to virtual reality*, **1965**, pp. 506–508.
- [154] D. R. Reddy. “Speech recognition by machine: A review”. *Proceedings of the IEEE* 64 (4), **1976**, pp. 501–531.
- [155] Tomasz Mazuryk and Michael Gervautz. *Virtual Reality - History, Applications, Technology and Future*.
- [156] Lawrence G. Roberts. “The Lincoln WAND”. *Proceedings of the November 7-10, 1966, Fall Joint Computer Conference*. AFIPS '66 (Fall). New York, NY, USA: ACM, **1966**, pp. 223–227.

- [157] Steven Feiner, Blair Macintyre, and Dorée Seligmann. “Knowledge-based Augmented Reality”. *Commun. ACM* 36 (7), **1993**, pp. 53–62.
- [158] Joshua Q. Coburn, Ian Freeman, and John L. Salmon. “A Review of the Capabilities of Current Low-Cost Virtual Reality Technology and Its Potential to Enhance the Design Process”. *Journal of Computing and Information Science in Engineering* 17 (3), **2017**, pp. 031013–031013–15.
- [159] D. Wagner and D. Schmalstieg. “History and Future of Tracking for Mobile Phone Augmented Reality”. *2009 International Symposium on Ubiquitous Virtual Reality*. **2009**, pp. 7–10.
- [160] Dan Saffer. *Designing Gestural Interfaces: Touchscreens and Interactive Devices*. "O’Reilly Media, Inc.", **2008**. URL: <https://books.google.de/books?id=iTsZ5cg7gegC&lpg=PP1&hl=de&pg=PP1#v=onepage&q&f=false>.
- [161] Yuhang Zhao, Cynthia L. Bennett, Hrvoje Benko, Edward Cutrell, Christian Holz, Meredith Ringel Morris, and Mike Sinclair. “Demonstration of Enabling People with Visual Impairments to Navigate Virtual Reality with a Haptic and Auditory Cane Simulation”. *Extended Abstracts of the 2018 CHI Conference on Human Factors in Computing Systems*. CHI EA ’18. New York, NY, USA: ACM, **2018**, D409:1–D409:4.
- [162] Evan Strasnick, Christian Holz, Eyal Ofek, Mike Sinclair, and Hrvoje Benko. “Demonstration of Haptic Links: Bimanual Haptics for Virtual Reality Using Variable Stiffness Actuation”. *Extended Abstracts of the 2018 CHI Conference on Human Factors in Computing Systems*. CHI EA ’18. New York, NY, USA: ACM, **2018**, D106:1–D106:4.
- [163] C. Pacchierotti, S. Sinclair, M. Solazzi, A. Frisoli, V. Hayward, and D. Praticchizzo. “Wearable Haptic Systems for the Fingertip and the Hand: Taxonomy, Review, and Perspectives”. *IEEE Transactions on Haptics* 10 (4), **2017**, pp. 580–600.
- [164] G. Welch and E. Foxlin. “Motion tracking: no silver bullet, but a respectable arsenal”. *IEEE Computer Graphics and Applications* 22 (6), **2002**, pp. 24–38.
- [165] Shyamal Patel, Hyung Park, Paolo Bonato, Leighton Chan, and Mary Rodgers. “A review of wearable sensors and systems with application in rehabilitation”. *Journal of NeuroEngineering and Rehabilitation* 9 (1), **2012**, p. 21.
- [166] K. -N. An, M. C. Jacobsen, L. J. Berglund, and E. Y. S. Chao. “Application of a magnetic tracking device to kinesiological studies”. *Journal of Biomechanics* 21 (7), **1988**, pp. 613–620.
- [167] A. D. Milne, D. G. Chess, J. A. Johnson, and G. J. W. King. “Accuracy of an electromagnetic tracking device: A study of the optimal operating range and metal interference”. *Journal of Biomechanics* 29 (6), **1996**, pp. 791–793.
- [168] Judd S Day, Genevieve A Dumas, and Duncan J Murdoch. “Evaluation of a long-range transmitter for use with a magnetic tracking device in motion analysis”. *Journal of Biomechanics* 31 (10), **1998**, pp. 957–961.
- [169] Huiyu Zhou and Huosheng Hu. “Human motion tracking for rehabilitation - A survey”. *Biomedical Signal Processing and Control* 3 (1), **2008**, pp. 1–18.

- [170] Per Krogh Hansen. “Magnetic motion tracker with transmitter placed on tracked object”. US5744953A. **1998**.
- [171] E. Palermo, S. Rossi, F. Patanè, and P. Cappa. “Experimental evaluation of indoor magnetic distortion effects on gait analysis performed with wearable inertial sensors”. *Physiological Measurement* 35 (3), **2014**, pp. 399–415.
- [172] Elena Bergamini, Gabriele Ligorio, Aurora Summa, Giuseppe Vannozzi, Aurelio Cappozzo, and Angelo Maria Sabatini. “Estimating Orientation Using Magnetic and Inertial Sensors and Different Sensor Fusion Approaches: Accuracy Assessment in Manual and Locomotion Tasks”. *Sensors* 14 (10), **2014**, pp. 18625–18649.
- [173] Weijun Tao, Tao Liu, Rencheng Zheng, and Hutian Feng. “Gait Analysis Using Wearable Sensors”. *Sensors* 12 (2), **2012**, pp. 2255–2283.
- [174] A. M. Franz, T. Haidegger, W. Birkfellner, K. Cleary, T. M. Peters, and L. Maier-Hein. “Electromagnetic Tracking in Medicine—A Review of Technology, Validation, and Applications”. *IEEE Transactions on Medical Imaging* 33 (8), **2014**, pp. 1702–1725.
- [175] Y. Ma, Z. Mao, W. Jia, C. Li, J. Yang, and M. Sun. “Magnetic Hand Tracking for Human-Computer Interface”. *IEEE Transactions on Magnetics* 47 (5), **2011**, pp. 970–973.
- [176] A. Gallagher, Y. Matsuoka, and Wei-Tech Ang. “An efficient real-time human posture tracking algorithm using low-cost inertial and magnetic sensors”. *2004 IEEE/RSJ International Conference on Intelligent Robots and Systems (IROS) (IEEE Cat. No.04CH37566)*. Vol. 3. **2004**, 2967–2972 vol.3.
- [177] S. S. P. Parkin, K. P. Roche, and Takao Suzuki. “Giant Magnetoresistance in Antiferromagnetic Co/Cu Multilayers Grown on Kapton”. *Japanese Journal of Applied Physics* 31 (Part 2, No. 9A), **1992**, pp. L1246–L1249.
- [178] S. S. P. Parkin. “Flexible giant magnetoresistance sensors”. *Applied Physics Letters* 69 (20), **1996**, pp. 3092–3094.
- [179] Yuan-fu Chen, Yongfeng Mei, Rainer Kaltofen, Jens Ingolf Mönch, Joachim Schumann, Jens Freudenberger, Hans-Jörg Klauß, and Oliver G. Schmidt. “Towards Flexible Magnetoelectronics: Buffer-Enhanced and Mechanically Tunable GMR of Co/Cu Multilayers on Plastic Substrates”. *Advanced Materials* 20 (17), **2008**, pp. 3224–3228.
- [180] Michael Melzer, Denys Makarov, Alfredo Calvimontes, Daniil Karnaushenko, Stefan Baunack, Rainer Kaltofen, Yongfeng Mei, and Oliver G. Schmidt. “Stretchable Magnetoelectronics”. *Nano Letters* 11 (6), **2011**, pp. 2522–2526.
- [181] Michael Melzer, Gungun Lin, Denys Makarov, and Oliver G. Schmidt. “Stretchable Spin Valves on Elastomer Membranes by Predetermined Periodic Fracture and Random Wrinkling”. *Advanced Materials* 24 (48), **2012**, pp. 6468–6472.
- [182] Denys Makarov, Daniil Karnaushenko, and Oliver G. Schmidt. “Printable Magnetoelectronics”. *ChemPhysChem* 14 (9), **2013**, pp. 1771–1776.
- [183] Daniil Karnaushenko, Denys Makarov, Chenglin Yan, Robert Streubel, and Oliver G. Schmidt. “Printable Giant Magnetoresistive Devices”. *Advanced Materials* 24 (33), **2012**, pp. 4518–4522.

- [184] Gungun Lin, Denys Makarov, Michael Melzer, Wenping Si, Chenglin Yan, and Oliver G. Schmidt. “A highly flexible and compact magnetoresistive analytic device”. *Lab Chip* 14 (20), **2014**, pp. 4050–4058.
- [185] Michael Melzer, Daniil Karnaushenko, Gungun Lin, Stefan Baunack, Denys Makarov, and Oliver G. Schmidt. “Direct Transfer of Magnetic Sensor Devices to Elastomeric Supports for Stretchable Electronics”. *Advanced Materials* 27 (8), **2015**, pp. 1333–1338.
- [186] Niko Münzenrieder, Daniil Karnaushenko, Luisa Petti, Giuseppe Cantarella, Christian Vogt, Lars Büthe, Dmitriy D. Karnaushenko, Oliver G. Schmidt, Denys Makarov, and Gerhard Tröster. “Entirely Flexible On-Site Conditioned Magnetic Sensorics”. *Advanced Electronic Materials* 2 (8), **2016**, p. 1600188.
- [187] Olaf Suess, Silke Suess, Sven Mularski, Björn Kühn, Thomas Picht, Stefanie Hammersen, Rüdiger Stendel, Mario Brock, and Theodoros Kombos. “Study on the clinical application of pulsed DC magnetic technology for tracking of intraoperative head motion during frameless stereotaxy”. *Head & Face Medicine* 2 (1), **2006**, p. 10.
- [188] *Ascension Technology Corp.* URL: <https://www.ascension-tech.com/>.
- [189] Vincent Linder, Byron D. Gates, Declan Ryan, Babak A. Parviz, and George M. Whitesides. “Water-Soluble Sacrificial Layers for Surface Micromachining”. *Small* 1 (7), **2005**, pp. 730–736.
- [190] Han-Jun Kim, Marcia Almanza-Workman, Bob Garcia, Ohseung Kwon, Frank Jeffrey, Steve Braymen, Jason Hauschildt, Kelly Junge, Don Larson, Dan Stieler, Alison Chaiken, Bob Cobene, Richard Elder, Warren Jackson, Mehrban Jam, Albert Jeans, Hao Luo, Ping Mei, Craig Perlov, and Carl Taussig. “Roll-to-roll manufacturing of electronics on flexible substrates using self-aligned imprint lithography (SAIL)”. *Journal of the Society for Information Display* 17 (11), **2009**, p. 963.
- [191] C. A. Volkert and A. M. Minor. “Focused Ion Beam Microscopy and Micromachining”. *MRS Bulletin* 32 (05), **2007**, pp. 389–399.
- [192] C. P. O Treutler. “Magnetic sensors for automotive applications”. *Sensors and Actuators A: Physical*. Third European Conference on Magnetic Sensors & Actuators. 91 (1), **2001**, pp. 2–6.
- [193] Jun-Yang Chen, Yong-Chang Lau, J. M. D. Coey, Mo Li, and Jian-Ping Wang. “High Performance MgO-barrier Magnetic Tunnel Junctions for Flexible and Wearable Spintronic Applications”. *Scientific Reports* 7, **2017**, p. 42001.
- [194] C. Barraud, C. Deranlot, P. Seneor, R. Mattana, B. Dlubak, S. Fusil, K. Bouzheouane, D. Deneuve, F. Petroff, and A. Fert. “Magnetoresistance in magnetic tunnel junctions grown on flexible organic substrates”. *Applied Physics Letters* 96 (7), **2010**, p. 072502.
- [195] Amilcar Bedoya-Pinto, Marco Donolato, Marco Gobbi, Luis E. Hueso, and Paolo Vavassori. “Flexible spintronic devices on Kapton”. *Applied Physics Letters* 104 (6), **2014**, p. 062412.

- [196] Olaf Ueberschar, Maria J. Almeida, Patrick Matthes, Mathias Muller, Ramona Ecke, Robert Ruckriem, Jorg Schuster, Horst Exner, and Stefan E. Schulz. “Optimized Monolithic 2-D Spin-Valve Sensor for High-Sensitivity Compass Applications”. *IEEE Transactions on Magnetics* 51 (1), **2015**, pp. 1–4.
- [197] J Nogués and Ivan K Schuller. “Exchange bias”. *Journal of Magnetism and Magnetic Materials* 192 (2), **1999**, pp. 203–232.
- [198] Daniil Karnaushenko, Niko Münzenrieder, Dmitriy D. Karnaushenko, Britta Koch, Anne K. Meyer, Stefan Baunack, Luisa Petti, Gerhard Tröster, Denys Makarov, and Oliver G. Schmidt. “Biomimetic Microelectronics for Regenerative Neuronal Cuff Implants”. *Advanced Materials* 27 (43), **2015**, pp. 6797–6805.
- [199] Dmitriy D Karnaushenko, Daniil Karnaushenko, Denys Makarov, and Oliver G Schmidt. “Compact helical antenna for smart implant applications”. *NPG Asia Materials* 7 (6), **2015**, e188–e188.
- [200] Chang Kyu Jeong, Kwi-Il Park, Jung Hwan Son, Geon-Tae Hwang, Seung Hyun Lee, Dae Yong Park, Han Eol Lee, Hwan Keon Lee, Myunghwan Byun, and Keon Jae Lee. “Self-powered fully-flexible light-emitting system enabled by flexible energy harvester”. *Energy Environ. Sci.* 7 (12), **2014**, pp. 4035–4043.
- [201] Ingolf Mönch, Denys Makarov, Radinka Koseva, Larysa Baraban, Daniil Karnaushenko, Claudia Kaiser, Karl-Friedrich Arndt, and Oliver G. Schmidt. “Rolled-Up Magnetic Sensor: Nanomembrane Architecture for In-Flow Detection of Magnetic Objects”. *ACS Nano* 5 (9), **2011**, pp. 7436–7442.
- [202] Xing Zhang, Huaqing Xie, Motoo Fujii, Hiroki Ago, Koji Takahashi, Tatsuya Ikuta, Hidekazu Abe, and Tetsuo Shimizu. “Thermal and electrical conductivity of a suspended platinum nanofilm”. *Applied Physics Letters* 86 (17), **2005**, p. 171912.
- [203] Peggy Cebe, Shirley Y. Chung, and Su-Don Hong. “Effect of thermal history on mechanical properties of polyetheretherketone below the glass transition temperature”. *Journal of Applied Polymer Science* 33 (2), **1987**, pp. 487–503.
- [204] E. Dallago, M. Ferri, P. Malcovati, A. Rossini, G. Venchi, and A. Baschirotto. “A CMOS 2D Micro-Fluxgate Earth Magnetic Field Detecting System with RS232 Digital Output”. *2007 IEEE Sensors*. Atlanta, GA, USA: IEEE, **2007**, pp. 240–243.
- [205] T.J. Peters. “Automobile navigation using a magnetic flux-gate compass”. *IEEE Transactions on Vehicular Technology* 35 (2), **1986**, pp. 41–47.
- [206] R. Racz, C. Schott, and S. Huber. “Electronic compass sensor”. *Proceedings of IEEE Sensors, 2004*. Vienna, Austria: IEEE, **2004**, pp. 1446–1449.
- [207] J.C. van der Meer, F.R. Riedijk, E. van Kampen, K.A.A. Makinwa, and J.H. Huijsing. “A fully integrated CMOS hall sensor with a $3.65\mu\text{T}$ 3σ offset for compass applications”. *ISSCC. 2005 IEEE International Digest of Technical Papers. Solid-State Circuits Conference, 2005*. San Francisco, CA, USA: IEEE, **2005**, pp. 246–247.

- [208] J. Lenz and S. Edelstein. “Magnetic sensors and their applications”. *IEEE Sensors Journal* 6 (3), **2006**, pp. 631–649.
- [209] B. Dufay, S. Saez, C. Dolabdjian, A. Yelon, and D. Menard. “Development of a High Sensitivity Giant Magneto-Impedance Magnetometer: Comparison With a Commercial Flux-Gate”. *IEEE Transactions on Magnetics* 49 (1), **2013**, pp. 85–88.
- [210] Bodong Li, Mincho N. Kavaldzhiev, and Jürgen Kosel. “Flexible magnetoimpedance sensor”. *Journal of Magnetism and Magnetic Materials* 378, **2015**, pp. 499–505.
- [211] M. Pannetier-Lecoeur, C. Fermon, A. de Vismes, E. Kerr, and L. Vieux-Rochaz. “Low noise magnetoresistive sensors for current measurement and compasses”. *Journal of Magnetism and Magnetic Materials* 316 (2), **2007**, e246–e248.
- [212] Chia-Yi Chiang, Jen-Tzong Jeng, Bor-Lin Lai, Van Su Luong, and Chih-Cheng Lu. “Tri-axis magnetometer with in-plane giant magnetoresistance sensors for compass application”. *Journal of Applied Physics* 117 (17), **2015**, 17A321.
- [213] J. Pelegri Sebastia, J. Alberola Lluch, J. R. Lajara Vizcaino, and J. Santiso Bellon. “Vibration Detector Based on GMR Sensors”. *IEEE Transactions on Instrumentation and Measurement* 58 (3), **2009**, pp. 707–712.
- [214] José Pelegrí Sebastiá, Jorge Alberola Lluch, and J. Rafael Lajara Vizcaíno. “Signal conditioning for GMR magnetic sensors: Applied to traffic speed monitoring GMR sensors”. *Sensors and Actuators A: Physical* 137 (2), **2007**, pp. 230–235.
- [215] F. Rottmann and F. Dettmann. “New magnetoresistive sensors: Engineering and applications”. *Sensors and Actuators A: Physical* 27 (1-3), **1991**, pp. 763–766.
- [216] Kaveh Mohamadabadi. “Anisotropic Magnetoresistance Magnetometer for inertial navigation systems”. PhD. France: Ecole Polytechnique X, 2013.
- [217] Honeywell International Inc. *1- and 2-Axis Magnetic Sensors HMC1021 Data-sheet*. **2008**. URL: https://aerocontent.honeywell.com/aero/common/documents/myaerospacecatalog-documents/Missiles-Munitions/HMC_1001-1002-1021-1022_Data_Sheet.pdf.
- [218] Tim Griesbach, Marc Christopher Wurz, and Lutz Rissing. “Design, Fabrication, and Testing of a Modular Magnetic Field Microsensor on a Flexible Polymer Foil”. *IEEE Transactions on Magnetics* 48 (11), **2012**, pp. 3843–3846.
- [219] Zhiguang Wang, Xinjun Wang, Menghui Li, Yuan Gao, Zhongqiang Hu, Tianxiang Nan, Xianfeng Liang, Huaihao Chen, Jia Yang, Syd Cash, and Nian-Xiang Sun. “Highly Sensitive Flexible Magnetic Sensor Based on Anisotropic Magnetoresistance Effect”. *Advanced Materials* 28 (42), **2016**, pp. 9370–9377.
- [220] Xueping Li, Guifu Ding, Taeko Ando, Mitsuhiro Shikida, and Kazuo Sato. “Micromechanical characterization of electroplated permalloy films for MEMS”. *Microsystem Technologies* 14 (1), **2007**, pp. 131–134.

- [221] Carnegie Mellon University. *Panda3D - Free 3D Game Engine*. **2010**. URL: <https://www.panda3d.org/>.
- [222] D. Cohen, Y. Palti, B. N. Cuffin, and S. J. Schmid. “Magnetic fields produced by steady currents in the body.” *Proceedings of the National Academy of Sciences* 77 (3), **1980**, pp. 1447–1451.
- [223] S. J. Williamson and L. Kaufman. “Biomagnetism”. *Journal of Magnetism and Magnetic Materials* 22 (2), **1981**, pp. 129–201.
- [224] Gerhard Baule and Richard McFee. “Detection of the magnetic field of the heart”. *American Heart Journal* 66 (1), **1963**, pp. 95–96.
- [225] Gerhard M. Baule and Richard McFee. “The magnetic heart vector”. *American Heart Journal* 79 (2), **1970**, pp. 223–236.
- [226] P. P. Freitas, F. A. Cardoso, V. C. Martins, S. A. M. Martins, J. Loureiro, J. Amaral, R. C. Chaves, S. Cardoso, L. P. Fonseca, A. M. Sebastião, M. Pannetier-Lecoeur, and C. Fermon. “Spintronic platforms for biomedical applications”. *Lab on a Chip* 12 (3), **2012**, pp. 546–557.
- [227] Daniil Karnaushenko, Dmitriy D. Karnaushenko, Denys Makarov, Stefan Baunack, Rudolf Schäfer, and Oliver G. Schmidt. “Self-Assembled On-Chip-Integrated Giant Magneto-Impedance Sensorics”. *Advanced Materials* 27 (42), **2015**, pp. 6582–6589.
- [228] M. Pannetier-Lecoeur, L. Parkkonen, N. Sergeeva-Chollet, H. Polovy, C. Fermon, and C. Fowley. “Magnetocardiography with sensors based on giant magnetoresistance”. *Applied Physics Letters* 98 (15), **2011**, p. 153705.
- [229] A. Schuhl, F. Nguyen Van Dau, and J. R. Childress. “Low-field magnetic sensors based on the planar Hall effect”. *Applied Physics Letters* 66 (20), **1995**, pp. 2751–2753.
- [230] Yevgeniy Telepinsky, Vladislav Mor, Moty Schultz, Yu-Ming Hung, Andrew D. Kent, and Lior Klein. “Towards a six-state magnetic memory element”. *Applied Physics Letters* 108 (18), **2016**, p. 182401.
- [231] V. Mor, M. Schultz, O. Sinwani, A. Grosz, E. Paperno, and L. Klein. “Planar Hall effect sensors with shape-induced effective single domain behavior”. *Journal of Applied Physics* 111 (7), **2012**, 07E519.
- [232] Robert Streubel, Jehyun Lee, Denys Makarov, Mi-Young Im, Daniil Karnaushenko, Luyang Han, Rudolf Schäfer, Peter Fischer, Sang-Koog Kim, and Oliver G. Schmidt. “Magnetic Microstructure of Rolled-Up Single-Layer Ferromagnetic Nanomembranes”. *Advanced Materials* 26 (2), **2014**, pp. 316–323.
- [233] Robert Streubel, Dominic J. Thurmer, Denys Makarov, Florian Kronast, Tobias Kosub, Volodymyr Kravchuk, Denis D. Sheka, Yuri Gaididei, Rudolf Schäfer, and Oliver G. Schmidt. “Magnetically Capped Rolled-up Nanomembranes”. *Nano Letters* 12 (8), **2012**, pp. 3961–3966.
- [234] A. Grosz, V. Mor, E. Paperno, S. Amrusi, I. Faivinov, M. Schultz, and L. Klein. “Planar Hall Effect Sensors With Subnanotesla Resolution”. *IEEE Magnetics Letters* 4, **2013**, pp. 6500104–6500104.

- [235] Gungun Lin, Dmitriy D. Karnaushenko, Gilbert Santiago Cañón Bermúdez, Oliver G. Schmidt, and Denys Makarov. “Magnetic Suspension Array Technology: Controlled Synthesis and Screening in Microfluidic Networks”. *Small* 12 (33), **2016**, pp. 4553–4562.
- [236] Fluke Corporation. *Clamp Multimeters / Fluke 325 True-RMS Clamp Meter*. **2019**. URL: <https://www.fluke.com/en-us/product/electrical-testing/clamp-meters/fluke-325>.
- [237] Takao Someya. “Continuous Health-Monitoring With Ultraflexible On-Skin Sensors”. *AAAS - 2018 AAAS Annual Meeting*. **2018**.
- [238] Youngsik Lee, Jaemin Kim, Hyunwoo Joo, Milan S. Raj, Roozbeh Ghaffari, and Dae-Hyeong Kim. “Wearable Sensing Systems with Mechanically Soft Assemblies of Nanoscale Materials”. *Advanced Materials Technologies* 2 (9), **2017**, p. 1700053.
- [239] Ivan R. Minev, Pavel Musienko, Arthur Hirsch, Quentin Barraud, Nikolaus Wenger, Eduardo Martin Moraud, Jérôme Gandar, Marco Capogrosso, Tomislav Milekovic, Léonie Asboth, Rafael Fajardo Torres, Nicolas Vachicouras, Qihan Liu, Natalia Pavlova, Simone Duis, Alexandre Larmagnac, Janos Vörös, Silvestro Micera, Zhigang Suo, Grégoire Courtine, and Stéphanie P. Lacour. “Electronic dura mater for long-term multimodal neural interfaces”. *Science* 347 (6218), **2015**, pp. 159–163.
- [240] Baoxing Xu, Aadeel Akhtar, Yuhao Liu, Hang Chen, Woon-Hong Yeo, Sung II Park, Brandon Boyce, Hyunjin Kim, Jiwoo Yu, Hsin-Yen Lai, Sungyoung Jung, Yuhao Zhou, Jeonghyun Kim, Seongkyu Cho, Yonggang Huang, Timothy Bretl, and John A. Rogers. “An Epidermal Stimulation and Sensing Platform for Sensorimotor Prosthetic Control, Management of Lower Back Exertion, and Electrical Muscle Activation”. *Advanced Materials* 28 (22), **2016**, pp. 4462–4471.
- [241] Seungyong Han, Jeonghyun Kim, Sang Min Won, Yinji Ma, Daeshik Kang, Zhaoqian Xie, Kyu-Tae Lee, Ha Uk Chung, Anthony Banks, Seunghwan Min, Seung Yun Heo, Charles R. Davies, Jung Woo Lee, Chi-Hwan Lee, Bong Hoon Kim, Kan Li, Yadong Zhou, Chen Wei, Xue Feng, Yonggang Huang, and John A. Rogers. “Battery-free, wireless sensors for full-body pressure and temperature mapping”. *Science Translational Medicine* 10 (435), **2018**, eaan4950.
- [242] Gunchul Shin, Adrian M. Gomez, Ream Al-Hasani, Yu Ra Jeong, Jeonghyun Kim, Zhaoqian Xie, Anthony Banks, Seung Min Lee, Sang Youn Han, Chul Jong Yoo, Jong-Lam Lee, Seung Hee Lee, Jonas Kurniawan, Jacob Tureb, Zhongzhu Guo, Jangyeol Yoon, Sung-Il Park, Sang Yun Bang, Yoonho Nam, Marie C. Walicki, Vijay K. Samineni, Aaron D. Mickle, Kunhyuk Lee, Seung Yun Heo, Jordan G. McCall, Taisong Pan, Liang Wang, Xue Feng, Tae-il Kim, Jong Kyu Kim, Yuhang Li, Yonggang Huang, Robert W. Gereau, Jeong Sook Ha, Michael R. Bruchas, and John A. Rogers. “Flexible Near-Field Wireless Optoelectronics as Subdermal Implants for Broad Applications in Optogenetics”. *Neuron* 93 (3), **2017**, 509–521.e3.

- [243] Aaron D. Mickle, Sang Min Won, Kyung Nim Noh, Jangyeol Yoon, Kathleen W. Meacham, Yeguang Xue, Lisa A. McIlvried, Bryan A. Copits, Vijay K. Samineni, Kaitlyn E. Crawford, Do Hoon Kim, Paulome Srivastava, Bong Hoon Kim, Seunghwan Min, Young Shiuan, Yeojeong Yun, Maria A. Payne, Jianpeng Zhang, Hokyung Jang, Yuhang Li, H. Henry Lai, Yonggang Huang, Sung-Il Park, Robert W. Gereau, and John A. Rogers. “A wireless closed-loop system for optogenetic peripheral neuromodulation”. *Nature* 565 (7739), **2019**, p. 361.
- [244] Niko Münzenrieder, Christoph Zysset, Luisa Petti, Thomas Kinkeldei, Giovanni A. Salvatore, and Gerhard Tröster. “Room temperature fabricated flexible NiO/IGZO pn diode under mechanical strain”. *Solid-State Electronics* 87, **2013**, pp. 17–20.
- [245] Niko Münzenrieder, Giuseppe Cantarella, Christian Vogt, Luisa Petti, Lars Bütthe, Giovanni A. Salvatore, Yang Fang, Renzo Andri, Yawhuei Lam, Rafael Libanori, Daniel Widner, André R. Studart, and Gerhard Tröster. “Stretchable and Conformable Oxide Thin-Film Electronics”. *Advanced Electronic Materials* 1 (3), **2015**.
- [246] N. Munzenrieder, C. Zysset, T. Kinkeldei, and G. Troster. “Design Rules for IGZO Logic Gates on Plastic Foil Enabling Operation at Bending Radii of 3.5 mm”. *IEEE Transactions on Electron Devices* 59 (8), **2012**, pp. 2153–2159.
- [247] Zhenxing Wang, Mehrdad Shaygan, Martin Otto, Daniel Schall, and Daniel Neumaier. “Flexible Hall sensors based on graphene”. *Nanoscale* 8 (14), **2016**, pp. 7683–7687.
- [248] Hui Fang, Jianing Zhao, Ki Jun Yu, Enming Song, Amir Barati Farimani, Chia-Han Chiang, Xin Jin, Yeguang Xue, Dong Xu, Wenbo Du, Kyung Jin Seo, Yiding Zhong, Zijian Yang, Sang Min Won, Guanhua Fang, Seo Woo Choi, Santanu Chaudhuri, Yonggang Huang, Muhammad Ashrafal Alam, Jonathan Viventi, N. R. Aluru, and John A. Rogers. “Ultrathin, transferred layers of thermally grown silicon dioxide as biofluid barriers for biointegrated flexible electronic systems”. *Proceedings of the National Academy of Sciences* 113 (42), **2016**, pp. 11682–11687.

List of publications

- [1] Pablo Nicolás Granell, Guoliang Wang, Gilbert Santiago Cañón Bermúdez, Tobias Kosub, Federico Golmar, Laura Steren, Jürgen Fassbender, and Denys Makarov. “Highly compliant planar Hall effect sensor with sub 200 nT sensitivity”. *npj Flexible Electronics* 3 (1), **2019**, p. 3.
- [2] Gilbert Santiago Cañón Bermúdez, Hagen Fuchs, Lothar Bischoff, Jürgen Fassbender, and Denys Makarov. “Electronic-skin compasses for geomagnetic field-driven artificial magnetoreception and interactive electronics”. *Nature Electronics* 1 (11), **2018**, p. 589.
- [3] Gilbert Santiago Cañón Bermúdez, Dmitriy D. Karnaushenko, Daniil Karnaushenko, Ana Lebanov, Lothar Bischoff, Martin Kaltenbrunner, Jürgen Fassbender, Oliver G. Schmidt, and Denys Makarov. “Magnetosensitive e-skins with directional perception for augmented reality”. *Science Advances* 4 (1), **2018**, eaao2623.
- [4] Gungun Lin, Dmitriy D. Karnaushenko, Gilbert Santiago Cañón Bermúdez, Oliver G. Schmidt, and Denys Makarov. “Magnetic Suspension Array Technology: Controlled Synthesis and Screening in Microfluidic Networks”. *Small* 12 (33), **2016**, pp. 4553–4562.
- [5] Michael Melzer, Jens Ingolf Mönch, Denys Makarov, Yevhen Zabala, Gilbert Santiago Cañón Bermúdez, Daniil Karnaushenko, Stefan Baunack, Falk Bahr, Chenglin Yan, Martin Kaltenbrunner, and Oliver G. Schmidt. “Wearable Magnetic Field Sensors for Flexible Electronics”. *Advanced Materials* 27 (7), **2015**, pp. 1274–1280.

Contributed talks

- [1] Gilbert Santiago Cañón Bermúdez. *Compliant on-skin compass for artificial magnetoception*. NanoBioSensors Conference. Dresden, Germany, **2017**.
- [2] Gilbert Santiago Cañón Bermúdez. *Compliant on-skin compass for artificial magnetoception*. MRS (Materials Research Society) Spring Meeting and Exhibit. Phoenix, USA, **2017**.
- [3] Gilbert Santiago Cañón Bermúdez. *Compliant on-skin compass for artificial magnetoception*. DPG (German Physical Society) Spring Meeting. Dresden, Germany, **2017**.
- [4] Gilbert Santiago Cañón Bermúdez. *Touchless omnidirectional magnetosensitive skins for interactive electronics*. MRS (Materials Research Society) Fall Meeting and Exhibit. Boston, USA, **2017**.
- [5] Gilbert Santiago Cañón Bermúdez. *Magnetic functionalities for flexible interactive electronics*. (Materials Research Society) Spring Meeting and Exhibit. Phoenix, USA, **2016**.
- [6] Gilbert Santiago Cañón Bermúdez. *Ultrathin magnetic angle sensor for on-skin interactive electronics*. (Materials Research Society) Spring Meeting and Exhibit. Phoenix, USA, **2016**.
- [7] Gilbert Santiago Cañón Bermúdez. *Ultra-thin magnetic angle sensor for on-skin interactive electronics*. DPG (German Physical Society) Spring Meeting. Regensburg, Germany, **2016**.
- [8] Gilbert Santiago Cañón Bermúdez. *Wearable magnetic field sensors for flexible electronics*. (Materials Research Society) Spring Meeting and Exhibit. Phoenix, USA, **2016**.
- [9] Gilbert Santiago Cañón Bermúdez. *Flexible large area sensors for magnetic field mapping*. WE_Heraeus-Seminar on Flexible, Stretchable and Printable High Performance Electronics. Bad Honnef, Germany, **2015**.
- [10] Gilbert Santiago Cañón Bermúdez. *Wearable magnetic field sensors for flexible electronics*. DPG (German Physical Society) Spring Meeting. Berlin, Germany, **2015**.